Università
Ca'Foscari
Venezia

Master's Degree Programme

in Sustainable Chemistry and Technologies

Final Thesis

Strategies for improving CO_2 photoreduction under solar light.

Supervisor

Ch. Prof. Michela Signoretto

Assistant Supervisor

Ch. Dott. Giulia Forghieri

Graduand

Giorgia Ferraro 875598

Academic Year

2022/2023

INDEX

1. INTRODUCTION

1.1 PREFACTION

In the last few decades, global warming has gained increasing attention all over the world. This phenomenon refers to the increase of the average temperature of the earth, that is due to the further emissions of greenhouse gases (GHG) such as carbon dioxide, methane, nitrous oxides, chlorofluorocarbons, water vapor and ozone[1]. The continuous increase of these gases in the atmosphere has led to various effects such as: sea-level rise (about 3,2 mm per year), melting of glaciers, temperature increase, and drought, resulting in several political, economic and social issues[2].

National Centers for Environmental Information (NOAA) has estimated that the year 2022 was the sixth warmest year since 1880-1900, namely the pre-industrial period. Since that time, the average temperature on earth has risen at a rate of 0,08°C every 10 years and 0,18°C since 1981.

Figure 1 reports the trend of the global average temperature from 1880 to 2022[3].

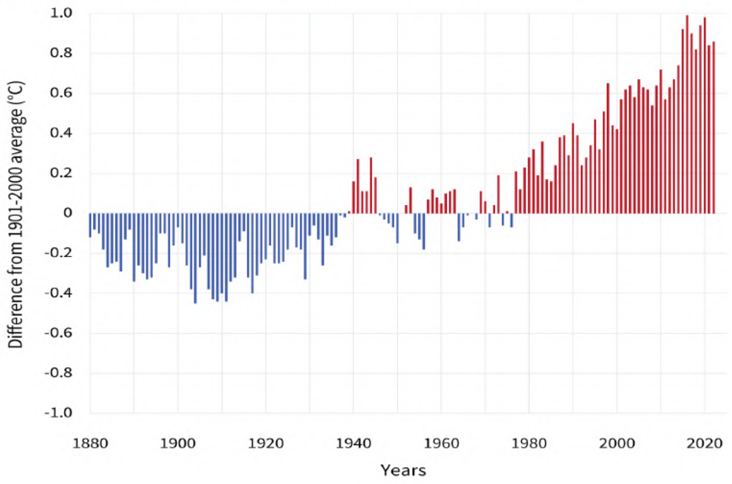

Figure 1: *Yearly surface temperature compared to the 20th-century average from 1880–2022*[3].

Human activities such as combustion of fossil resources (oil, natural gas, carbon) for transportation and energy production, deforestation, agriculture and industrial processes, are leading to the increase of greenhouse gases concentration in the atmosphere[4]. Carbon dioxide (CO_2) is the most abundant greenhouse gas, followed by methane (CH_4) that is released in the atmosphere during natural gas extraction, production, transport, and distribution[1].

Nitrous oxide (N_2O) mainly derives from wastewater and has a global warming potential being about 310 times higher than that of CO_2, but its concentration is lower, even if it is estimated that could increase by 0,2% per year[5]. Water vapor (H_2O) is a condensable gas, whose concentration depends on the temperature of the atmosphere, because it absorbs heat from earth and prevents it from escaping out to space. The increment of water vapor in the atmosphere is called "positive feedback" because it is the only gas whose concentration increases with increasing of temperature[6].

Compared to CO_2 and N_2O, whose emissions derive from human activities and nature, fluorinated gases derive exclusively from anthropogenic activities and industrial processes[7]. In 2018, F-gases emissions accounted for 3% of greenhouse gas emissions in Europe also contributing to climate change[8]. The contribution of the main greenhouse gases is shown in Figure 2.

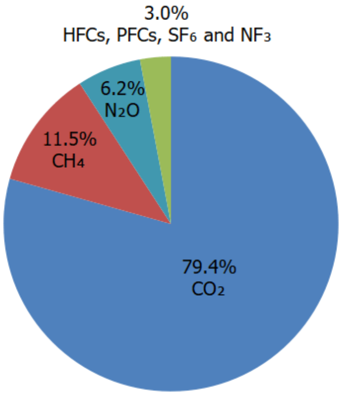

Figure 2: *Emissions of the main greenhouse gases in 2021*[9].

In 2005, the Kyoto's protocol came into effect to reduce the environmental impact due to greenhouse gas emissions. It was about limiting GHG emissions by 5% below pre-industrial level, using targeted strategies to contain climate changes[10]. Then in 2015 the Paris Agreement, an international treaty, was stipulated in order to limit global warming to 1,5°C by adopting various action plans.

Through the stipulation of the Green Deal, Europe states are committed in achieving climate neutrality by 2050, which means bringing emission down to zero, by applying circular economy policies based on waste valorization and recycle, replacement of fossil resources with renewable ones, and on the use of low or zero emission vehicles.

Eventually, COP 27 held in Sharm El-Sheikh in November 2022, reiterated the need to achieve climate neutrality by 2050[11]. Therefore, considered the urgency to reduce GHG emissions, different strategies are being implemented, including replacing fossil fuels with renewable energy resources, electrifying transports[1], renovating and constructing buildings using less carbon-intensive materials, enhancing waste and using it as resources for new applications, in accordance with the principles of the circular economy[12]. The strategies to reduce carbon dioxide emissions - one of the most concerning among greenhouse gases - include carbon capture and sequestration and carbon capture and utilization technologies.

1.2 CARBON DIOXIDE

Carbon dioxide is the most abundant greenhouse gas emitted by human activities, accounting for 79% of global warming, that is significantly higher than the pre-industrial period[9]. It is considered that in 1950, 6 billion tons of carbon dioxide were emitted. Since now, emissions are rapidly increasing so that, every year, more than 34 billion tons are emitted[13]. In the last decades, CO_2 concentration in the atmosphere has grown up to 410 ppm (Figure 3)[14].

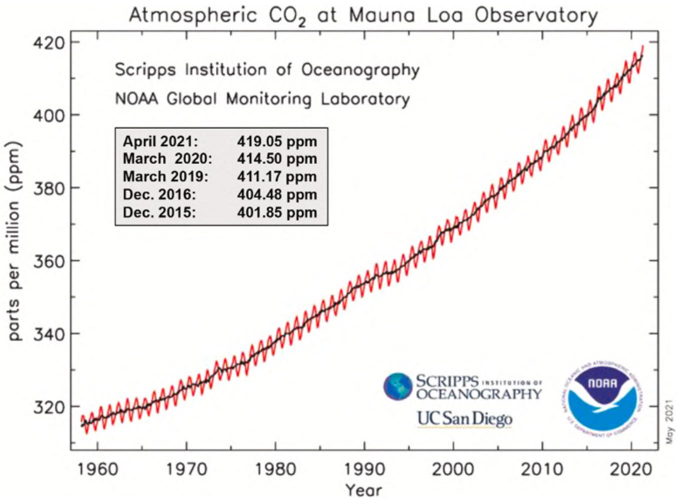

Figure 3: *Concentration of CO_2 in the last decades*[15].

Carbon dioxide is naturally present in the atmosphere due to the natural carbon cycle among oceans, plants, air, animals, and soil. CO_2 remains in the atmosphere for a long time, and it is the cause of global warming as it absorbs outgoing infra-red radiation from the earth's surface and releases part of it back to Earth[15].

The carbon cycle is altered by human activities such as combustion of fossil fuels for transports and energy in major measure, industrial processes like cement production, land-use and forestry, because trees fix carbon through photosynthesis, but subsequent abatement results in the release of high amounts of carbon dioxide[16].

To reduce the concentration of CO_2, it is important to implement strategies such as developing carbon-neutral fuels and energy sources, using technologies like carbon capture and storage (CCS) and carbon capture and utilization (CCU), and converting it into high value-added products. CCS technologies consist in the capture of CO_2 directly from the air; near industrial sites involved in the production of cement and/or petrochemical plants; from the combustion of oxyfuels whose products are concentrated in CO_2; from pre-combustion which consists in the gasification of fossil fuels to give syngas, from which CO_2 is separated before hydrogen being burned; and from post-combustion, which refers to the removal of gas following the combustion process[15]. While the first method of removing carbon dioxide directly from the air (DAC) is difficult to apply industrially, due to the low concentrations of CO_2, the post-combustion method owns the potential to become commercially available[17]. The latter consists in the removal of the gas by chemical adsorption on amine solvents, perfluorinated solvents, or ionic liquids; by physical absorption on solid supports such as activated carbon, graphene, zeolites, MOFs, in which the gas reacts with oxides or carbonates such as $CaCO_3$ or dolomite[15]. Once CO_2 is captured, it is stored in different ways, such as CO_2-enhanced oil recovery (EOR) and saline formations. Other methods consist of storing by enhanced gas recovery (EGR) in oil and gas fields (not yet applied on industrial scale), ocean and mineral storing, which are currently under development[18].

Moreover, once captured, CO_2 can be used directly (non-conversion) in different industries like food, agro-chemistry, and packaging, or further converted into high-value products, such as fuels and chemicals. In recent years, technologies such as electrocatalysis and photocatalysis are gaining increasing attention and could play an important role in achieving net zero CO_2 emissions[19].

For instance, some products of interest include carbon monoxide, formic acid and methane[20,21]. The latter can be exploited and used as an energy source in industrial plants, in residential heating, and as fuel in automotive. It is also a building block for the synthesis of various chemical compounds[22]. In addition, methanol and dimethyl ether are considered as appealing products for future development. The first can be used as an alternative fuel, as an energy-storage material and as a starting material for the synthesis of other chemical compounds, boasting a production of about 110 million metric tons per year[23],[24]. The latter is an environmentally friendly compound whose production is about 6 million tons per year, and it is used as an intermediate to fuels and oxygenated products[17].

Therefore, achieving the scalable conversion of carbon dioxide as a carbon source for obtaining high-value products could be of high interest, beside falling within the principles of the circular economy. Carbon dioxide is an apolar, abundant, cheap, non-toxic, thermodynamically stable molecule, with high binding energies mainly relative to the C=O bond, owning a standard Gibbs free energy equal to $\Delta G° = -394{,}4\ kJ/mol$. For this reason, additional energy is required to make the reduction happen, by means of the addition of a single electron with the consequent formation of a radical and by the variation of the molecular structure. This is due to the loss of symmetry and to the repulsion between the free electron pairs on the oxygen atoms and the radical electron[25,26]. Table 1 shows the electrochemical CO_2 reduction potentials versus the NHE (Normal Hydrogen Electrode) at pH=7.

Table 1: *Electrochemical reduction potentials of CO_2.*

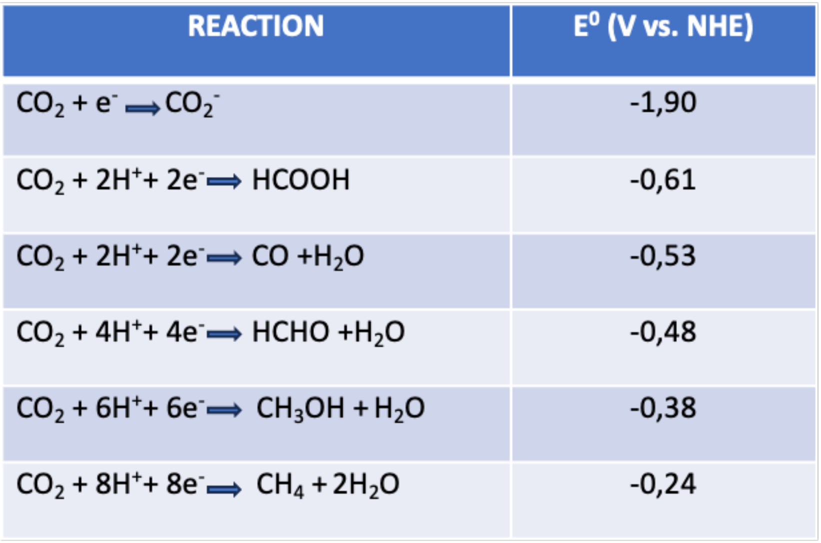

REACTION	E^0 (V vs. NHE)
$CO_2 + e^- \Longrightarrow CO_2^-$	-1,90
$CO_2 + 2H^+ + 2e^- \Longrightarrow HCOOH$	-0,61
$CO_2 + 2H^+ + 2e^- \Longrightarrow CO + H_2O$	-0,53
$CO_2 + 4H^+ + 4e^- \Longrightarrow HCHO + H_2O$	-0,48
$CO_2 + 6H^+ + 6e^- \Longrightarrow CH_3OH + H_2O$	-0,38
$CO_2 + 8H^+ + 8e^- \Longrightarrow CH_4 + 2H_2O$	-0,24

To overcome the energy request for CO_2 activation, catalysis is widely used. This allows to lower the activation energy of the reaction, to improve the selectivity towards the desired product and to limit the formation of by-products[26]. It has been seen that many semiconductors are able to convert CO_2 into fuels by involving a multi-electronic transfer assisted by the presence of protons[27].

New catalytic approaches for carbon dioxide reduction such as electroreduction and photocatalysis have been currently studied. While the former applies electricity to perform CO_2 reduction, which could however derive from non-renewable energy sources, photocatalysis exploits solar energy as a renewable energy source, thus resulting in a promising method to enable the conversion of carbon dioxide. Therefore, the use of photocatalysis could be a more sustainable way to upcycle carbon dioxide.

1.3 PHOTOCATALYSIS

Photocatalysis is a catalytic approach used in the treatment of air pollutants, wastewater, and other redox reactions such as water splitting, CO_2 reduction and sterilization[28]. The photocatalytic process involves the use of solar radiation, as abundant, available, free, and unlimited energy source, although being intermittent, and of a semiconductor material.

A semiconductor is a material in which the structure of orbitals defines a band structure, composed by a valence band and a conduction band, separated by an energy gap, usually between 0.3-5 eV. If the semiconductor is irradiated by a radiation of energy equal to or greater than the band gap, there is the formation of an exciton that is composed of an electron excited from the valence band to the conduction band, and an empty state called hole on the valence band. The formed electrons may move from the bulk to the surface where they are available to react with an accepting molecule - such as carbon dioxide , and performing a reducing reaction, while the hole can catalyze an oxidizing reaction, such as water into oxygen and hydrogen[25,26].

To enable the reaction, the potential of conduction band of the semiconductor must be more negative than the reduction potential of CO_2, and the potential of valence band must be more positive than the oxidative potential of the reducing agent, being water in this case[29].

However, electron-hole recombination processes may occur, which consist in the tendency of electrons to return to the valence band and interact with the holes, releasing energy in the form of heat or photons; in this way, electrons are no longer available to react and photoactivity is reduced[30]. The mechanism of the photocatalytic process is reported in Figure 4.

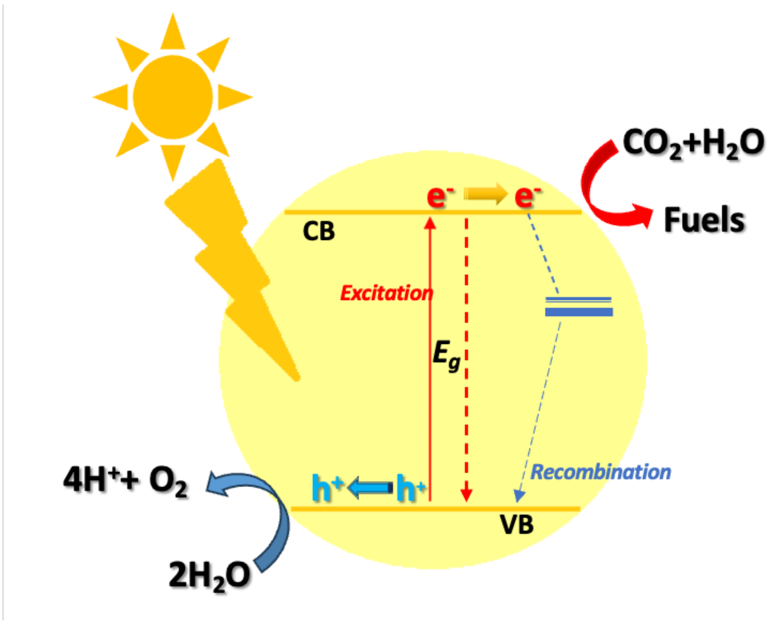

Figure 4: *Photocatalytic process*

An ideal photocatalyst has the smallest band gap to ensure the better energy efficiency and greater exploitation of the solar spectrum; good photon absorption capacity, good charge mobility and slow recombination rate, to enable a more efficient charge transfer on the surface. The material should be photochemically stable to photo corrosion, which is generally proportional to the intensity of the redox process. This phenomenon consists of photogenerated electrons and holes which can participate in decomposing the semiconductor. In particular, photogenerated holes, before being consumed, could be present on the outer surface. If the semiconductor is a metal sulfide such as CdS, sulfide ions are oxidated by holes, thereby resulting in low photostability[31].

Amongst the materials investigated for the photocatalytic process, titanium dioxide (titania) is the most widely studied as it is non-toxic, available, economic, and stable. TiO_2 is a polymorph semiconductor presents in three different crystalline structures: rutile, anatase and brookite, with anatase being the most photo-active phase due to its higher charge mobility and then rutile owns a higher recombination rate instead[32]. The most employed commercial titania is Degussa P25, in which both allotropic phases are present, in the proportion of 75% anatase and about 25% rutile.

The use of titania is limited because of its high bandgap of about 3,2 eV, that allows the absorption of radiation only in the ultraviolet region (UV), which makes up only 10% of the solar spectrum. It is also sensitive to surface's degradation and has high recombination rate[30]. Another common semiconductor is zinc oxide (ZnO) that has excellent optical properties. However, it suffers from photo corrosion, it has high recombination rate, and due to the conduction band position it is less likely to directly reduce CO_2[33].

For the application of photocatalysis in the reduction of carbon dioxide, its reduction mechanism must first be considered. In the literature, three different pathways have been proposed: formaldehyde, carbene and glyoxal pathways, of which the first two are the most widespread. The initial step is common to both pathways and consists in the activation of CO_2 through the transfer of an electron, leading to the formation of the $CO_2^{-\cdot}$ radical. After that, the main differences consist in the adsorption mode of $CO_2^{\cdot}$ on the surface of the photocatalyst, such as TiO_2. The formaldehyde pathway is a fast hydrogenation where $CO_2^{-\cdot}$ oxygen coordinates the titanium atom and reacts with a proton leading to the subsequent formation of the $COOH^{\cdot}$ radical, which recombines with the $H^{\cdot}$ radical to form formic acid. The latter accepts an additional $H^{\cdot}$ forming formaldehyde, then methanol and finally methane. In the carbene pathway, $CO_2^{-\cdot}$ carbon coordinates the semiconductor and reacts with a proton that breaks the C-O bond forming CO; then through reduction steps, CH_4 and CH_3OH are formed[27],[34]. In Figure 5*,* the carbon dioxide reduction pathways are reported.

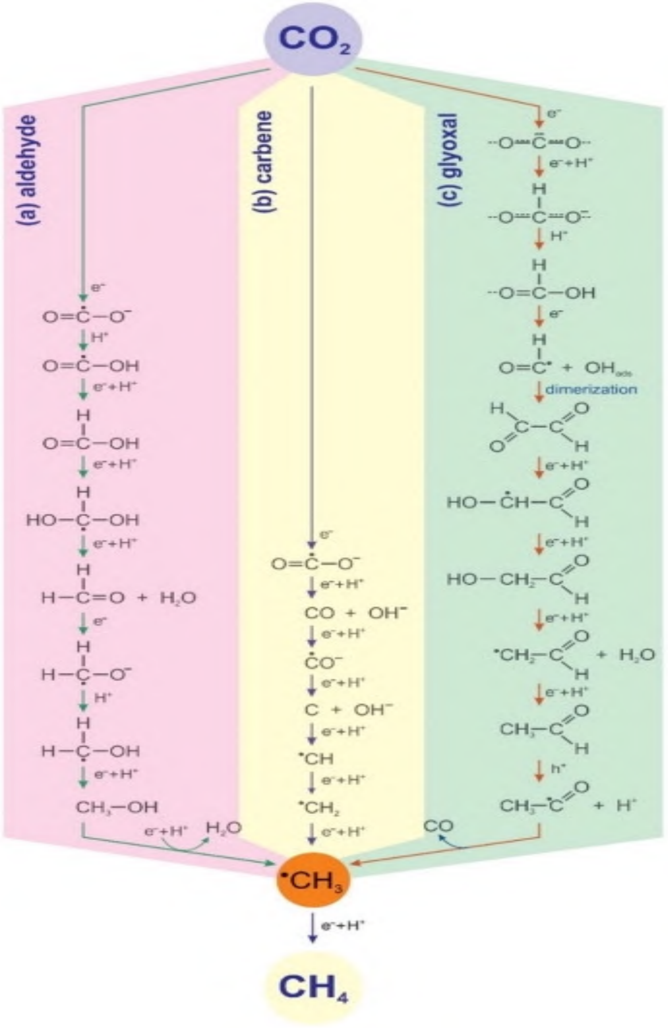

Figure 5*: Carbon dioxide pathways*[35].

The operating parameters used in the photocatalytic reaction are also fundamental for obtaining an efficient and selective catalytic system.

Some works have reported that higher temperature generate higher products yields, because of the rapid adsorption and desorption of the reactants and products from the photocatalyst. Also, an increase of the pressure, both in gas and liquid phases, involves an increase in the adsorption of carbon dioxide on the surface of the catalyst and therefore higher hydrocarbon generation. Moreover, it is reported that basic conditions in liquid phase lead to the increasing solubility of carbon dioxide and higher methanol yield; on the other side, in gas phase, basic sites on photocatalyst allow better interaction with carbon dioxide, that is slightly acidic[36]. The photocatalytic activity is influenced by the reaction time. *Sasirekha et al.* have reported that when irradiation time increase beyond six hours, the photocatalyst tends to deteriorate and be deactivated[37]; and by the wavelength of light used to irradiate the catalyst, in fact with lower wavelength the generation rate of the exciton is higher and thus the photocatalytic activity is enhanced[32]. Irradiance, as the number of photons per unit of time and area, also affects the photocatalyst and the selectivity of the reaction because it accelerates the process by lowering the activation energy. In addition, the photoreactor influences the photoactivity by enhancing light-harvesting process and the separation of products; reducing the recombination and photon loss and by increasing the photocatalyst surface area[36]. Typically, due to its geometry, a fixed bed reactor favors a homogeneous irradiation, limits pressure drops, and doesn't require the separation of the catalyst, whereas in slurry reactors, the irradiation is not homogeneous. In this study, a thin film fixed bed reactor is applied for the gas phase reaction. Despite in the liquid-phase methanol, methane and formic acid are generated, in the gas-phase reaction, methane and carbon monoxide are the only products that are generated. In addition, compared to liquid phase, the gas one promotes high penetrability of light radiation, high diffusivity, and high miscibility of gaseous reagents (carbon dioxide and water vapor).

1.4 PEROVSKITES

The selection and the study of the starting catalytic material plays an important role in the performance and selectivity of the reaction. Due to the limiting activity in the visible region and recombination problems of the common semiconductors, perovskites are gaining attention in photocatalysis. Perovskites is a family of materials, currently less studied, which have general formula ABO_3. Generally, A is the cation of an alkaline earth metal such as barium, calcium, strontium, that interacts weakly with oxygen, while B is a transition metal such as titanium cation that interacts strongly with oxygen or any other present anion. The materials exhibit ferroelectric, piezoelectric and photocatalytic properties.

Titanium is one of the most abundant elements in the earth's crust, that is very stable and environmentally friendly, for this reason titanium-based perovskites are currently being considered[38]. Titanate perovskites were studied in photocatalytic applications such as carbon dioxide photoreduction, photocatalytic water splitting, photooxidation of organic molecules and photocatalytic nitrogen fixation. Compared to titania, perovskites show good photostability, corrosion resistance in aqueous solutions and band gap necessary for obtaining all the products of carbon dioxide reduction. In particular, barium titanate ($BaTiO_3$) and calcium titanate ($CaTiO_3$) are characterized by an intrinsic basicity and hydrophobicity, which favors the interaction with carbon dioxide - which is slightly acidic - in the photoreduction reaction[39]. Despite $SrTiO_3$ is commonly used as a photocatalyst in water splitting due to the similar band gap to titania, its high recombination rate limits its application, so in this work, barium and calcium titanates will be considered[40]. Band positions are reported in Figure 6.

$BaTiO_3$ presents four different crystal structures, cubic, tetragonal, orthorhombic, and rhombohedral, among which the tetragonal and cubic ones are the most important ones (Figure 7). The tetragonal phase shows ferroelectric properties, that help the narrowing of the band gap. As the temperature decreases, three phase transitions occur, that involve a structural change in barium titanate, which is due to the variation of the band gap and of the ferroelectric properties[41]. *Kwak et al.* reported that $BaTiO_3$ shows the best photocatalytic activity in CO_2 photoreduction, compared to $SrTiO_3$ and $CaTiO_3$, because of the lower recombination rate, the higher surface area and the better interaction with carbon dioxide[40]. On the other side, calcium titanate presents the same crystalline structures of barium titanate, and the orthorhombic one is the most stable. In addition, calcium has a smaller ionic radius than the barium one, which could therefore affect the properties of perovskite. This perovskite possesses a more negative conduction band potential and a more positive valence band potential than that of titania and strontium titanate. For this reason, it is suitable to be applied in water splitting and wastewater treatment. However, it has large band gap value of about 3,5 eV and high recombination rate[42].

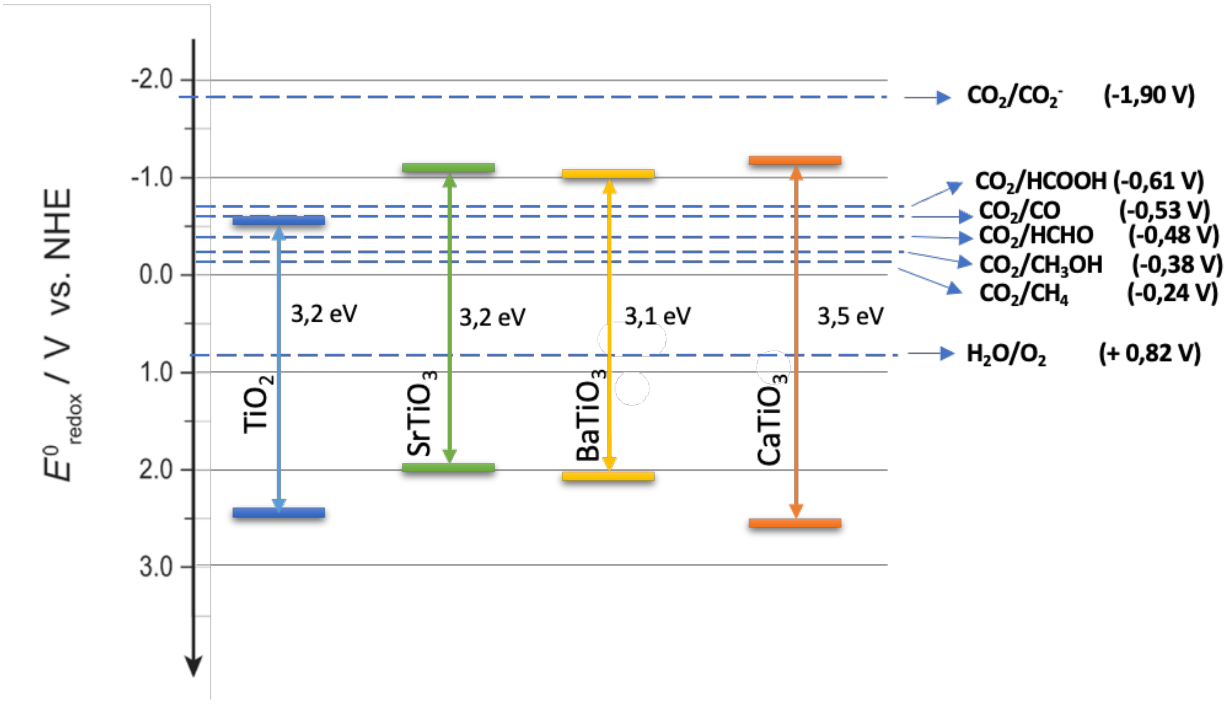

Figure 6: *Band positions of titanate-perovskites compared to titania*[40]

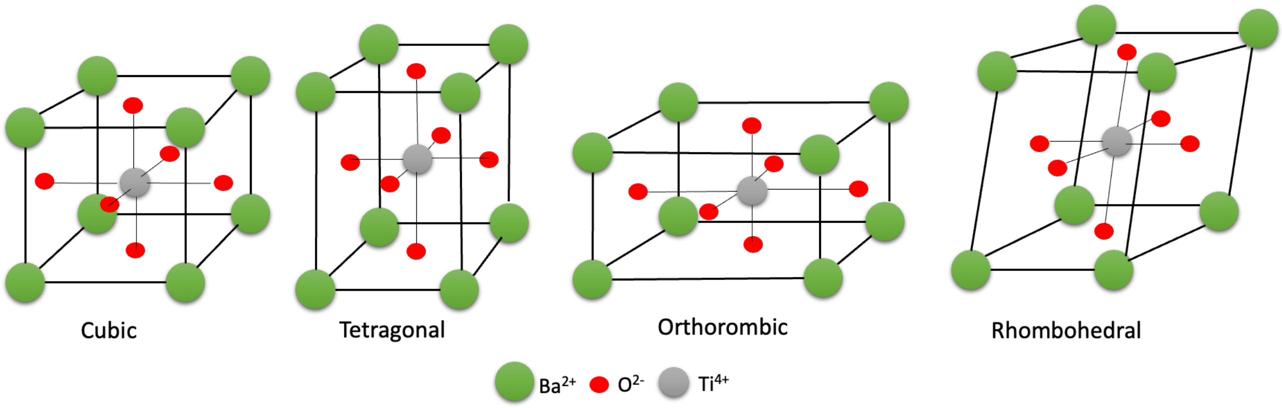

Figure 7: *Crystalline phases of* $BaTiO_3$

Barium titanate and calcium titanate can be synthetized by several methods such as hydrothermal, solvothermal, microwave, co-precipitation, sol-gel, combustion, and others. Among them, hydrothermal treatment, a bottom-up approach, is the most popular one. The bottom-up approaches consist in the formation of large nanostructures from atoms and molecules, in contrast to the top-down methods that reduce bulk structures to nanoparticles. Hydrothermal treatment is a simple, cost-effective, and environmentally friendly method, in which the precursor is mixed with water as a solvent, in an autoclave heated beyond the boiling point of water and under autogenous pressure[45]. During the synthesis, without the need of further calcination, partial crystallization takes place, which is influenced by different parameters such as temperature, pressure, reaction time and pH. The latter influences the rate of growth of the crystals and therefore their size. An increase in pH allows a slower precipitation of hydroxide and therefore the formation of a crystalline solid. Also, the temperature and the reaction time involve structural changes.

Hydrothermal treatment is therefore considered as a more sustainable method since water as a reaction solvent is used and allows to operate in relatively mild reaction conditions.

Although perovskites such as barium titanate and calcium titanate have appropriate properties as photocatalysts, it is necessary to develop different strategies to improve the photoactivity and enable the materials to exploit the full sunlight spectrum. Strategies like using visible-active dyes or polymer conjugates to sensitize the photocatalyst, and doping the semiconductor with heteroatoms (O, C, N, S) or metals (Cu, Ni, Zn, Fe) by introducing new intra-gap energy levels have been used.

An alternative strategy consists in associating the semiconductor with a co-catalyst able to absorb in the visible range by promoting the presence of heterojunctions which are reported to reduce the rate of recombination. Due to the different band nature of the semiconductors, there are three types of heterojunctions as shown in Figure 8[28].

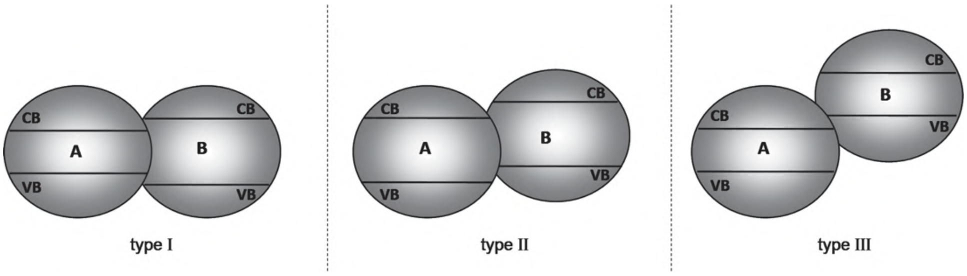

Figure 8: *Types of heterojunctions*[28]

1.4.1 DOPING

The semiconductor can present problems of conductivity, selectivity, and absorption, in particular most materials absorb UV radiation, which however constitutes only 10% of the solar spectrum. To overcome these issues $BaTiO_3$ and $CaTiO_3$ perovskites were doped with non-metal dopants. This permits to introduce new intra-gap energy levels reducing the band gap and shifting the absorption of radiation in the visible region[43]. In general, dopants tend to occupy the interstitial or substitutional sites of the semiconductor to create localized energy levels as reported in Figure 9.

The heteroatoms that will be considered are nitrogen and carbon, which are available, inexpensive, and non-toxic. Nitrogen is gaining considerable attention because of its ability for narrowing the band gap, huge stability, lower electronegativity, and lower ionization energy than oxygen. Nitrogen and oxygen have also similar ionic radius; this helps mixing nitrogen 2p orbital with oxygen 2p orbital improving photocatalytic activity. From literature, it is reported that nitrogen replaces some oxygen atoms creating vacancies and shifting the absorption band from UV to visible range[28]. *Humayun et al.* synthetized N-doped $LaFeO_3$ perovskite and they reported that since the ionic radius and the electronegativity of O^{2-} and N^{3-} are similar, the substitution of N^{3-} on oxygen vacancies is facilitated. In addition, since the potential energy of N 2p orbitals is higher than that of O 2p, the band gap is effectively reduced[44]. In particular, this element favors the interaction with CO_2 and could act as adsorption site in the photoreduction. In addition, the functional groups that contain nitrogen permit strong chemisorption of the intermediates leading to higher selectivity to methane[45]. On the other side, carbon can improve the photoactivity, stabilize the material and promote the absorption of the molecules on the catalyst surface. As nitrogen, carbon 2p orbital mixed with oxygen 2p orbital help narrowing the band gap[30].

Nitrogen and carbon precursors can be mixed with perovskites precursors and water in the autoclave to make the hydrothermal treatment. It is important to adjust the pH to a constant value using a base such as NaOH in order to facilitate the entrance of the catalytic precursor into the perovskite crystal lattice. The co-doping can increase the photoactivity of the perovskites under both UV and solar light[30].

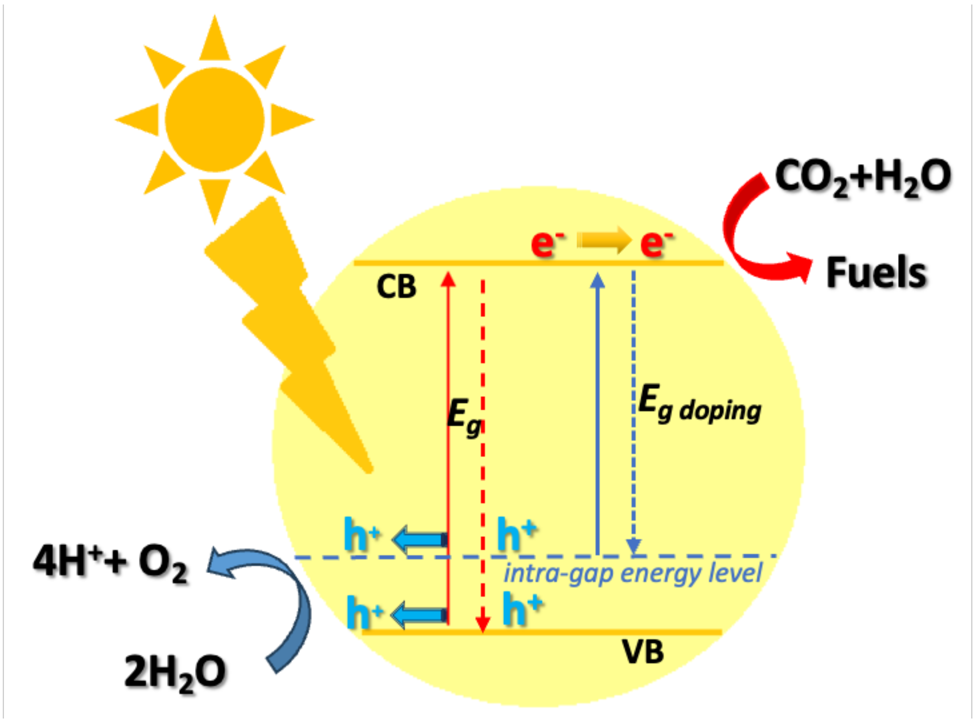

Figure 9: *Influence of doping a photocatalyst.*

1.4.2 CO-CATALYST

A co-catalyst can be associated to $BaTiO_3$ and $CaTiO_3$ in order to slow down the recombination. In the literature, it is reported that the using of nanoparticles or nanostructured materials can afford large surface areas[46]. Carbon dots (CDs) are an emerging type of photocatalytic materials that can be active in the photoreduction of carbon dioxide. *Kulandaivalu et al.* reported the use of carbon dots supported on Cu_2O for carbon dioxide photoreduction in the gas phase under visible light irradiation. They obtained a high selectivity toward ethane and an improvement in the photostability of the catalytic system[47]. Moreover, carbon dots are also explored in organic pollutant degradation, hydrogen generation, NOx removal and organic transformations[48]. CDs are carbon spherical nanoparticles with the size below 10 nanometers, that have high chemical stability, fluorescent properties, good photogenerated charge transfer ability, easy surface modification, biocompatibility, and low toxicity[49]. CDs are composed of a nanocrystalline core and an amorphous shell rich in functional groups such as C=O and COOH, which accelerate the separation between electrons and holes, and they are characterized by a large π conjugated system that is correlated to the ability of separating charge electron-hole pairs and improving the photocatalytic activity. Due to their narrow band gap, CDs have also the ability to increase the range of wavelength absorption and could act as active sites in the CO_2 photoreduction[50]. In the literature, *Ong et al.* has reported the use of carbon dots as co-catalysts to modify g-C_3N_4 (graphene carbon nitride), that has improved the adsorption of nonpolar CO_2 and has enhanced the generation of methane[51]. Then, carbon dots can be coupled with barium and calcium titanates.

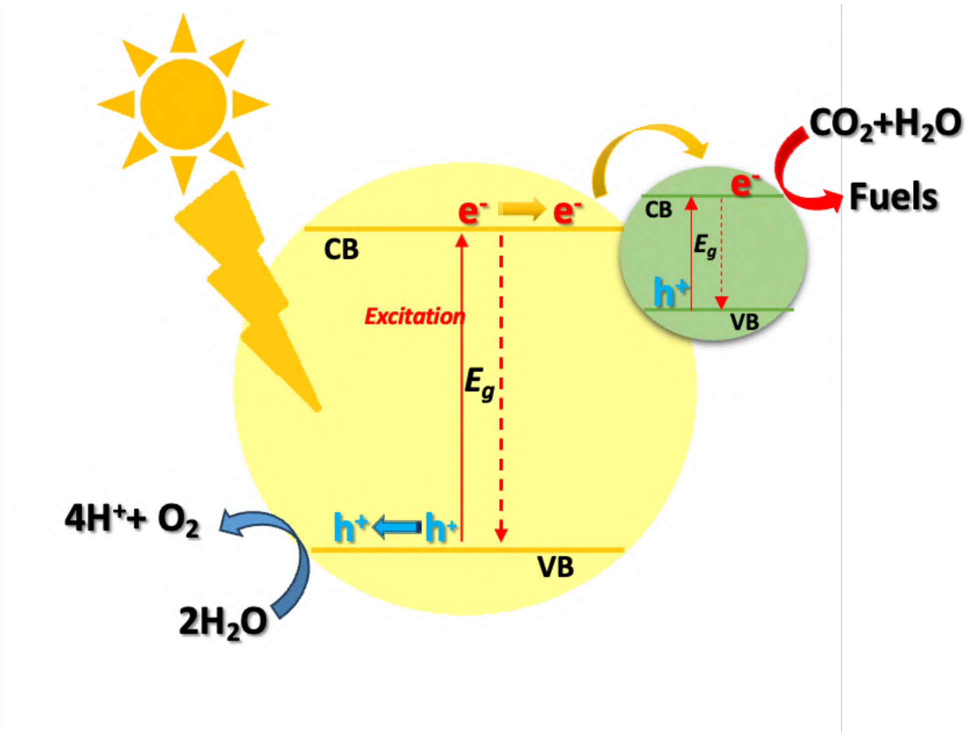

Figure 10: *Semiconductors effect of associating a co*-catalyst.

2. GOAL OF THE THESIS

The goal of this thesis is the design of efficient photocatalytic materials for developing CO_2 photoreduction under solar light.

In particular, the study focused on perovskites such as $BaTiO_3$ and $CaTiO_3$, which are gaining attention for their photocatalytic properties, that were implemented through doping with heteroatoms and associating a co-catalyst. Ammonium chloride and glucose were used respectively as nitrogen and carbon sources. Also chitosan, that is a polysaccharide of natural origin that constitutes the crustacean shells of shrimp, crab, and crawfish, was used as both nitrogen and carbon source[52]. The bare and doped perovskites were synthetized by hydrothermal method, as an efficient and scalable bottom-up approach without the need of further calcination.

On the other side, carbon dots were synthetized by microwave-assisted method which uses microwave radiation to carbonize directly organic precursors into CDs in a shorter reaction time[53]. These catalysts were compared to P25, the benchmark material. A gas-phase batch reactor was used to carry out the catalytic tests under both UV light and solar simulator, and then compared to the liquid phase tests.

The use of solar light and the upcycling of CO_2 is part of a circular economy perspective in line with the 2030 Agenda and the requirements of the current energy transition.

3. EXPERIMENTAL PART

3.1 MATERIAL SYNTHESIS

3.1.1 HYDROTHERMAL SYNTHESIS OF BARIUM TITANATE ($BaTiO_3$) AND CALCIUM TITANATE ($CaTiO_3$)

Barium titanate and calcium titanate were prepared via hydrothermal synthesis. 50 mL of 0,1 M $BaCl_2 \cdot 2H_2O$ (5 mmol) as barium precursor or $CaCl_2$ as calcium precursor and 1,5 mL of titanium tetraisopropoxide (TTIP) were mixed in a beaker. The pH value was adjusted to 12 by adding a 4M solution of sodium hydroxide (NaOH) dropwise. The solution was put under stirring with the rate of 300 rpm for 20 min until being homogeneous, then transferred into a Teflon vessel of 100 mL capacity. Then, it was put in the autoclave heated at 180°C in autogenous pressure for 8 h (Figure 11). After the reaction was finished, the autoclave was cooled down to room temperature. The resulting mixture was filtered on a Gooch crucible and washed with distilled water and ethanol. The white solid sample was dried in the oven at 110°C for 12 h.

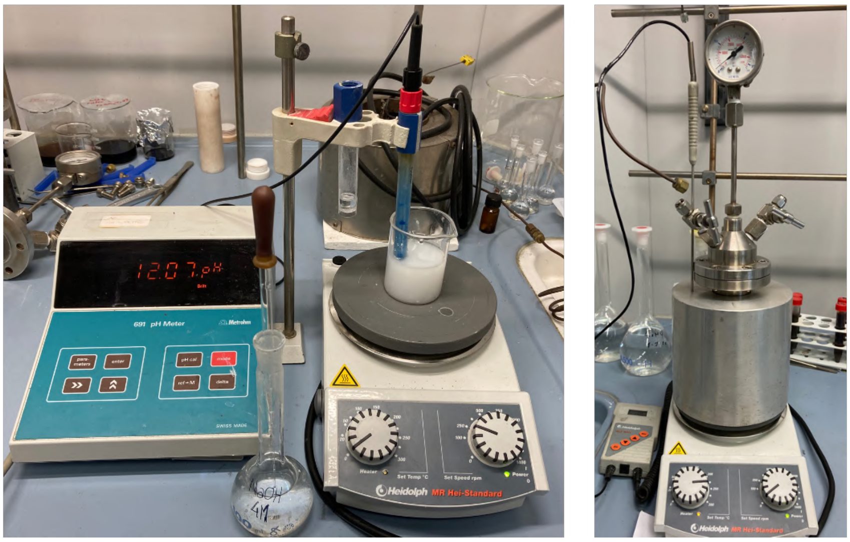

Figure 11: *Procedure for perovskites preparation*

3.1.2 HYDROTHERMAL SYNTHESIS OF DOPED PEROVSKITES

Doped barium titanate and doped calcium titanate were prepared by hydrothermal synthesis.

50 mL of 0,1M $BaCl_2 \cdot 2H_2O$ (5 mmol) as barium precursor or $CaCl_2$ as calcium precursor, 1,5 mL of titanium tetraisopropoxide (TTIP) and a certain amount of nitrogen and/or carbon precursors were mixed in a beaker.

The pH value was adjusted to 12 by adding a 4M solution of sodium hydroxide (NaOH) dropwise. The solution was put under stirring with the rate of 300 rpm for 20 min until being homogeneous and then transferred into a Teflon vessel of 100 mL capacity. The autoclave was heated at 180°C for 20 h and then cooled down to room temperature at the end of the reaction. The resulting mixture was filtered on a Gooch crucible and washed with distilled water and ethanol. The cream-colored solid sample was dried in the oven at 110°C for 12 h. The name of doping precursors and their amount are reported in Table 2.

Table 2: *Ratios and quantities of doping precursors.*

SAMPLE	MATERIAL	DOPING PRECURSOR(S)	RATIO	QUANTITY (mmol)
NBaT **NCaT**	N-$BaTiO_3$ N-$CaTiO_3$	Ammonium chloride (NH_4Cl)	1Ba:1Ti:1N 1Ca:1Ti:1N	5,0
CBaT **CCaT**	C-$BaTiO_3$ C-$CaTiO_3$	Glucose dextrose	1Ba:1Ti:1C 1Ca:1Ti:1C	0,8
CNBaT **CNCaT**	CN-$BaTiO_3$ CN-$CaTiO_3$	Ammonium chloride (NH_4Cl) and Glucose dextrose	1Ba:1Ti:0,5C:0,5N 1Ca:1Ti:0,5C:0,5N	2,5 NH_4Cl and 0,4 Glucose
ChitBaT	Chitosan $BaTiO_3$	Chitosan	1Ba:1Ti:1C	0,5

3.1.3 MICROWAVE-ASSISTED SYNTHESIS OF CARBON DOTS AND SUPPORTED CARBON DOTS

Carbon dots were prepared via microwave-assisted method. 0,1 g of o-phenylenediamine were dissolved in 15 mL of ethanol in a beaker and irradiated in a microwave at 180°C for 15 minutes. To obtain CDs/P25 and CDs/$BaTiO_3$ in situ, 2 mg of the reagent and 40 mg of support were dissolved in ethanol and irradiated in a microwave in the same conditions.

After the solution was filtered with 0,22 µm WHATMAN filter papers and dialyzed in ethanol for 24 hours with 1 kDa SPECTRA/POR membrane to remove inorganic components and other small molecules (Figure 12). The obtained solution of carbon dots was freeze-dried for 24 hours. These obtained carbon dots were labelled as CDs.

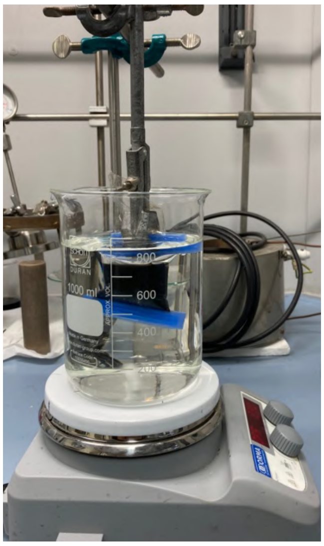

Figure 12: *Dialysis of carbon dots*

3.1.4 WET IMPREGNATION OF CARBON DOTS ONTO $BaTiO_3$ and P25

Titanium dioxide was used in its commercial form Degussa P25. To obtain CDs/P25 and CDs/$BaTiO_3$, the support was impregnated with 5 wt% CD_s that were previously synthesized. Carbon dots were dissolved in 2 mL of ethanol and sonicated for 30 minutes, then they were added dropwise on the support with a Pasteur pipette, following an incipient wetness impregnation procedure. During the dripping, the powder was continuously stirred until a grey powder was obtained, which was then placed in the oven at 110 for 12 h. The names of carbon dots and the used synthesis methods are reported in Table 3.

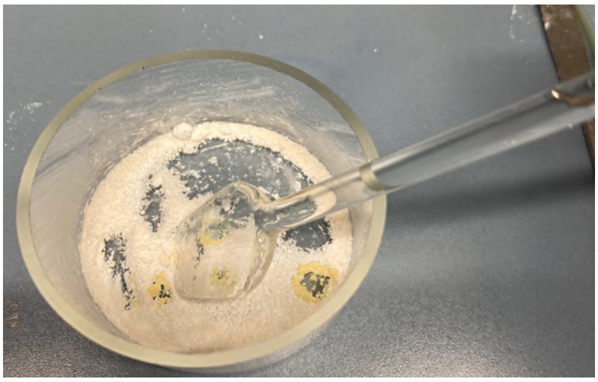

Figure 13: *Procedure of wet impregnation of carbon dots to the supports.*

Table 3: *Carbon dots names and synthesis methods.*

SAMPLE	MATERIAL	SYNTHESIS METHODS
CDs	CDs	Microwave
CD-TW	CDs/P25	Microwave-Wet Impregnation
CD-BW	CDs/$BaTiO_3$	Microwave-Wet impregnation
CD-TS	CDs/P25	Microwave-Situ
CD-BS	CDs/$BaTiO_3$	Microwave-Situ

3.2 CHARACTERIZATIONS

3.2.1 ELEMENTAL ANALYSIS

The samples were analyzed in their chemical composition by elemental analysis. This technique allows to determine the amounts of carbon, hydrogen, nitrogen, sulfur present in the sample under analysis. The analyses were performed in a UNICUBE organic elemental analyzer, consists of two reactors: a combustion reactor, which operates at 1100°C in the presence of WO_3 (oxidation catalyst) and a reduction reactor operating at 600°C in the presence of CuO (reduction catalyst). Before carrying out the analysis, the samples were dried in the oven to remove any traces of water present inside them. Then, 2 mg of sample were weighted and placed in a tin sample holder, which was closed and folded correctly to eliminate the presence of air inside. The sample was inserted into the autosampler. In the first reactor, the sample is burned, and the decomposition gases are formed. These arrive at the reduction reactor and are then conveyed into a trap, which releases the gases at different temperatures to a thermal conductivity detector (TCD). The signal is proportional to the concentration of each gas and reveals, thanks to an internal calibration of the instrument, the composition in C, H, N and S of the samples. The oxygen content, that isn’t revealed because it is the comburent of the analysis, can be calculated by difference according to Equation 1:

$$O\% = 100 - (C\% + H\% + N\% + S\% + ash\%)$$ **Equation 1**

3.2.2 SEM-EDX and TEM

To determine the morphology of perovskites and carbon dots samples, scanning electron microscopy (SEM) analysis was applied. This technique was performed using an electron microscope (Electron Microscopy LEO 1525) whose source generates a beam of electrons, which interacts with the atoms that constitute the sample under examination, allowing the consequent emission of other electrons from the sample. A detector collects the signal generated by the interaction between the electron beam and the sample and thus reconstructs a high-resolution image of the material[54].

The X-ray energy dispersion (EDX) technique was used to determine the types and the amounts of elements in the sample. In this study, a scanning electron microscope (Bruker Quantax EDS) was used. The microscope is equipped with a detector positioned, at a given angle, very close to the sample and can measure the energy of incoming x-rays photons.

Transmission electron microscopy (TEM) was applied to determine the morphology of the internal structure of the perovskites and carbon dots. In this case, a beam of electrons is transmitted through the sample, interacting with the atoms, in order to create an image. The instrument used in this work was Philips 208.

The analyses were conducted by Dr. Alessandro Di Michele at the Department of Physics and Geology at the University of Perugia.

3.2.3 NITROGEN PHYSISORPTION

All the samples were analyzed by nitrogen physisorption. The technique consists of the physical adsorption of nitrogen and subsequent desorption on the surface of a sample. Weak reversible interactions are established between adsorbate and the substrate. The instrument used for these measurements was Micromeritics TriStar II PLUS. Before starting the analysis, 100 mg of sample were weighted, and then pre-treated at 200°C under vacuum for 2,5 h to remove physically absorbed impurities on the surface. After that, the sample was cooled and weighted again prior to the beginning of the measurement.

This analysis enables to obtain information of the surface area calculated through the BET (Brunauer-Emmett-Teller) or Langmuir theory, the micropore area by t-plot analysis, and the pore size distribution by BJH (Barrett-Joyner-Halenda). From the physisorption measurement, an adsorption isotherm is obtained, that is a curve that represents the relationship between the amount of adsorbed gas and relative pressure. From the isotherm it is possible to obtain information about the type of porous system that constitutes the sample[55]. In Figure 14, the 6 IUPAC adsorption desorption isotherms which describe microporous (with pore diameter < 2 nm), mesoporous (2 nm < diameter < 50 nm) and macroporous (diameter > 50 nm) systems are reported.

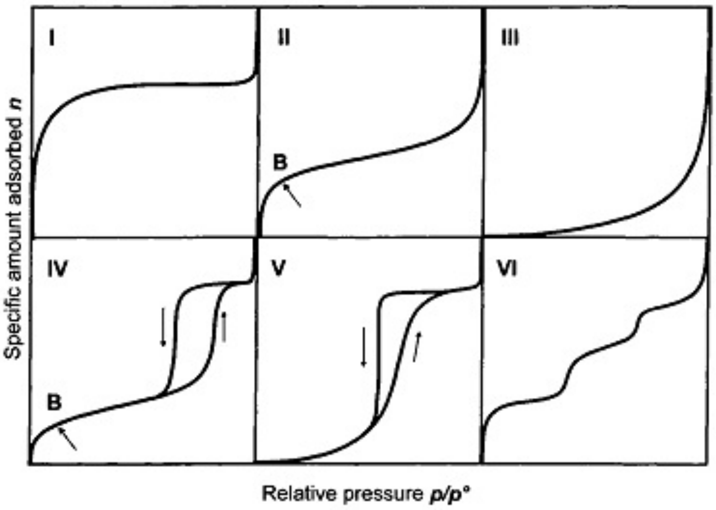

Figure 14*: IUPAC adsorption desorption isotherms*[56]*.*

3.2.4 FT-IR SPECTROSCOPY

Infrared spectroscopy was applied to determine the functional groups present on the surface of the samples. It is an analytical technique based on the interaction between electromagnetic radiation and matter. When a molecule is hit by infrared radiation at a certain frequency, the energy released by the radiation is converted into vibrational energy. Then the molecule is promoted from its fundamental vibrational state to an excited one. The energy gap between the two vibrational states determines the formation of a band which can be related to different functional groups present at the surface[57]. The Perkin Elmer Precisely Spectrum One IR spectrometer was used to carry out the analysis. Before starting the analysis, the samples were dried in the oven at 110°C overnight in order to remove any traces of water present. After the tablet composed by KBr and of a small amount of the sample was prepared. The resulting pellet was inserted into the instrument, which was set in a wavenumber range between 4000 and 400 cm^{-1} and with a resolution of 4 cm^{-1}.

3.2.5 DIFFUSE REFLECTANCE SPECTROSCOPY (DRS)

Diffuse reflectance spectroscopy (DRS) was applied to determine the perovskites interaction with light and their band gaps. DRS is an analytical, non-destructive technique that involves a source of white light and an integrating sphere coated with an internal standard, that is the reference. The radiation can be absorbed, reflected, or scattered by the integrating sphere or by the sample that is placed on a holder. The reflectance spectrum gives the relative percentage of diffuse reflectance intensity of the sample surface (R%) versus the wavelength of the radiation. In this thesis, Cary 100 Agilent spectrometer was used to carry out the analysis working at room temperature in the range of 200-800 nm (UV-vis-NIR) and $BaCl_2$ was used as internal reference. A thick film of the powder sample was placed in a plastic holder with a quartz window.

In order to determine the absorbance of the samples, spectra are reported in the Kubelka-Munk function (Equation 2) which is proportional to the absorbance, assuming the infinitely thick samples.

$$F(R) = \frac{(1-R)^2}{2R} = K/S \quad \textbf{Equation 2}$$

where R, K, S are respectively the reflectance, absorption, and scattering coefficients of the sample[58]. The Tauc plot was calculated for each sample to determine the band gap energy (E_g).

3.2.6 X-RAY DIFFRACTION (XRD)

To determine the crystal structure of the materials X-Ray Diffraction was used.

When x-rays affect a crystal in the form of powder, an interference pattern is generated. This results in a diffractogram that reports the intensity of the peaks as a function of 2θ. Each peak is characterized by a particular Miller index, which is composed by three numbers representing the Miller planes. These are a family of planes parallel to each other and defined by a distance d. To determine the interplanar distance Bragg's law is applied:

$$2d(sen\theta) = n\lambda$$ **Equation 3**

where λ is the wavelength of the incident radiation and θ is the Bragg angle that corresponds to the maximum of the peak. From this equation and through other mathematical operations, it is possible to obtain information about the crystal lattice of the sample under examination[54].

In this work, X-ray Diffraction (XRD) was performed with Bruker D8 Advanced diffractometer equipped with Cu Kα radiation (λ = 1.5418 Å) and compared with the ICDD-ICPDS powder diffraction file database.

The analyses were conducted by Prof. Giuseppe Cruciani at the Department of Physics and Earth Science at the University of Ferrara.

3.2.7 UV-VIS SPECTROSCOPY

UV-Vis spectroscopy was used to determine the absorption range and to analyze the methylene blue solutions of carbon dots. It is an analytical technique that involves light, in the range between UV and visible, that is absorbed or transmitted through a sample. A certain amount of energy is required to promote electrons from a lower energy state to a higher one and this energy is inversely proportional to the wavelength. For a substance the absorption of light occurs at different wavelengths depending on the bonding structure of the same. The whole wavelengths are collected in an absorption spectrum, that reports the absorbance (A) of the sample versus the different wavelengths in the UV-Vis range. Absorbance is equal to the logarithm of the fraction between intensity of light (I) before and after passing through the sample (I_0), where the fraction I_0/I is transmittance. Using the Lambert-Beer law (Equation 4) and constructing a calibration curve, given a specific absorbance value it is possible to determine the concentration of the sample.

$$A = \log\frac{I}{I_0} = -logT = \varepsilon bC$$ **Equation 4**

where ε is the molar extinction coefficient that is specific for the substance, and b is the path length[57].

In this work Cary 100 Agilent spectrometer was used to carry out the analysis working at room temperature in the range of 200-800 nm (UV-vis-NIR) using quartz cuvettes. Milli-Q water was used as the solvent and as the blank for the analysis.

3.2.8 PHOTOLUMINESCENCE SPECTROSCOPY

Photoluminescence spectroscopy (PL) and photolumiscence excitation (PLE) were applied to investigate the emission of light from a material upon light excitation. During this analysis, the atoms or molecules are excited by the absorption of a beam of electromagnetic radiation. The excited species then relax to the ground state by emitting energy in the form of photons. An emission spectrum and excitation spectrum are therefore generated[57].

These analyses were carried out using a spectrofluorometer (Jasco FP-750) with a 150 W Xenon lamp (270-730 nm) as the excitation source. The emission spectrum was measured in the range 250-600 nm.

3.3 PHOTOCATALYTIC TESTS

3.3.1 GAS PHASE PHOTOREDUCTION REACTION

CO_2 photoreduction with water vapor was carried out in a gas phase batch reactor made of boron silicate (volume 1,9 mL). The catalyst (10 mg) was first dissolved in 2 mL of ethanol into a vial, sonicated for an hour, and then deposited at 200°C with a Pasteur pipette as a thin film in the reactor. In order to evaporate any traces of ethanol, the reactor was put in the oven for an hour. A 125 W mercury UVA lamp (spectral range 315-400 nm; Helios Italquartz, GN125RZS) and a solar simulator (model number 10500; ABET technologies; 150 W Xenon arc lamp with AM 1.5G atmospheric filter) were used as light source, with an irradiance of 40 W/m^2 and 1000 W/m^2, respectively. A schematic representation of the photoreduction system is reported in Figure 15 and the gas phase reactor illuminated by solar simulator light is shown in Figure 16. The gas phase reaction mixture was composed by compressed CO_2 (99,99%) and water vapor with a CO_2/H_2O molar ratio of 13,3. The reaction was conducted at 40°C for 6 hours at atmospheric pressure. Before performing tests, the system was purged with a helium to remove any traces of impurities. Then blank tests were carried out in the presence of gas reagents and light. The reaction was performed for 6 hours. After that, the reaction products (CH_4, CO, H_2) were analyzed by gas cromatography (Agilent 6890 Plus GC, Porapak Q column), with a thermoconducibility detector (TCD) using Helium as gas carrier. The results are expressed in TON turn over number, according to the Equation 5.

$$TON = \frac{\mu\text{mol product}}{g\ catalyst}$$ **Equation 5**

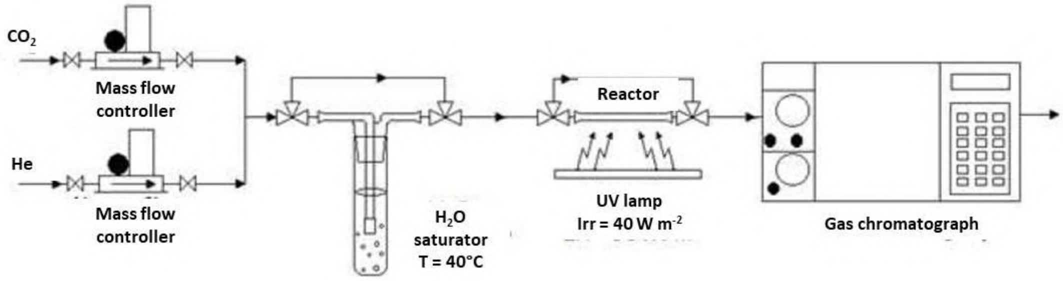

Figure 15: *Schematic representation of gas phase photoreduction system.*

Figure 16: *Gas phase reactor illuminated by solar simulator light.*

3.3.2 LIQUID PHASE PHOTOREDUCTION REACTION

Liquid phase photoreduction tests were conducted in the lab of Prof. Ilenia Rossetti at the Department of Chemistry at the University of Milan . The same catalysts synthetized and used in gas phase were tested in a batch pressurized reactor that is a 1,7 L autoclave with a UV 250 W mercury medium pressure lamp (Figure 17). To degas the system, before performing the tests, the autoclave was loaded with 1,2 L of milli-Q water, 30 mg/L of catalyst, 1,6 g/L of sodium sulfite Na_2SO_3 as hole scavenger, and CO_2 was flowed at 2 bar. The autoclave was heated at 30°C for 30 minutes under stirring at 400 rpm in the absence of illumination. Then, three samples of liquid (14 mL each) were collected from the autoclave and analyzed with iodometric titration to determine the initial concentration of the hole scavenger. This material was loaded to reduce electron-hole recombination by donating electrons to the valence band avoiding hole accumulation[59]. After degassing, CO_2 was dissolved under 18 bars of pressure at 80°C, the lamp was turned on and the reaction was carried out for 6 hours at basic pH with about 120 W/m^2 of irradiance. At the end of the reaction, four samples of reaction liquid were collected and centrifugated to remove solid impurities.

The gas products (CH_4, CO, H_2) were analyzed by gascromatography (Agilent Technology 7890 A, double column PlotQ and Molecular Circular) using a TCD detector.

The liquid products (HCOOH, CH_3OH, sulfite, CO_3^{2-}) were analyzed by high performance liquid chromatography (Agilent 1220 Infinity, Alltech OA-10308, 300 mm_7,8 mm column) with UV and refractive index detectors. The eluent was an aqueous solution of H_3PO_4 (0.1 wt %). The iodometric titration was re-performed to determine if the hole scavenger had reacted and so its residual amount.

The iodometric titration is a retro titration that is performed with 5 mL of potassium iodide (KI), 5 mL of potassium iodate (KIO_3), 1 mL of HCl, 1 mL of the sample and a starch solution as an indicator. The titrant is sodium thiosulphate. As reported in Equation 6, known concentrations of KIO_3 and KI in acid environment produce iodine in the metallic state, that subsequently oxidizes sulfite into sulfate generating electrons for the valence band. Then the excess of iodine is titrated with sodium thiosulphate ($Na_2S_2O_3$).

Equation 6:

$$IO_3{}^- + 6H^+ + 5I^- \rightleftharpoons 3H_2O + 3I_2$$

$$I_2 + H_2O + SO_3{}^{2-} \rightleftharpoons 2I^- + SO_4{}^{2-} + 2H^+$$

$$I_2 + 2Na_2S_2O_3 \rightleftharpoons 2\ NaI + Na_2S_4O_6$$

The results are expressed in TON turn over number (μmol/g cat).

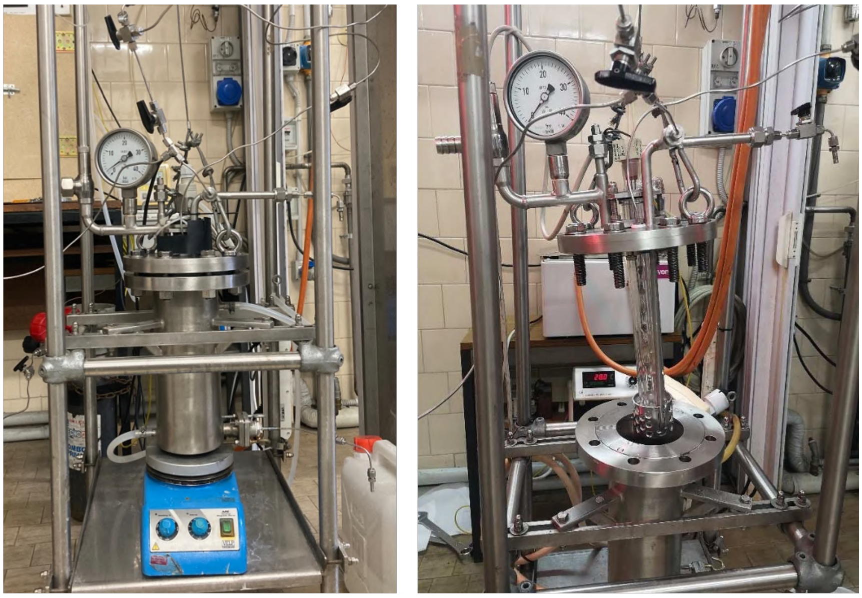

Figure 17: *Liquid phase photoreduction apparatus.*

3.3.3 PHOTODEGRADATION OF METHYLENE BLUE

To determine carbon dots photoactivities in water under both UV and solar light, photodegradation of methylene blue was performed. A 125 W mercury UV lamp (spectral range 315-400 nm; HG100; Jelosil Srl) and a solar simulator (model number 10500; ABET technologies; 150 W Xenon arc lamp with AM 1.5G atmospheric filter) were used as light sources with an irradiance equal to 40 W/m^2 and 1000 W/m^2 respectively.

A 10^{-3}M standard aqueous solution of methylene blue (MB) was prepared and then diluted to a 10^{-5} M standard solution, that was put in a beaker under stirring. In absence of illumination (dark) 5 mL of the solution were taken, introduced into a 10 mL flask, and diluted with 5 mL of milli-Q water. Then, 20 mg of catalyst (perovskite or carbon dots) were put into the MB solution and left stirring at 300 rpm for 20 minutes to homogenize the solution. After, the solution was irradiated with UV or visible light radiation and, at regular intervals (0, 10, 20, 30, 45, 60, 90, 120 min), 5 mL of the methylene blue solution were taken and analyzed with UV-vis spectroscopy. The photodegradation system is shown in Figure 18.

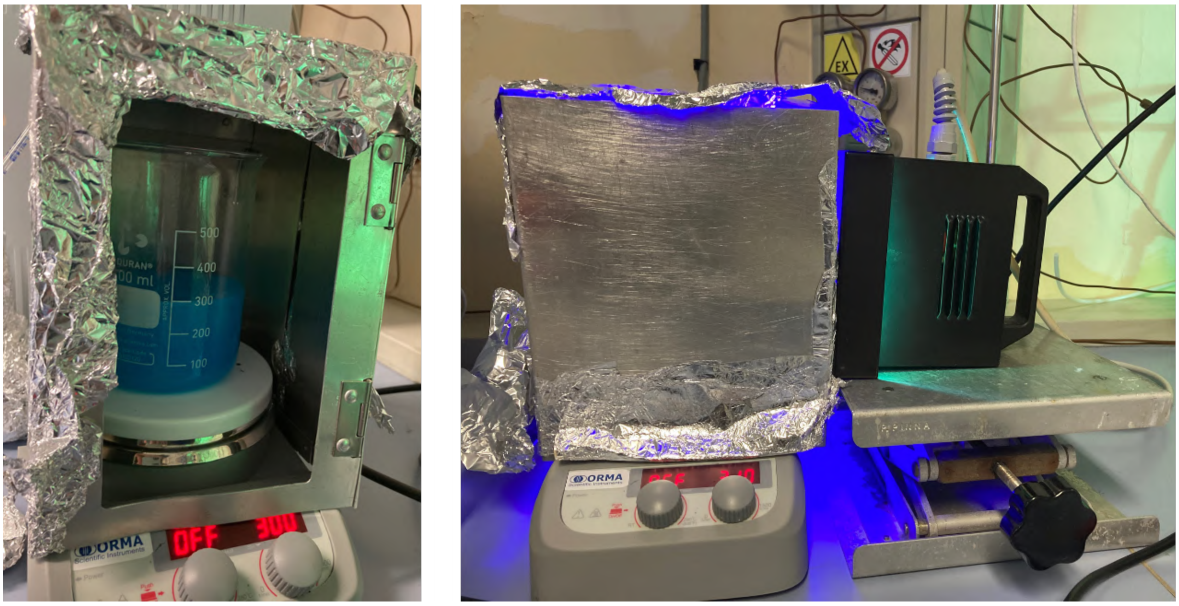

Figure 18: *Methylene blue photodegradation rig.*

4. RESULTS AND DISCUSSION

4.1 C, N AND C-N DOPED SAMPLES

4.1.1 STRUCTURAL AND MORPHOLOGICAL CHARACTERIZATIONS

XRD analysis was performed to determine the crystal structure of the catalysts. XRD spectra for Ba-based materials are reported in Figure 19.

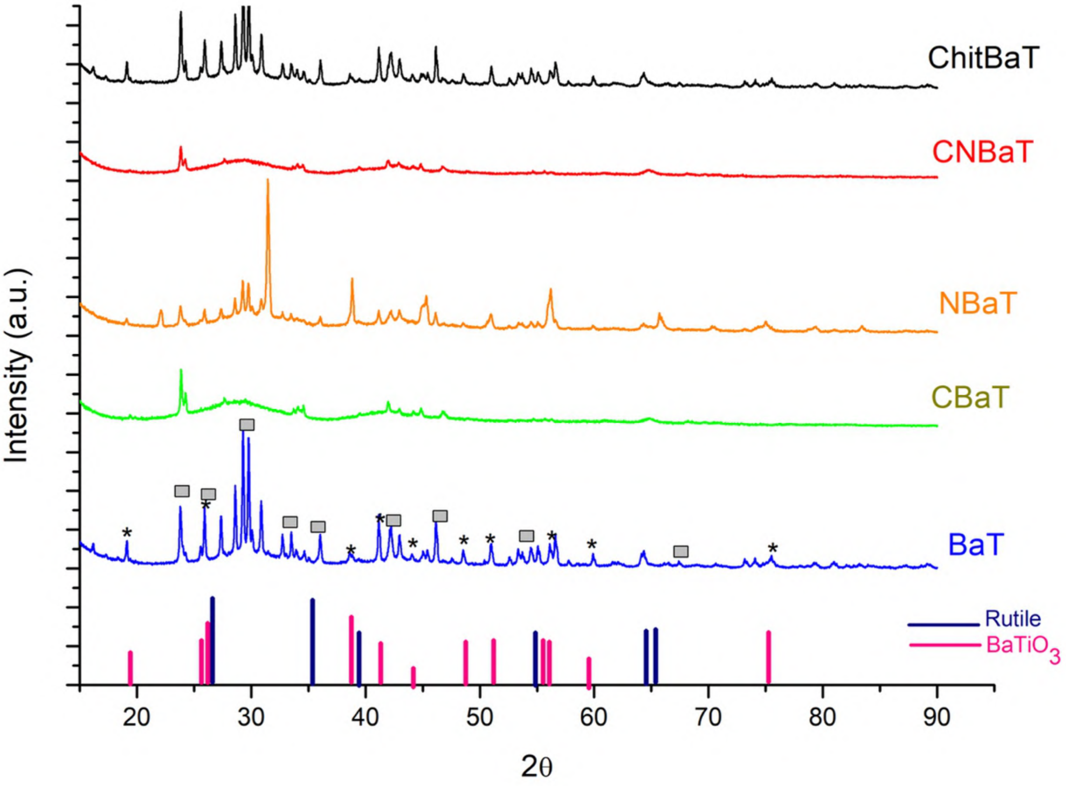

Figure 19: *XRD spectra of Ba-perovskites: BaT (blue), CBaT (green), NBaT (orange), CNBaT (red), ChitBaT (black). Asterisk (*) denoted BaT phase, rectangles denoted BaCO$_3$.*

In bare BaTiO$_3$ XRD pattern, different crystalline phases were identified. Traces of barium carbonate (BaCO$_3$) were identified and attributed to the superficial adsorption of CO$_2$ from air during the synthesis procedure[60]. Although an increased affinity for CO$_2$ is desirable, a too high affinity could be an issue, resulting in the fast saturation of active superficial sites. The XRD pattern showed the presence of BaTiO$_3$ cubic structure derived from the characteristic peaks (2θ= 19°, 39°, 45°, 51°, 56°) denoted with asterisk (*) in Figure 19, as reported in the study of *Phan et al.*[61]. CBaT showed an amorphous structure, possibly related to a lattice distortion due to C doping of BaT. *Hernandez et al.*, previously studied carbon-doped $NaTaO_3$, and observed that carbon can affect the lattice parameters of the unit cell[62]. Similarly, CNBaT had an amorphous-like profile. The XRD patterns of ChitBaT were like bare $BaTiO_3$. Thus CN-doping with chitosan seemed not cause a change in the crystalline phase. *Yuan et al.* reported that doping titania with urea did not cause a modification of crystalline structure, but using an excess of urea changed the system to amorphous structure[63]. NBaT diffractogram was also similar to that of BaT, with a slight shift to higher angles, which was attributed to the incorporation of nitrogen to substitute some oxygen atoms, without a change in the crystal structure[44]. *Alammar et al.* reported an N-doped $SrTiO_3$ system with shifted the diffraction peaks at higher angles, which was attributed to a shrinkage of the structure[64]. In addition, the presence of rutile phase in N-$BaTiO_3$ was determined. This was attributed to the presence of soluble titanium species in the forms of $Ti(OH)_4$ and $HTiO_3^-$ during the hydrothermal synthesis. In this case, the pH was kept constant to 9 to facilitate nitrogen insertion in the perovskite lattice. The pH is an important parameter and in general high value are requested for the synthesis of high purity $BaTiO_3$[65]. Therefore, the lower pH likely led to the side formation of TiO_2 species, as shown in the diffractogram. Also in these cases, traces of $BaCO_3$ were detected.

XRD spectra for Ca-based materials are reported in Figure 20.

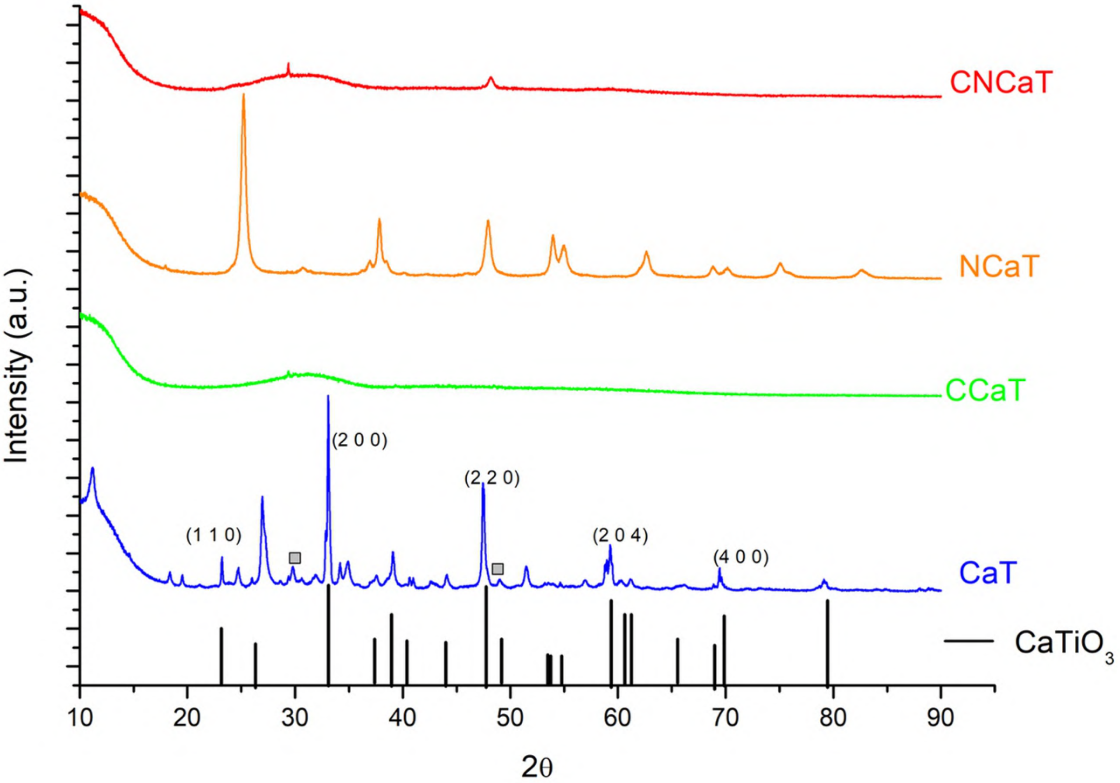

Figure 20: *XRD spectra of Ca-based perovskites: CaT (blue), CCaT (green), NCaT (orange), CNCaT (red). Rectangles denoted $CaCO_3$.*

The XRD pattern of bare $CaTiO_3$ confirmed its crystalline phase formation. The crystal planes of (1 1 0), (2 0 0), (2 2 0), (2 0 4) and (4 0 0) and 2θ= 34°, 39°, 45° were matched with the orthorhombic phase of $CaTiO_3$[66]. CCaT showed an amorphous structure likely related to the introduction of carbon in the crystalline structure. However, in the study of *Olivo et al.* the introduction of carbon into titania structure did not affect its crystalline phase[30]. In addition, *Yahya et al.* observed the formation of $CaCO_3$ on the samples exposed to CO_2[67]. This evidence supports the possible carbon dioxide adsorption on $CaTiO_3$ and the consequent formation of traces of $CaCO_3$ on the surface. The CO_2 adsorption capacity could be further confirmed by TPD measurements. CNCaT had a similar profile to CCaT showing an amorphous structure. There were also two peaks at 2θ of 29,4°and at 48,2° that were attributed to the formation of $CaCO_3$, as reported in the work of *Yahya et al.*[67]. Notably, NCaT showed a slight shift toward lower 2θ values compared to that of CaT. At 2θ =25° the NCaT peak seemed to correspond to the peak at 34° of CaT, in addition the CaT peak at 48° was shifted to 39° in NCaT pattern. In the work of *Yang et al.,* $FeVO_4$ was doped with nitrogen, and the peak at 2θ= 25° shifted toward lower angles compared to the undoped material. This should be due to oxygen ions substituted by nitrogen ions[68]. Moreover, NCaT reported no detectable change in the crystal phase, suggesting that the doping process was not as extensive as to have a remarkable effect on lattice parameters[69]. In general, the shift to lower angles is correlated to the expansion of the unit cell because the planes become more distant and, considering the mutual space, move to smaller angles[54]. The increase of the unit cell parameter could be related to nitrogen insertion into the $CaTiO_3$ lattice. However, the same N-doping in $BaTiO_3$ structure demonstrated a shift to higher angles. Calcium ions are characterized by smaller ionic radius than the barium ones, and it is possible that the insertion of heteroatoms in the overall structure of $CaTiO_3$ distanced the planes and increased the unit cell[70]. In addition, nitrogen ionic radius (1,5 Å) is slightly higher than that of oxygen ones (1,4 Å), resulting in a possible expansion of unit cell[44]. Moreover, C and CN-doping in both perovskites showed similar XRD profiles presenting amorphos structures. Carbon ionic radius is bigger than nitrogen and oxygen, hence it is possible that C introduction in the lattice led to more marked distortion of the crystal phase.

Scanning electron microscopy (SEM) analysis was applied to investigate the surface morphology of the catalysts. This technique was paired with EDX to determine the distribution and the presence of defined elements in the materials. The high-resolution images of the barium perovskites are reported in Figure 21*.* SEM-EDX images and spectra are showed from Figure 22 to Figure 31.

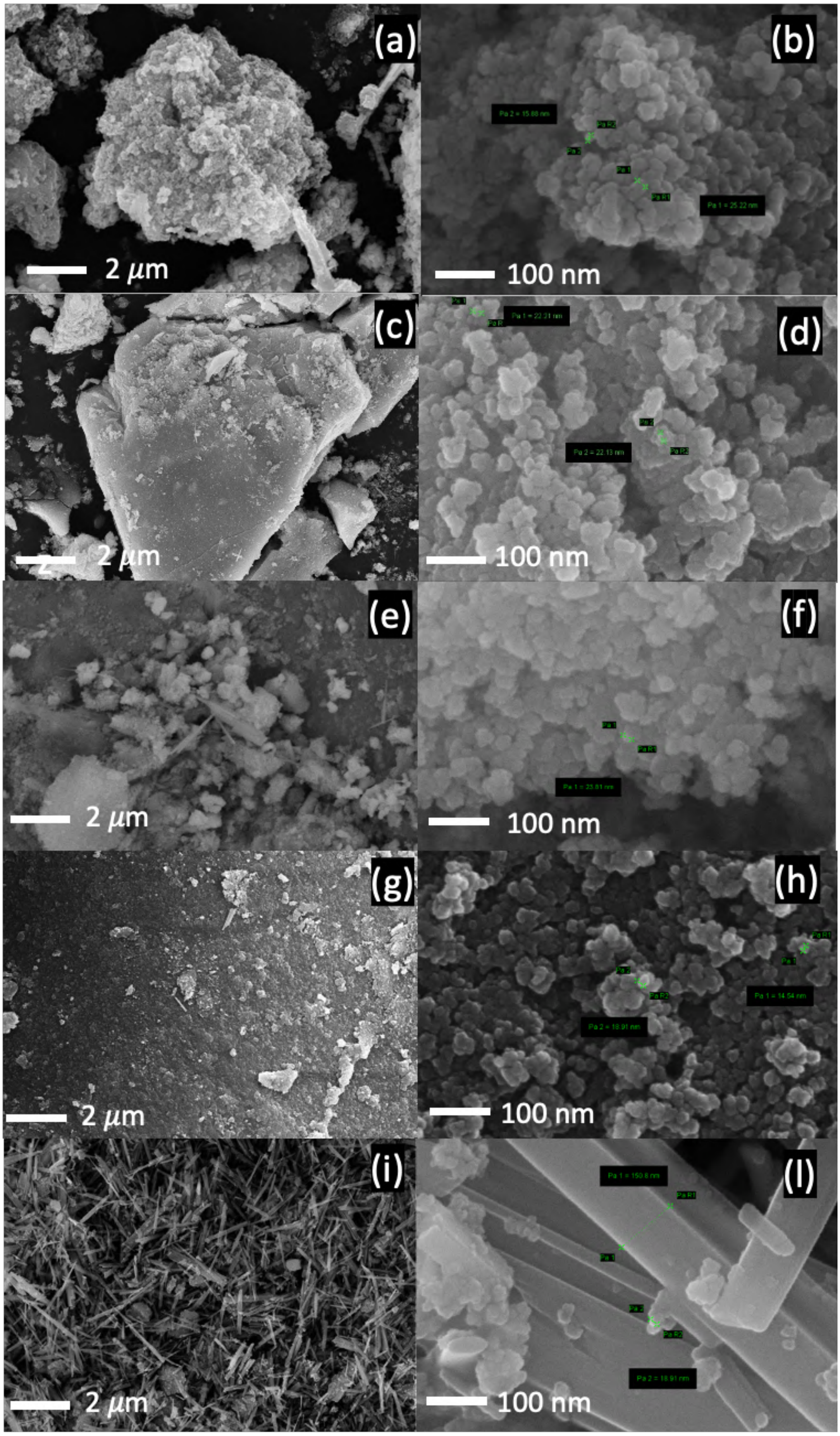

Figure 21: *SEM images of Ba-perovskites at different magnifications (Figures on the left 10 KX, Figures on the right 250 KX): (a,b) BaT, (c,d) CBaT, (e,f) NBaT, (g,h) CNBaT, (i, l) ChitBaT.*

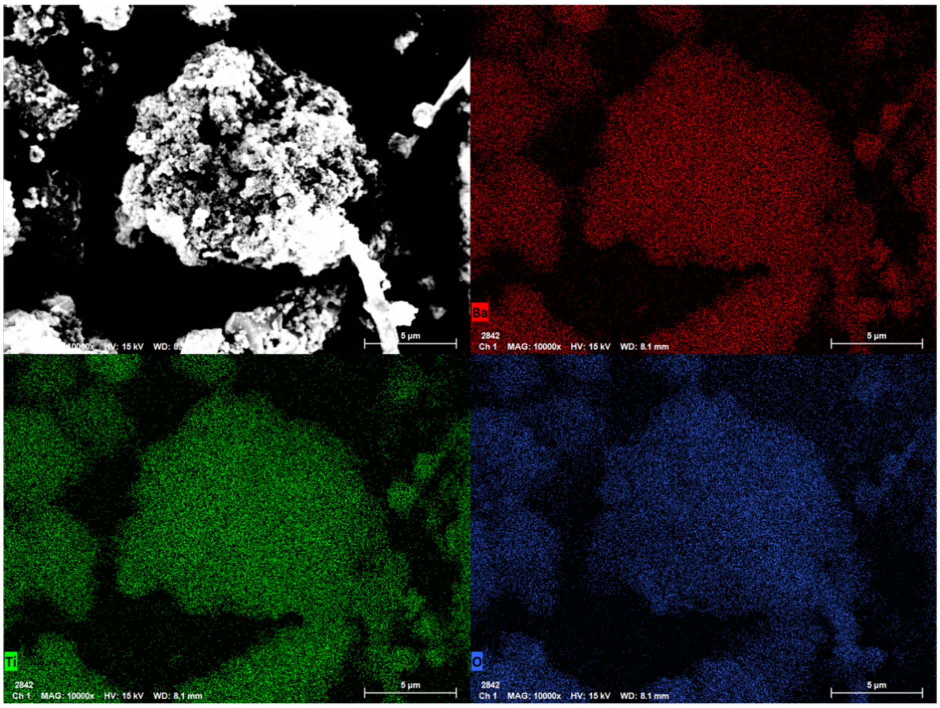

Figure 22: *SEM-EDX analysis of BaT showing the atomic distribution of barium (red), titanium (green), and oxygen (blue).*

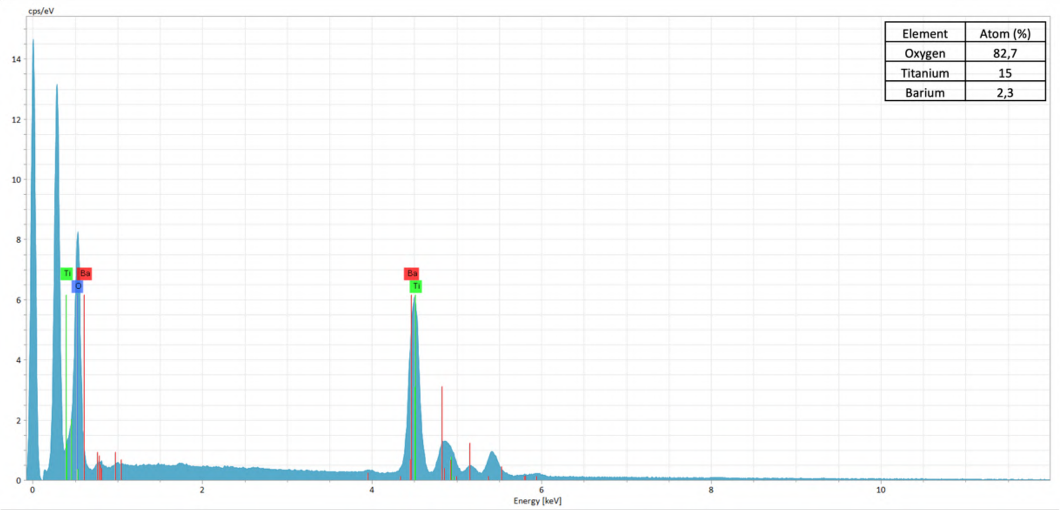

Element	Atom (%)
Oxygen	82,7
Titanium	15
Barium	2,3

Figure 23: *SEM-EDX spectra of BaT.*

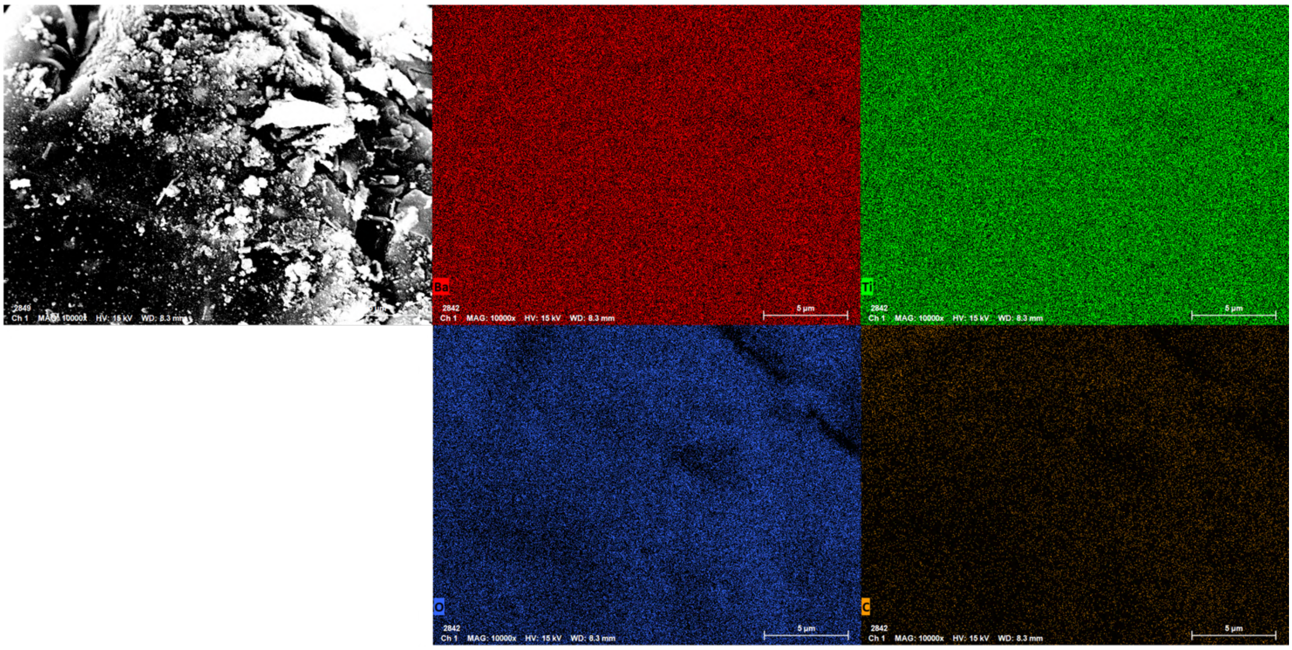

Figure 24: *SEM-EDX analysis of CBaT showing the atomic distribution of barium (red), titanium (green), oxygen (blue), carbon (brown).*

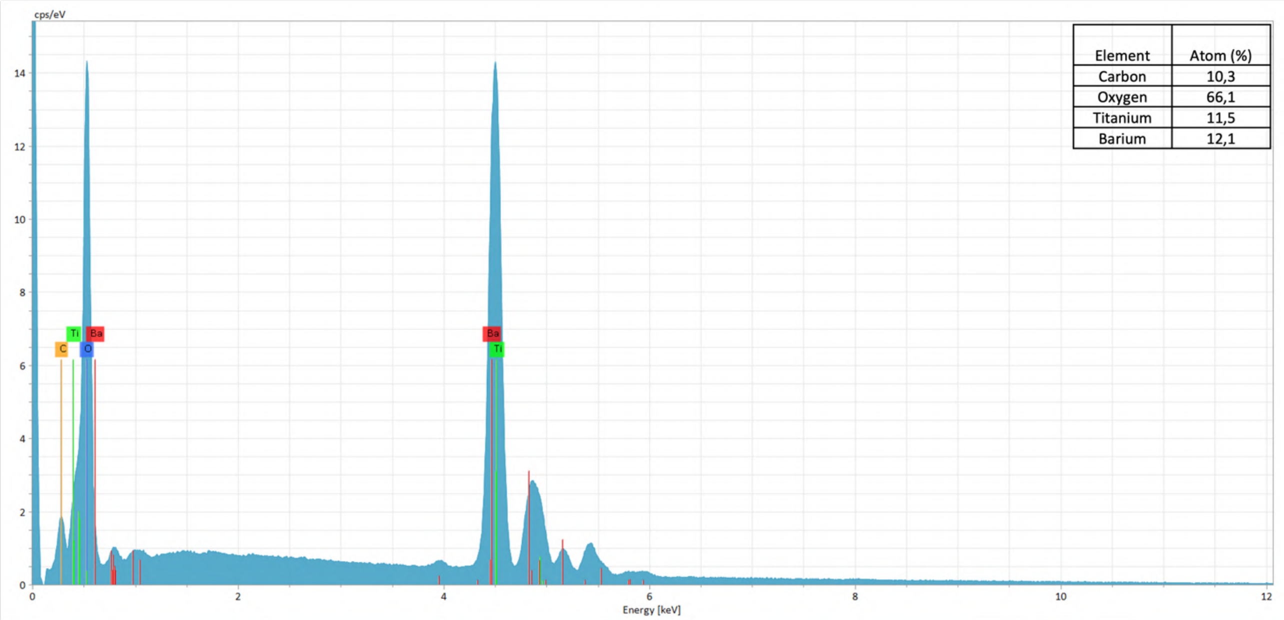

Element	Atom (%)
Carbon	10,3
Oxygen	66,1
Titanium	11,5
Barium	12,1

Figure 25: *SEM-EDX spectra of CBaT.*

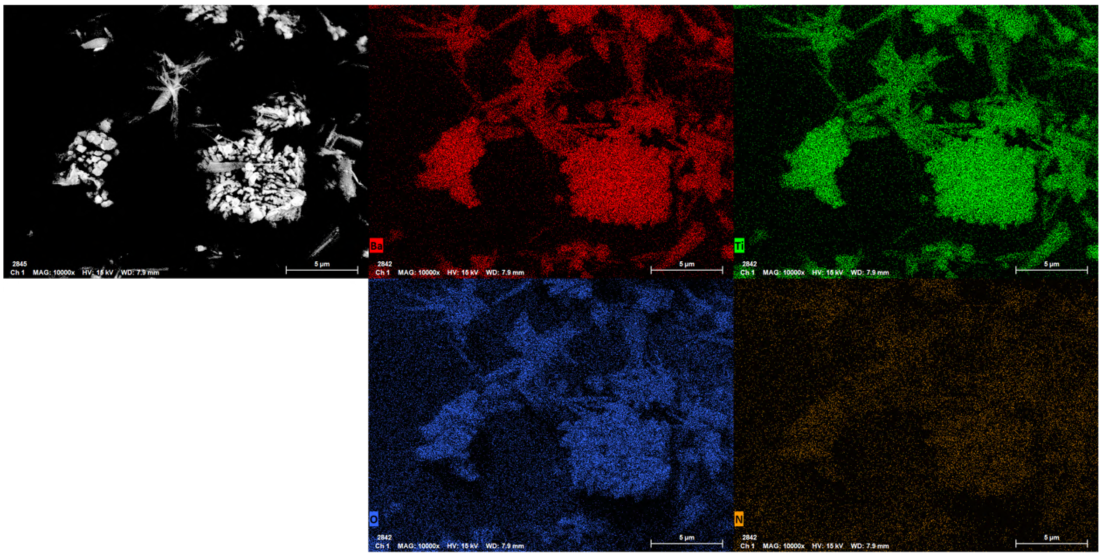

Figure 26: *SEM-EDX analysis of NBaT showing the atomic distribution of barium (red), titanium (green), nitrogen (brown), oxygen (blue).*

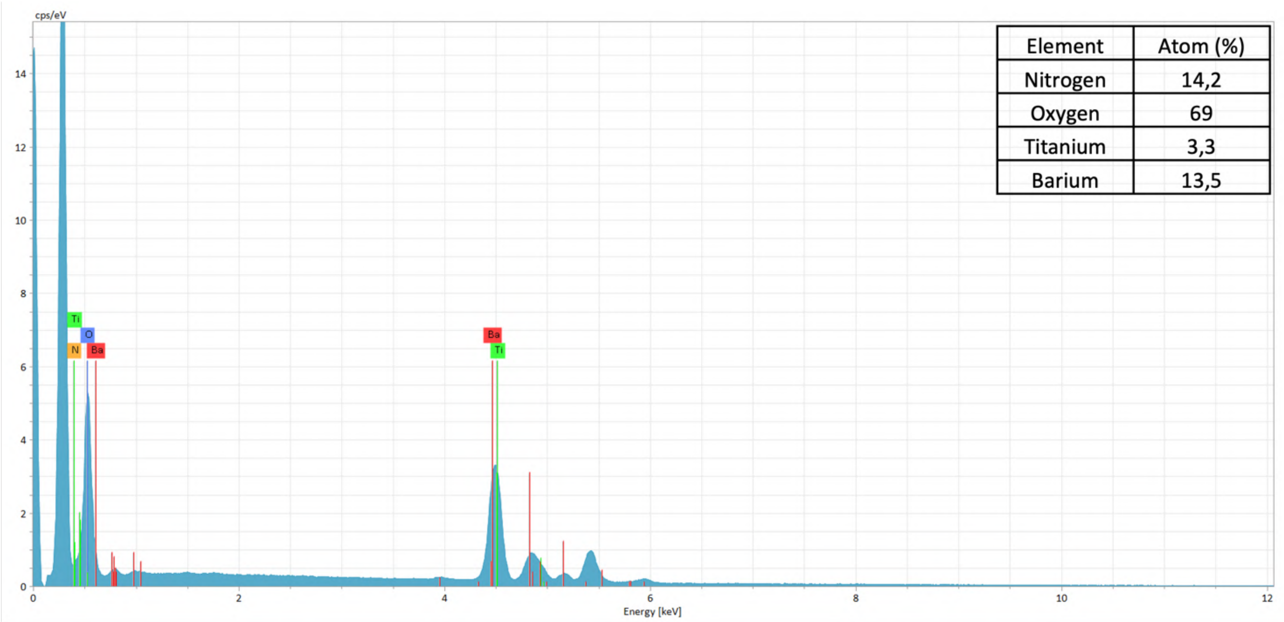

Element	Atom (%)
Nitrogen	14,2
Oxygen	69
Titanium	3,3
Barium	13,5

Figure 27: *SEM-EDX spectra of NBaT.*

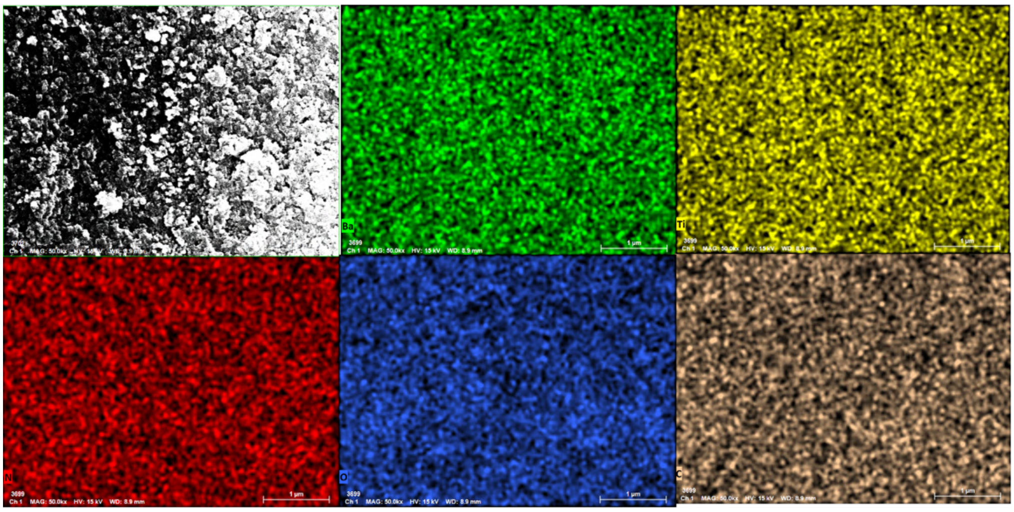

Figure 28: *SEM-EDX analysis of CNBaT showing the atomic distribution of (green) barium, (yellow) titanium, nitrogen (red), oxygen (blue), brown (carbon).*

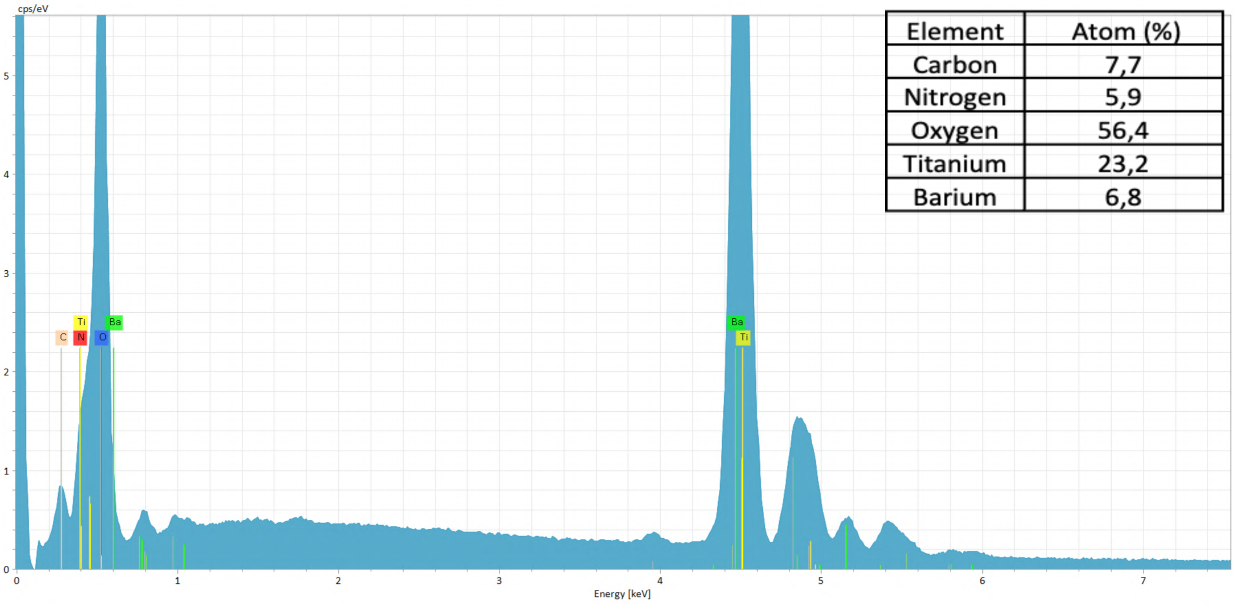

Element	Atom (%)
Carbon	7,7
Nitrogen	5,9
Oxygen	56,4
Titanium	23,2
Barium	6,8

Figure 29: *SEM-EDX spectra of CNBaT.*

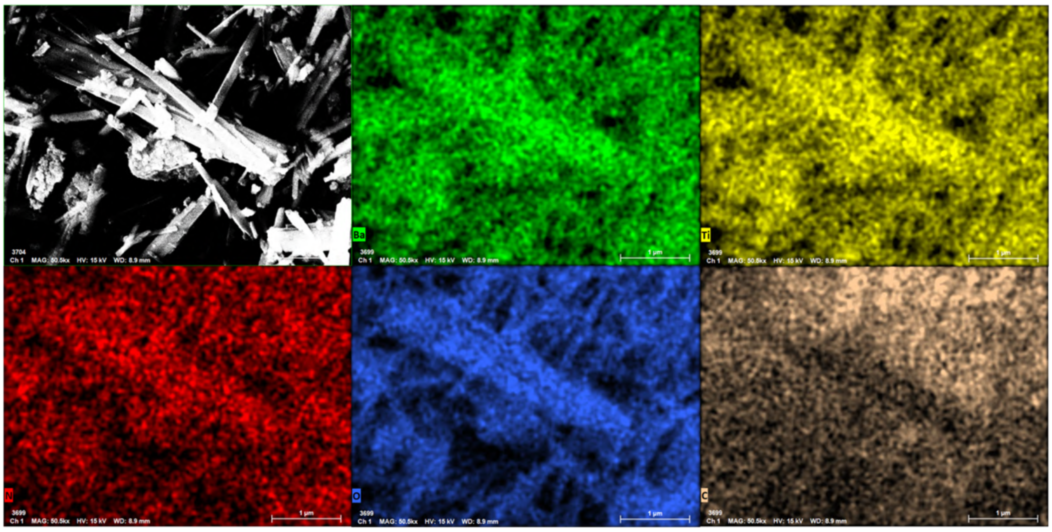

Figure 30: *SEM-EDX analysis of ChitBaT showing the atomic distribution of (green) barium, (yellow) titanium, nitrogen (red), oxygen (blue), brown (carbon).*

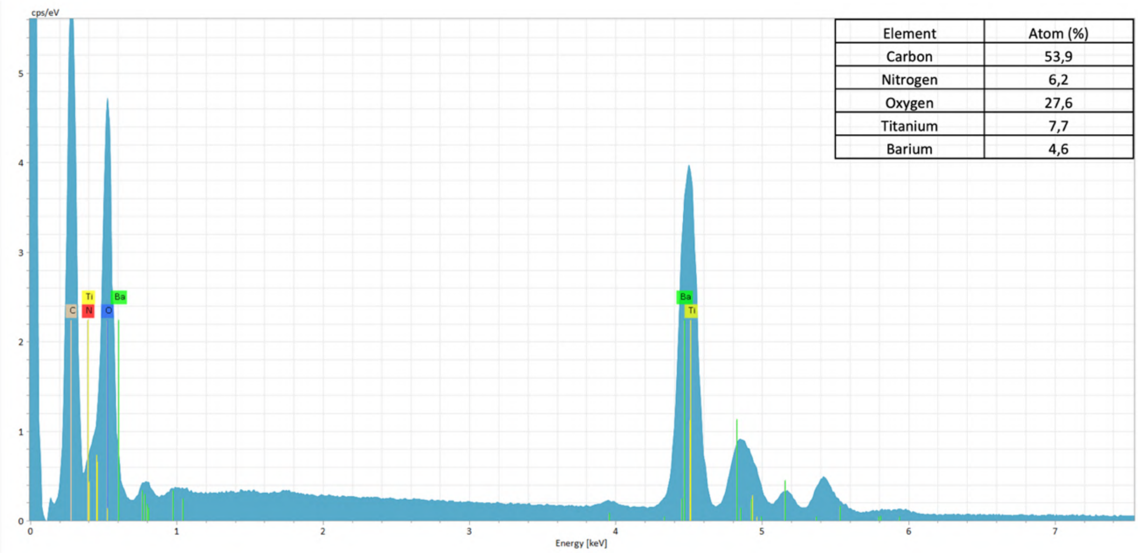

Element	Atom (%)
Carbon	53,9
Nitrogen	6,2
Oxygen	27,6
Titanium	7,7
Barium	4,6

Figure 31: *SEM-EDX spectra of ChitBaT.*

$BaTiO_3$ (figure 21 a, b) showed irregularly shaped spherical nanoparticles with average dimensions around 20 nm±8nm, together with bigger elongated structures. SEM-EDX (Figure 22) and spectrum (Figure 23) in which the atom distribution was reported, proved the formation of barium titanate structure.

CBaT (Figure 21 c, d) showed the presence of aggregates on $BaTiO_3$ surface, that could be reconducted to carbon deposition as reported in SEM-EDX analysis in Figures 24 and 25. Similarly, the particles average dimensions were around 22±0,06nm. In Figure 25, the revealed carbon percentage was in accordance to the expected ratios of Ba:Ti:C equal to 1:1:1.

NBaT (Figure 21 e, f) showed a structure composed by nanoparticles with average dimensions around 24±0,01 nm, along with the presence of elongated structures as for $BaTiO_3$. EDX mapping (Figure 26) reported that these elongated structures were made of perovskite material.

CNBaT (Figure 21 g, h) reported the presence of aggregated spherical particles, whose average dimensions were 17±3 nm. Figure 31 showed the atomic distribution of Ba, Ti, O, N, and C in CNBaT. All the elements were presented in the sample even if with different atomic ratios than that predicted (Ba:Ti 1:1) with atomic percentages resulted to be 56%, 23%, 6,8% for respectively O, Ti and Ba, which composed the perovskite structure. The presence of C and N atoms was confirmed.

However, compared to the other Ba-perovskites, chitosan-doped $BaTiO_3$ (Figure 21 i, l) demonstrated a different morphology characterized by a fibrous structure. The latter was composed of fibers with dimensions of 151 nm, on which were deposited spherical particles of 19 nm. SEM-EDX image and spectra (Figures 30, 31) of this sample reported the presence of a high content of carbon (53,9%) and 6,2% of nitrogen, which corresponded to atomic ratios equal to 4:1, reconducted to the insertion of chitosan.

The hydrothermal synthesis conditions, in particular time, temperature and pH affected the physical properties of the product samples. The reaction duration was shorter for bare $BaTiO_3$ compared to the one of the doped samples. Thus, with an increase in the reaction time the particles sizes increased. This was because in the initial stage of the reaction, hydroxide ions of barium formed smaller nuclei which grew over the time[65]. This was demonstrated in the particle's average dimensions ranging from 20 nm for bare $BaTiO_3$ to 22-24 nm for single doped samples.

Beside the temperature, which was reported to accelerate the N doping of semiconductors[71], the pH likely influenced the particles morphology, leading to a greater size irregularity in the case of N-$BaTiO_3$, being synthesized at lower pH.

The high-resolution images of the calcium perovskites are reported in Figure 32. SEM-EDX images and spectra are shown from Figure 33 to Figure 40.

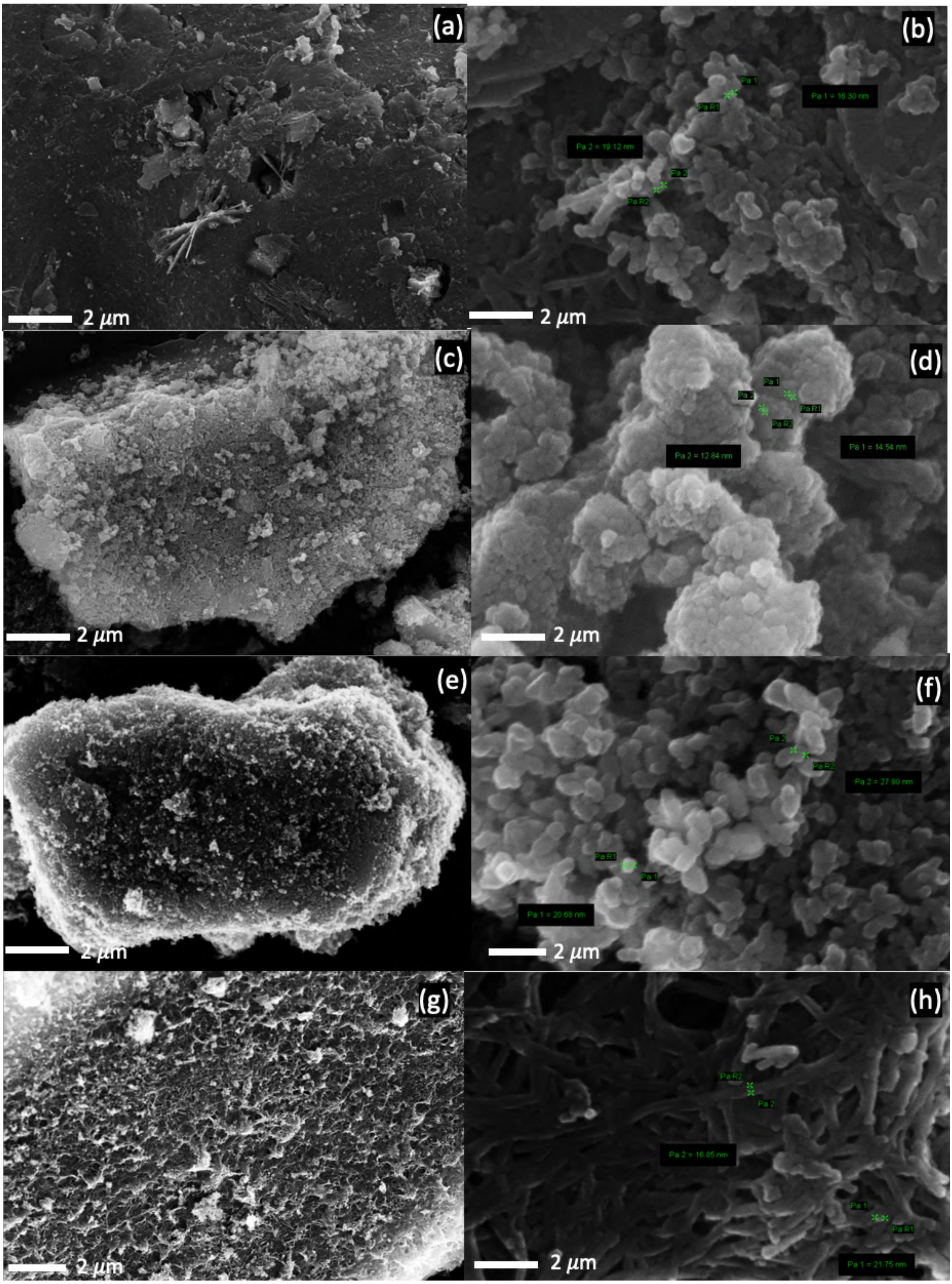

Figure 32: *SEM images of Ca-perovskites at different magnifications (Figures on the left 10 KX, Figures on the right 250 KX): (a,b) CaT, (c,d) CCaT, (e, f) NCaT, (g, h) CNCaT.*

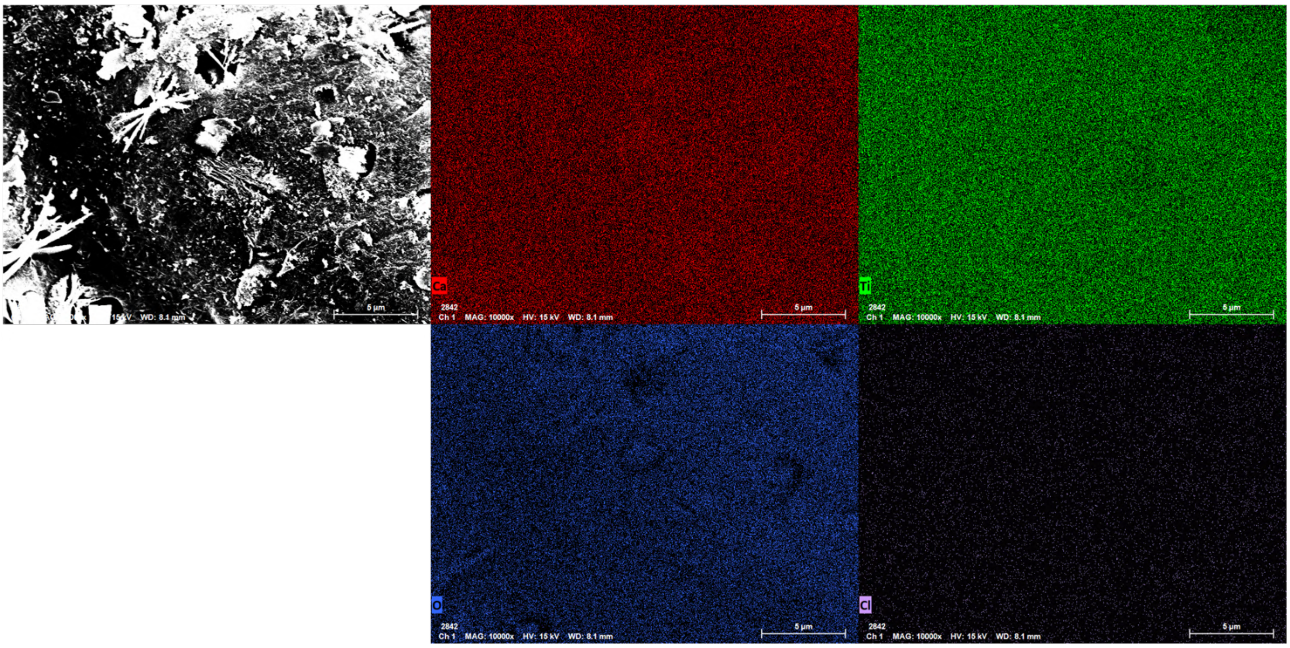

Figure 33: *SEM-EDX analysis of CaT showing the atomic distribution of calcium (red), titanium (green), oxygen (blue) and chlorine (purple).*

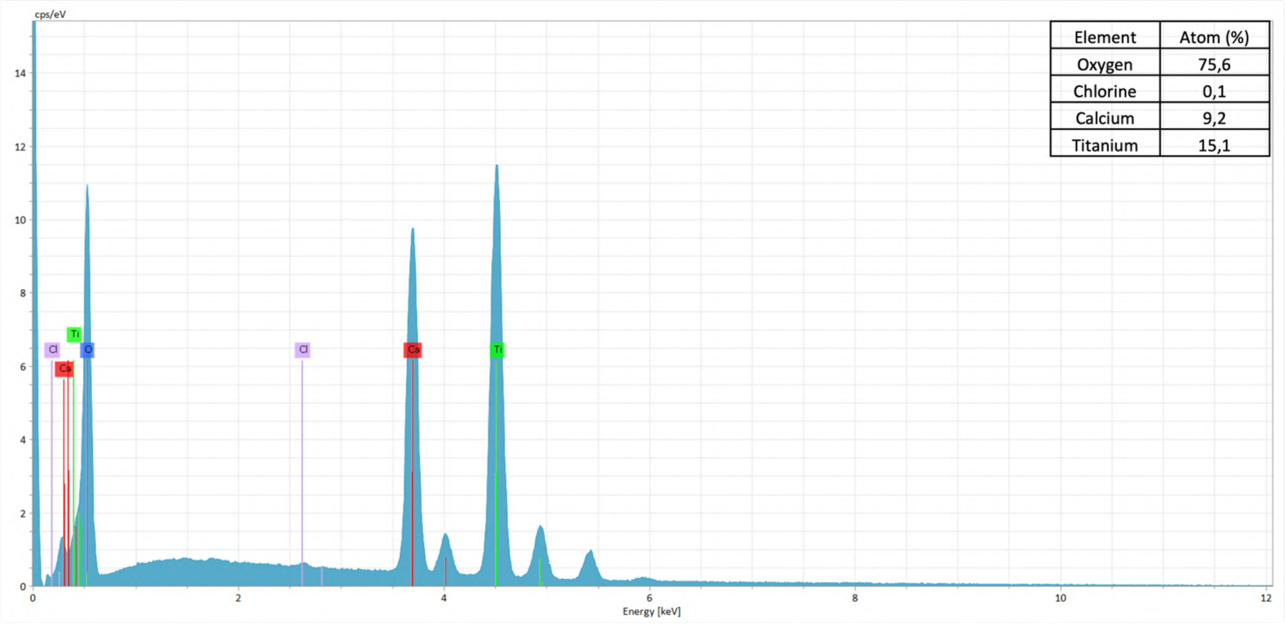

Element	Atom (%)
Oxygen	75,6
Chlorine	0,1
Calcium	9,2
Titanium	15,1

Figure 34: *SEM-EDX spectra of CaT.*

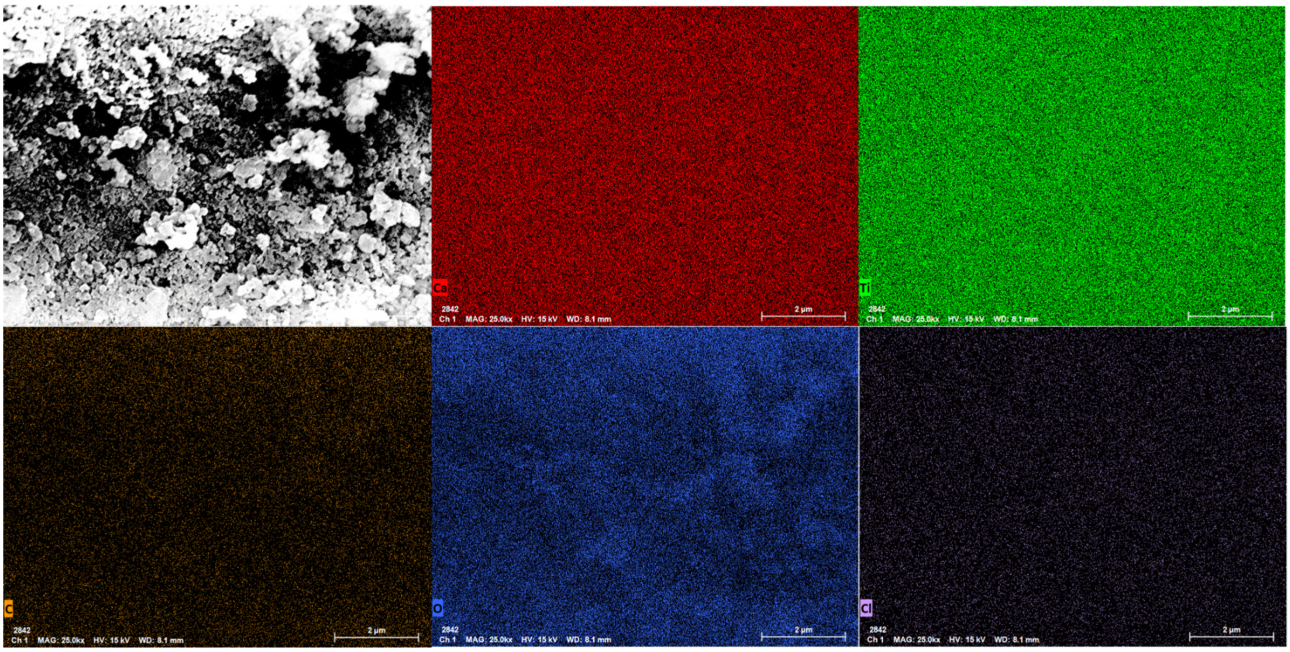

Figure 35: *SEM-EDX analysis of CCaT showing the atomic distribution of calcium (red), titanium (green), carbon (brown), oxygen (blue), chlorine (purple).*

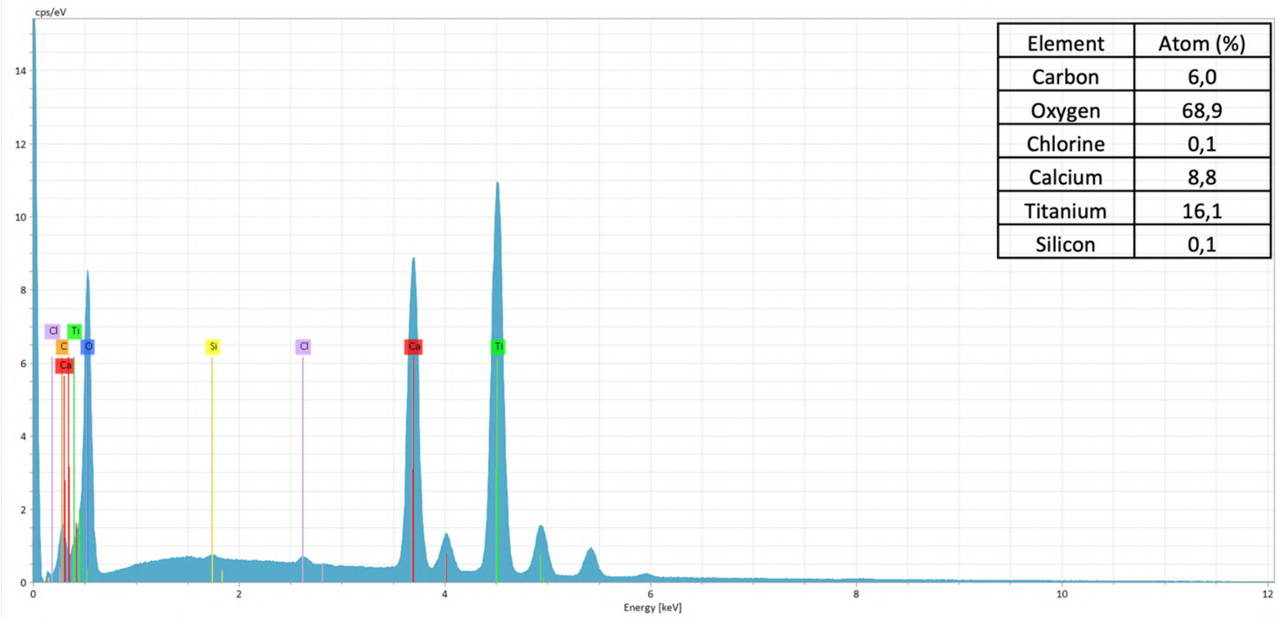

Element	Atom (%)
Carbon	6,0
Oxygen	68,9
Chlorine	0,1
Calcium	8,8
Titanium	16,1
Silicon	0,1

Figure 36: *SEM-EDX spectra of CCat.*

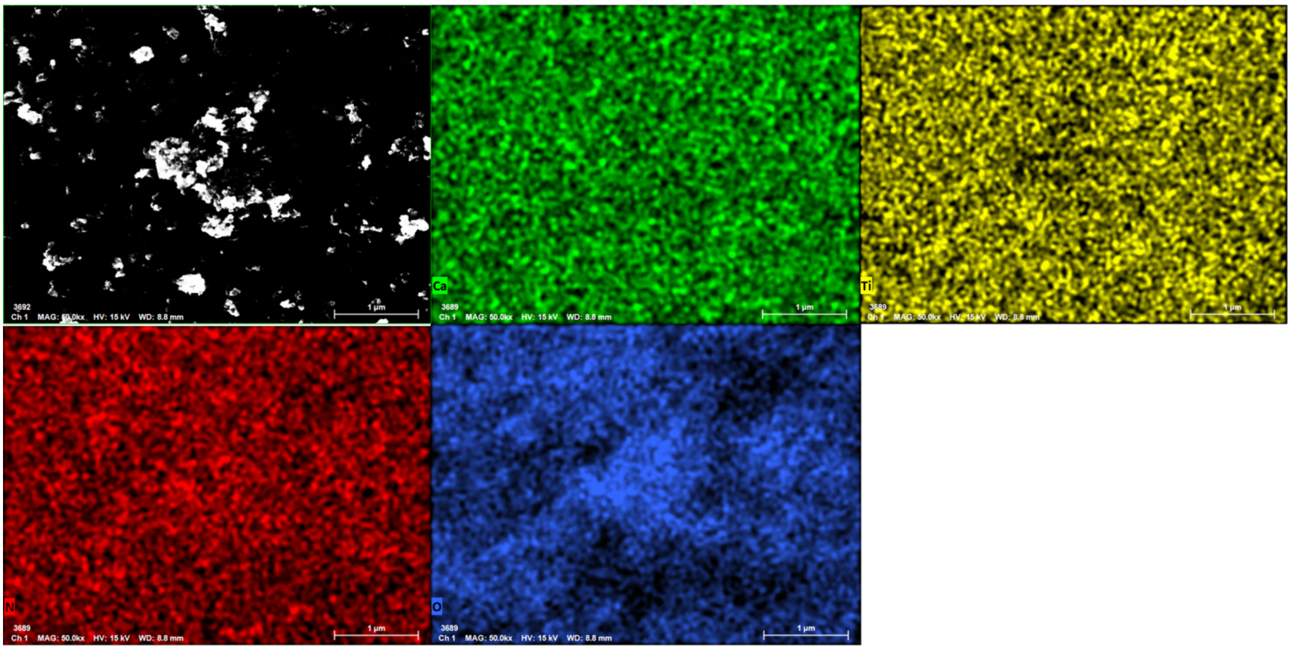

Figure 37: *SEM-EDX analysis of NCaT showing the atomic distribution of calcium (green), titanium (yellow), nitrogen (red), oxygen (blue).*

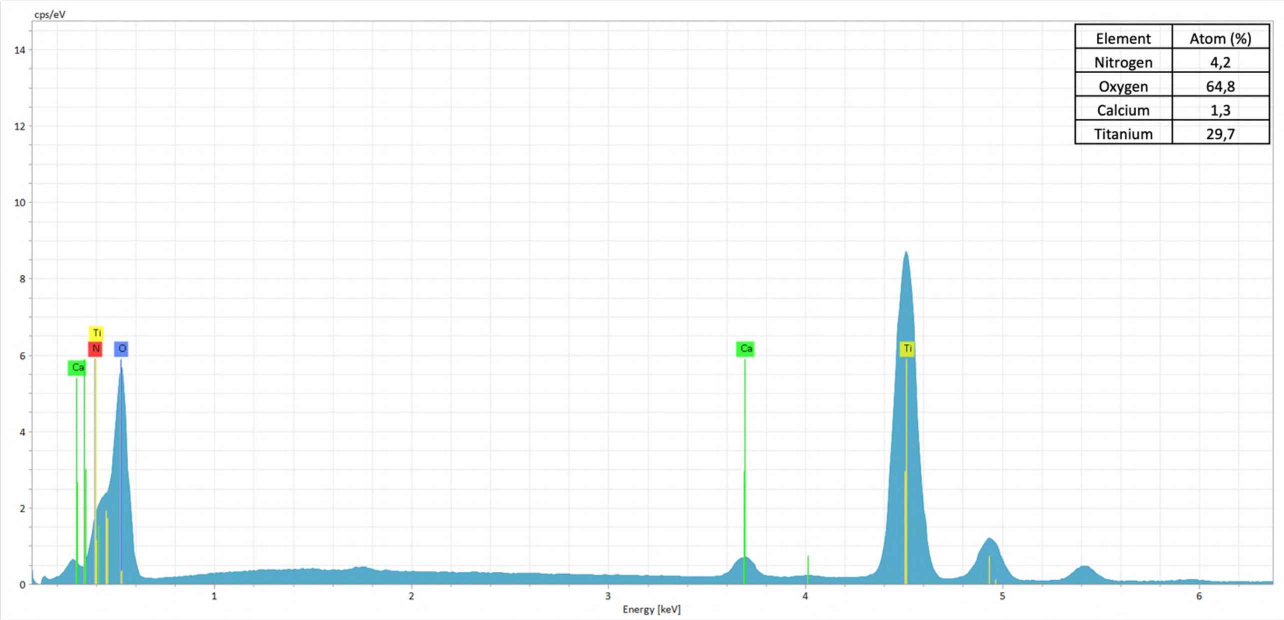

Element	Atom (%)
Nitrogen	4,2
Oxygen	64,8
Calcium	1,3
Titanium	29,7

Figure 38: *SEM-EDX spectra of NCat.*

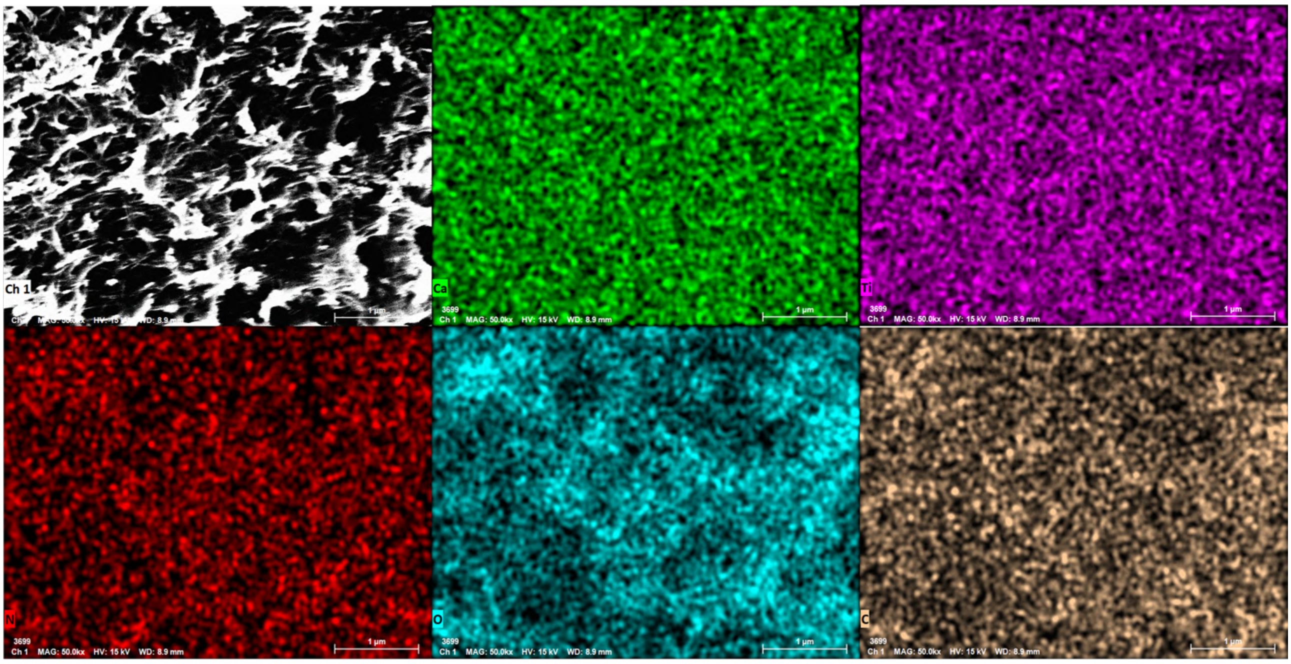

Figure 39: *SEM-EDX analysis of CNCaT showing the atomic distribution of calcium (green), titanium (purple), nitrogen (red), oxygen (blue), and carbon (brown).*

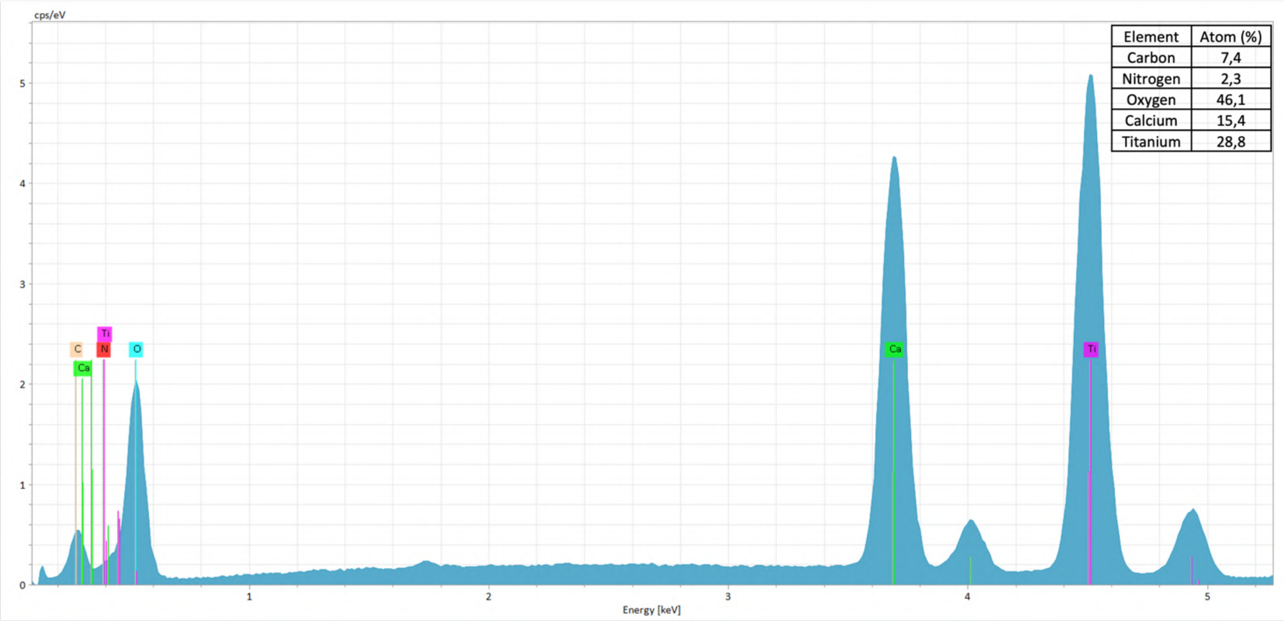

Element	Atom (%)
Carbon	7,4
Nitrogen	2,3
Oxygen	46,1
Calcium	15,4
Titanium	28,8

Figure 40: *SEM-EDX spectra of CNCat.*

$CaTiO_3$ (Figure 32 a, b) morphology was quite different from $BaTiO_3$, even if it was characterized by aggregated microstructures composed by spherical particles. In fact, it presented particles average dimensions around 18±2 nm. Similarly, structures with elongated morphology were observed. EDX mapping (Figures 33-34) confirmed the perovskite formation, and traces of chlorine were detected, which could be derived from calcium chloride used as reagent. Chloride was usually removed in the washing step with water and ethanol after the synthesis. CCaT (Figure 32 c, d) images demonstrated the formation of spherical particles with average dimensions of about 14±1 nm. In the work of *Badovinac et al.* it was reported that due to the increase of the active surface area, these nanoparticles or smaller grains can play an important role in the catalytic efficiency[72]. It was noted that the average dimensions of CCaT were smaller and morphologically more irregular and jagged than that of bare $CaTiO_3$. As reported in Figure 36, carbon distribution was in accordance to the predicted ratios (1Ca:1Ti:1C). In addition, traces of silicon and chlorine were detected and reconducted to the crystallizer and to some impurities presented in the synthetic step. NCaT SEM image (Figure 32 e, f) demonstrated a similar structure to CCaT, even if the particles morphology was bigger in NCaT sample. In fact, the average particles dimensions were around 24±5 nm. SEM-EDX (Figures 37, 38) showed the effective presence of nitrogen as doping atom (4,2%), whereas the predicted atomic ratios of 1Ca:1Ti:1N was not respected. CNCaT (Figure 32 g, h) showed a quite different structure than the other single-doped samples, with particles average dimensions of 19±3 nm. This morphology was characterized by the presence of both nitrogen and carbon, with the predicted atomic ratios, as confirmed by SEM-EDX analysis reported in Figures 39 and 40.

TEM images of calcium perovskites are shown in Figure 41.

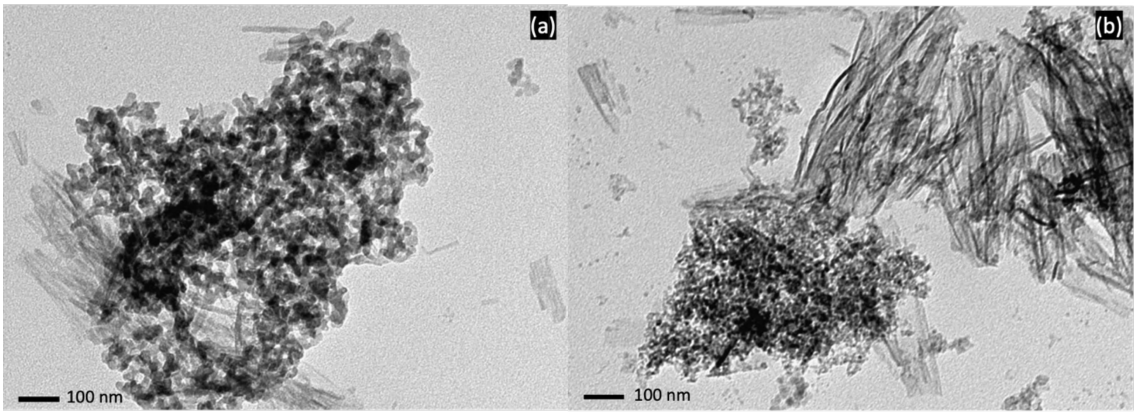

Figure 41: *TEM images of Ca- perovskites: (a) CaT, (b) CCaT.*

TEM images of $CaTiO_3$ and of C-$CaTiO_3$ showed the presence of elongated structures. In addition, visibly the C-$CaTiO_3$ particles were smaller than that of bare $CaTiO_3$, as previous reported in the SEM analysis.

These observations supported the prevalence of amorphous phases compared to crystalline structures.

Elemental analysis was perfomed to further assess the presence of nitrogen and carbon in the doped perovskites. The results of Ba-perovskites are reported in Table 4.

Table 4: *Nitrogen and Carbon composition of Ba-perovskites.*

Sample	N (%)	C (%)
BaT	0,00	0,00
CBaT	0,01	2,45
NBaT	0,00	0,00
CNBaT	0,06	1,42
ChitBaT	0,61	4,05

As reported in Table 4, as expected BaT did not present neither nitrogen nor carbon. An unexpected result was obtained for NBaT sample in which the doping element nitrogen was not detected. This was not in accordance with EDX mapping (Figure 26), which detected the presence of nitrogen. For this reason, EDX analysis will be repeated or more insights will be carried out.

In addition, NBaT had similar chemical composition to bare BaT. This fact could explain the similar XRD spectra to the bare perovskite (Figure 19). The analysis suggested that doping did not occur.

CBaT showed the presence of 2,45% of carbon, demonstrating the doping efficiency with this element. This is in accordance with SEM-EDX analysis (Figures 24-25) and with the XRD spectrum (Figure 19) in which it was underlined the amorphous and distorted structure of CBaT due to the carbon doping. In the co-doped CNBaT, the presence of carbon (1,42%) confirmed its doping, whereas nitrogen percentage was low (0,06%). Also in the study of *Olivo et al.* in the co-doped catalysts nitrogen was almost negligible, probably due to the procedure of carbon introduction[30]. Probably nitrogen had not inserted well in the structure as carbon did. This was supported by the similar XRD profile of CNBaT to CBaT. However, ChitBaT showed the presence of both nitrogen and carbon, so the chitosan insertion did effectively happen, as supported by SEM analysis.

The results obtained for Ca-perovskites by elemental analysis are shown in Table 5.

Table 5: *Nitrogen and Carbon composition of Ca-perovskites.*

Sample	N (%)	C (%)
CaT	0,01	0,00
CCaT	0,01	4,29
NCaT	0,05	0,98
CNCaT	0,07	2,70

CaT sample was not composed by neither nitrogen nor carbon. The nitrogen percentage of 0,01% was attributed to the adsorption of air during the preparation of the sample. The doping Ca-perovskites showed the presence of the doping elements, confirming their insertion in the structure, in line with the XRD spectra (Figure 20). However, NCaT presented traces of carbon (0,98%) probably related to some impurities in the autoclave during the synthesis.

N_2 physisorption analysis was performed to determine the surface area, porosity, and ability of adsorption/desorption of each perovskite. The adsorption desorption isotherms of BaT and NBaT, CBaT, CNBaT are reported in Figure 42. Superficial area and pore volume values are reported in Table 1.

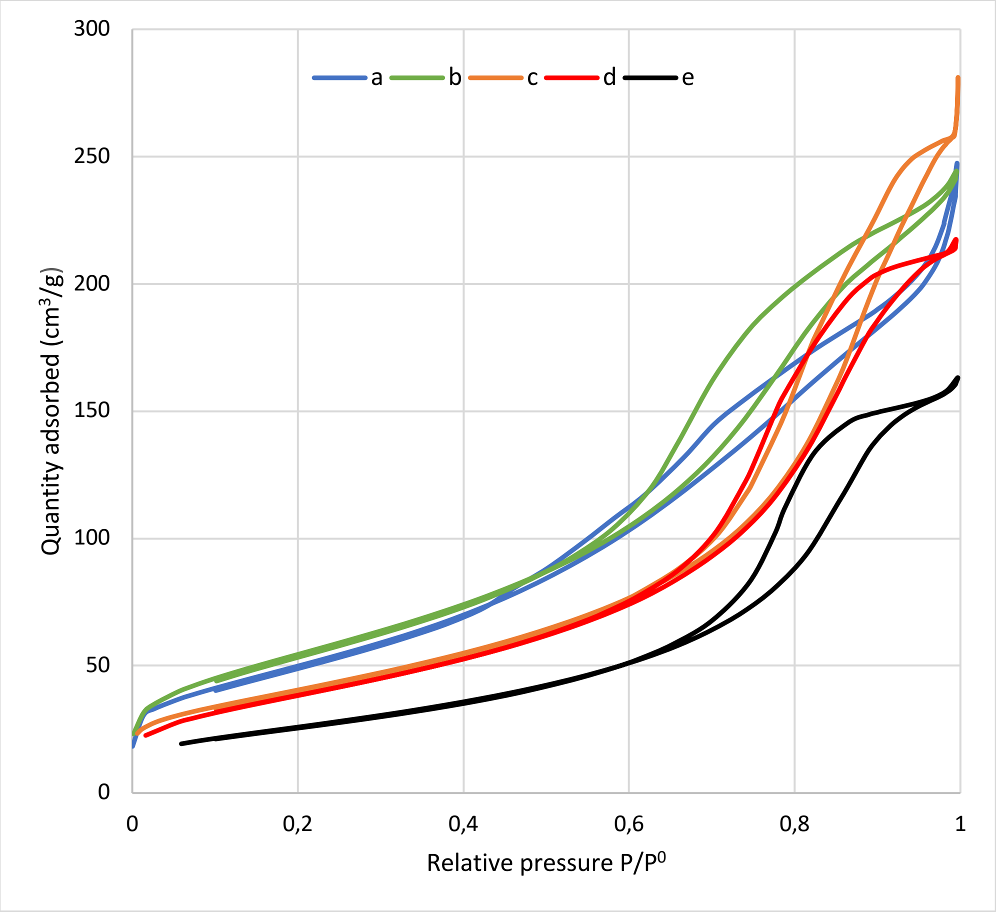

Figure 42: *Nitrogen adsorption/desorption isotherms of (a) BaT, (b) CBaT, (c) NBaT, (d) CNBaT, (e) ChitBaT.*

Table 6: *Surface area and pore volume values of $BaTiO_3$ and N, C, NC doped $BaTiO_3$*

Sample	**BET surface area (m^2/g)**	**Pore volume (cm^3/g)**
BaT	181	0,04
CBaT	196	0,34
NBaT	145	0,38
CNBat	140	0,32
ChitBaT	96	0,23

In general, barium-based perovskites showed type IV isotherms. In particular, BaT and CBaT (Figure 42 a, b) presented unclosed type H1 hysteresis loop, that could be lead back to a greater variability of pores, including macropores and mesopores[73]. In addition, these two perovskites showed a surface area of 181 m^2/g and 196 m^2/g, respectively, which were slightly higher than the other samples. In the work of *Dolat et al.* it was reported that as the carbon content on the surface increased, the charge of the surface decreased leading to less particle agglomeration, thus resulting into larger surface areas[74]. Despite the higher surface area, BaT was characterized by a critical reduction of the pore volume (Table 6).

On the other hand, doping the perovskite with nitrogen or both nitrogen and carbon (Figure 42 c, d, e) lead to type IV isotherms, relative to mesoporous systems, according to IUPAC classification[55],[64]. However, all other samples presented a lower surface area than bare BaT. For Chit-BaT, the result was likely attributed to the possible chitosan, which had high molecular weight – or byproducts – accumulation inside the pores of BaT, reducing the gas interaction at the surface of the perovskite. In addition, as the other doped materials, NBaT and CNBaT samples were left aging for 20 hours, and as reported in the SEM analysis discussion, the reaction time led to different particle sizes. In fact, in these cases, a higher average dimension of the particles led to lower surface area values. However, except for ChitBaT, the samples porosity did not change considerably. In particular, higher amounts of gas were absorbed by the single doped perovskites.

The adsorption desorption isotherms of $CaTiO_3$ and N, C, CN doped are reported in Figure 43.

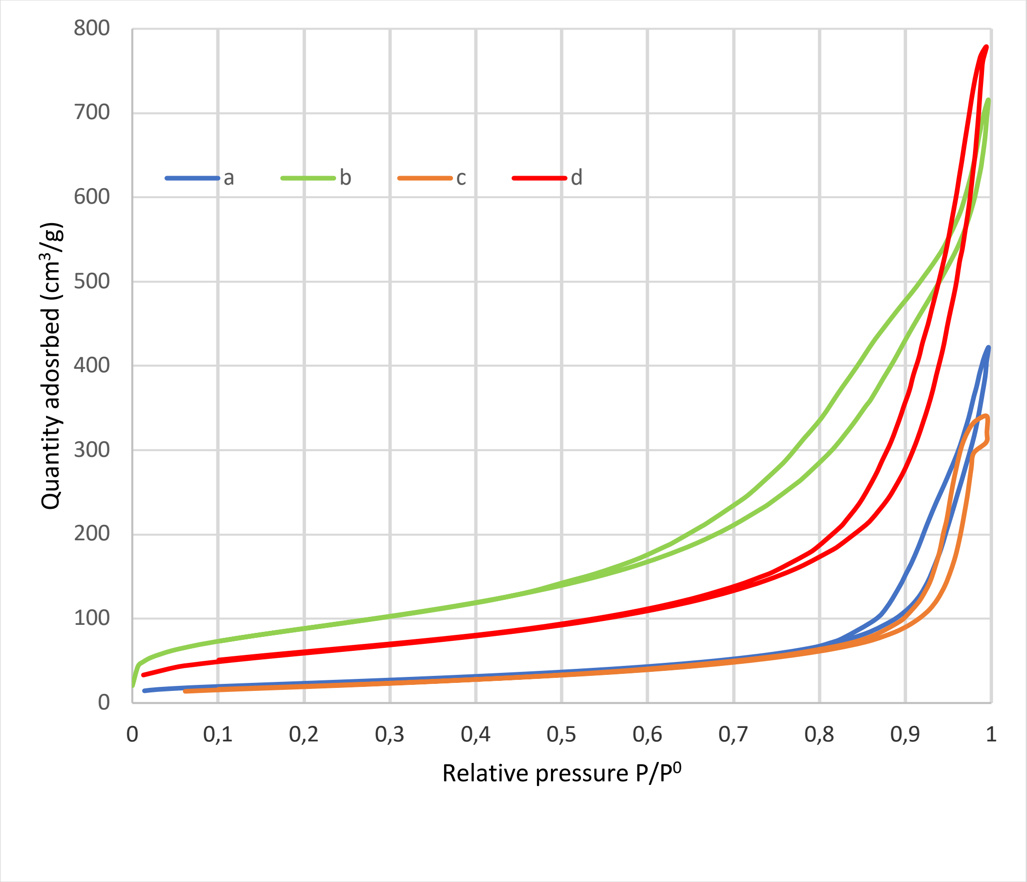

Figure 43: *Adsorption/desorption isotherms of Ca-based perovskites: (a) CaT, (b) CCaT, (c) NCaT, (d) CNCaT.*

Table 7: *Surface area and pore volume values of $CaTiO_3$ and N, C, NC doped $CaTiO_3$.*

Sample	**BET surface area (m^2/g)**	**Pore volume (cm^3/g)**
CaT	84	0,23
CCaT	313	0,07
NCaT	74	0,15
CNCaT	215	0,55

As it is reported in the graph 43, comparing to the corresponding barium-based perovskites, the calcium-based one presented type IV isotherms with a type H1 hysteresis loop associated with the filling and emptying of mesopores by capillary condensation, and the presence of macropores in higher relative pressure, suggesting the presence of both mesopores and macropores and resulting

in multi-porous systems. CCaT and CNCaT (Figure 43 b, d) adsorbed more gas than the other samples. This was confirmed by BET surface area values reported in Table 7.
BET surface area values of 313 m^2/g and 215 m^2/g for CCaT and CNCaT respectively were higher than those of the other samples. This could be referred to the same reasons proposed by *Dolat et al.*[74]. Comparing to $BaTiO_3$, $CaTiO_3$ had an overall lower surface area, except for CCaT and CNCaT which had larger areas than all barium-based samples. However, NCaT BET surface area value of 74 m^2/g was lower than the others. This was also obtained by *Asahi et al.* who performed a heating treatment of titania with ammonia and observed a consequent decrease of the specific surface area[75]. *Alammar et al.* studied N-doped $SrTiO_3$ and observed a surface area decrease than that of the undoped perovskite, and they supposed it to be related to a partial collapse of the mesopores during the synthesis[64].

Then the doping effect on surface area values was compared between Ba-perovskites and Ca ones. It was shown that doping the perovskites with carbon led to higher surface areas in both Ba and Ca samples, as explained by *Dolat et al*.[74]. However, nitrogen-doping led to higher areas for NBaT (145 m^2/g) than that of NCaT (74 m^2/g) even if the average particles dimensions were similar (Figures 21 e, f and 32 e, f). This result was probably related to the fact that in the case of NBaT, as demonstrated by the previous characterizations, the pores volume was bigger than that of NCaT (0,38 cm^3/g for NBaT, 0,15 cm^3/g for NCaT). The porosity affected the interaction with physisorbed nitrogen and therefore the surface area. The co-doping effect led to 215 m^2/g for CNCaT compared to 140 m^2/g for CNBaT. These structures were morphologically different: CNBaT was composed by spherical particles and the pores volume corresponded to 0,32 cm^3/g, whereas CNCaT morphology seemed to be more interconnected and porous, presenting pores volume of 0,55 cm^3/g. So, the greater porosity could explain the higher surface area value.

4.1.2 OPTICAL AND SPECTROSCOPIC CHARACTERIZATIONS.

DRS was applied to determine perovskites interaction with light. UV-Vis spectra of barium-based perovskites are reported in Figure 44 as Kubelka-Munk functions. The energy band gap values were extrapolated from Tauc plot and reported in Figure 45.

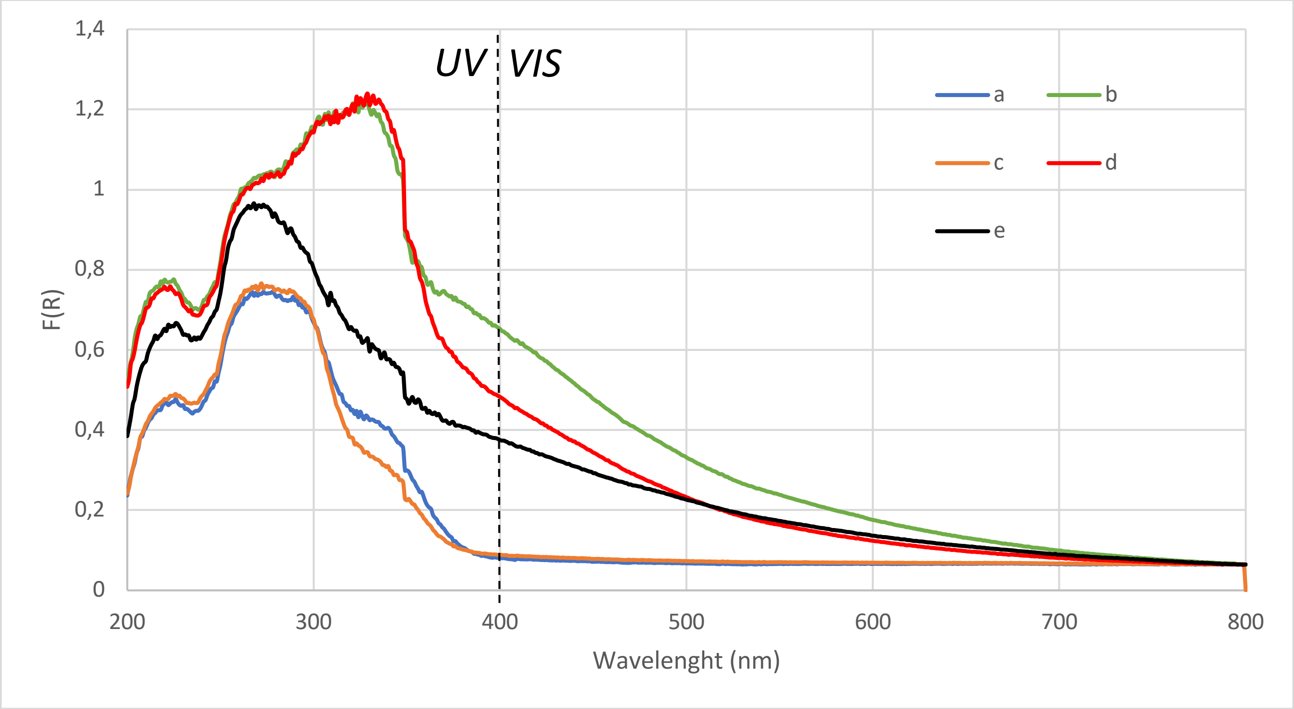

Figure 44*: DRS spectra of Ba-based perovskites reported as Kubelka-Munk functions: (a) BaT, (b) CBaT, (c) NBaT, (d) CNBaT, (e) ChitBaT.*

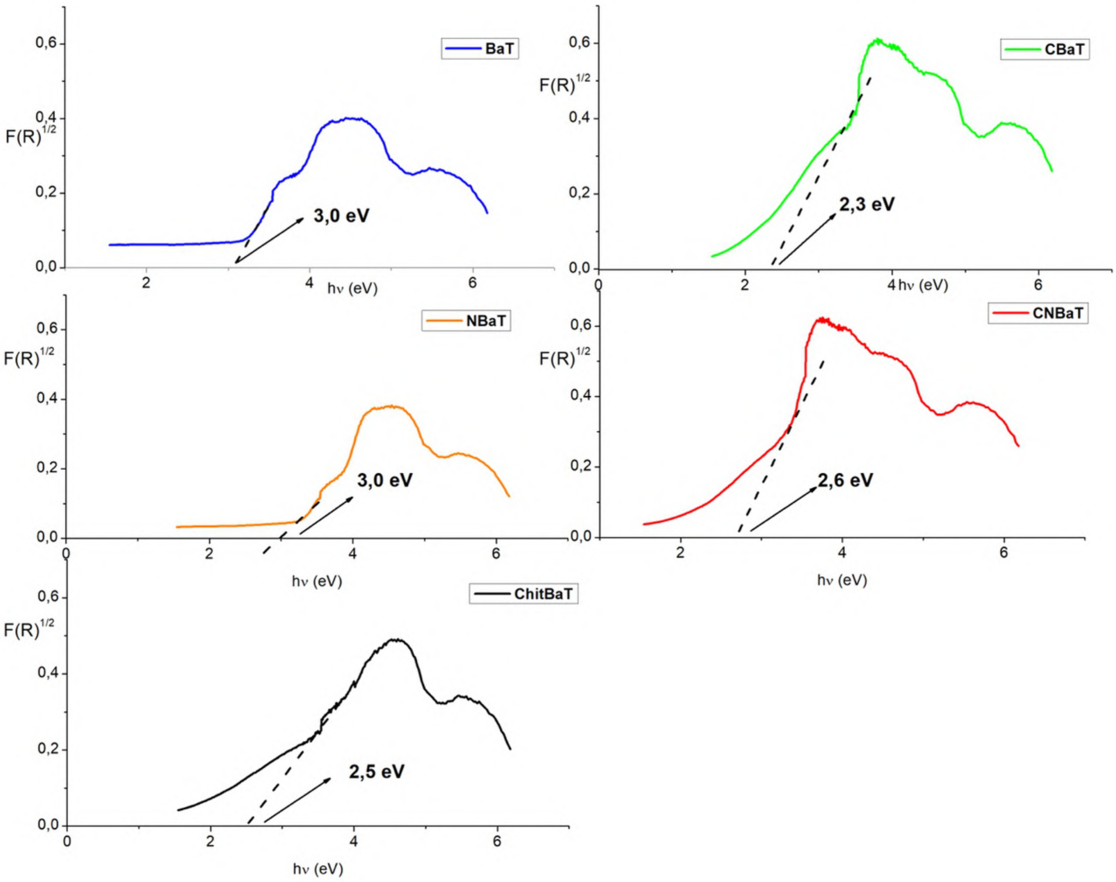

Figure 45: *Tauc plots and energy band gap values of BaT (blue), CBaT (green), NBaT (orange), CNBaT (red), and ChitBaT (black).*

Graph 44 showed that all materials absorbed in the UV region but only C-$BaTiO_3$, CN-$BaTiO_3$ and Chitosan-$BaTiO_3$ were active in the visible region of the spectra (in the range 400-600 nm). Graph 45 related the absorption coefficient α to hν using the following Equation 7.

$$(\alpha h\nu)^{1/2} = C(h\nu - E_g)\ \textbf{Equation 7}$$

where C is a constant and E_g is the band gap. The function of reflectance F(R) is directly proportional to $(\alpha h\nu)$. The band gap was given by extrapolating the intercept of the tangent on the x-axis. Tauc plots showed that $BaTiO_3$ had the biggest band gap that was approximately 3 eV, whereas 3,0 eV, 2,3 eV, 2,6 eV and 2,5 eV respectively for N, C, CN, and chitosan $BaTiO_3$. As expected, doping the material with heteroatoms, in particular with carbon, likely led to the narrowing of the band gap (Figure 45). It is possible that carbon replaced some oxygen atoms or gained interstitial positions, generating intra-gap energy layers and lattice distortions, by shifting the perovskite adsorption in the visible region[30]. *Teng et al.* studied the density of states of the orbitals for carbon doped $BaTiO_3$ and suggested that the C 2p states of the dopant are distributed at the two sides of the Fermi level, thereby resulting in a band gap narrowing effect[76]. On the other hand, the DRS spectra (Figure 44 c) showed that NBaT had a similar trend to BaT, as well as similar band gaps. Therefore, doping with nitrogen did not lead to a discrete narrowing of the band gap, suggesting that the introduction of N into the lattice did not occur, as supported by the elemental analysis.

UV-Vis spectra of calcium-based perovskites are reported in Figure 46 as Kubelka-Munk functions. Tauc plots of Calcium-based materials are reported in Figure 47.

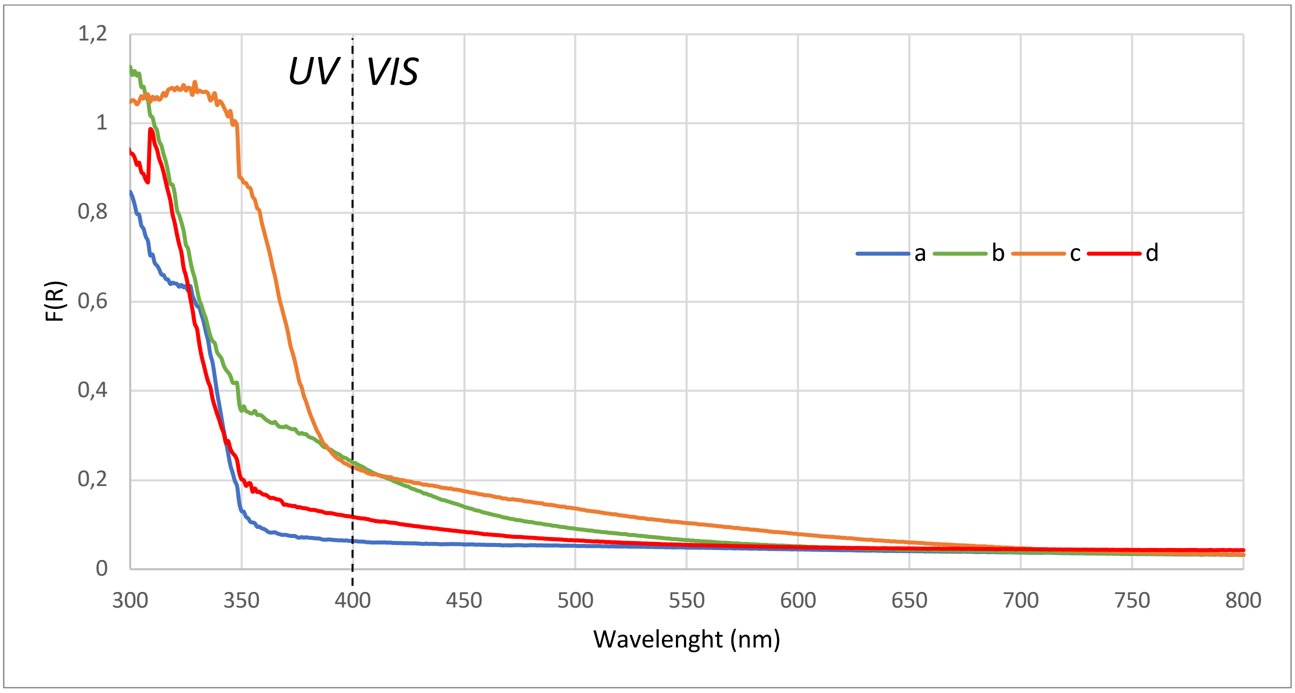

Figure 46: *DRS spectra of Ca-based perovskites reported as Kubelka-Munk functions: (a) CaT, (b) CCaT, (c) NCaT, (d) CNCaT.*

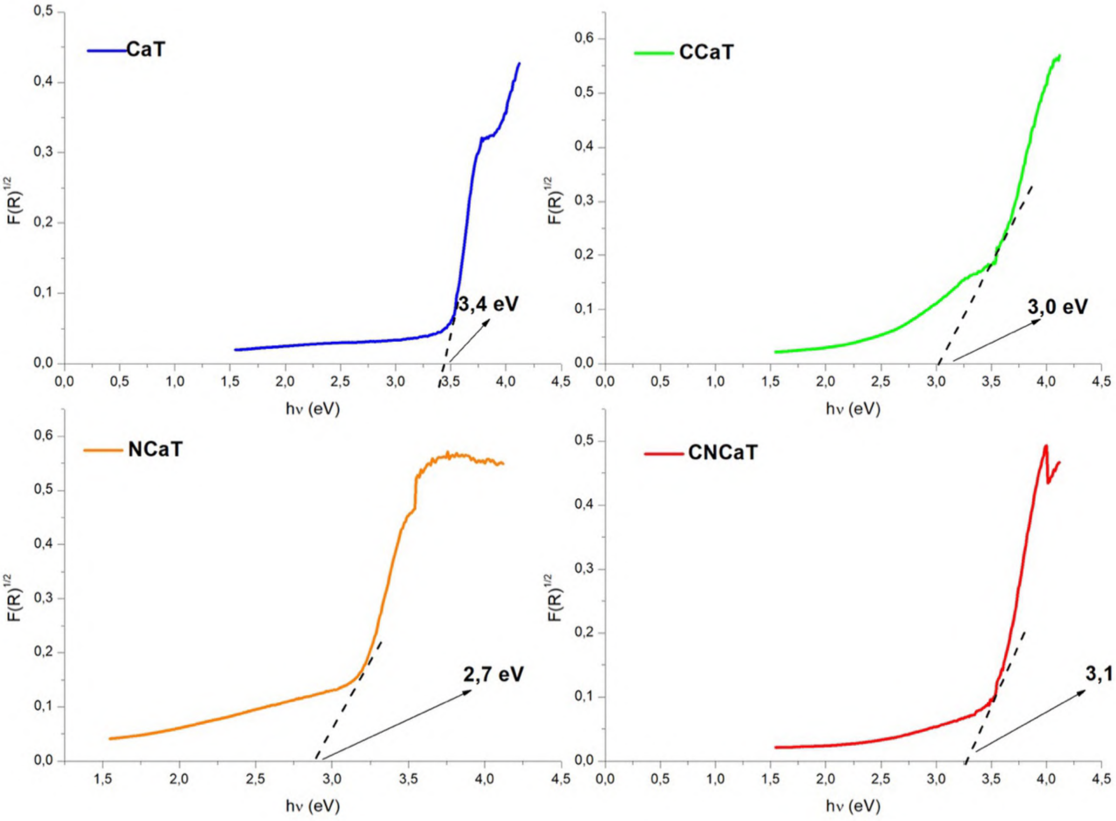

Figure 47: *Tauc plots and energy band gap values of CaT (blue), CCaT (green), NCaT (orange), CNCaT (red).*

Graph 46 showed the adsorption ability of all materials in the UV region. Only CCaT and NCaT (Figure 46 b, c) were observed to absorb in the visible region – with the latter owning the highest absorption ability – compared to CaT and CNCaT (Figure 46 a, d).

As described in the literature, $CaTiO_3$ (Figure 47) had the biggest band gap of 3,4 eV, therefore its absorption in the visible region was absent[39]. Whereas the doped materials showed lower band gaps, supporting the possible formation of intra-gap energy levels, related to the narrowing of the band gaps. Since the ionic radius and the electronegativity of O^{2-} and N^{3-} are similar, the substitution of N^{3-} on oxygen vacancies is facilitated. In addition, since the potential energy of N 2p orbitals is higher than that of O 2p, the band gap could be effectively reduced[44].

Eventually, for all the perovskites it was observed a color change from the white of bare perovskites to a cream/yellow of the doped ones, supporting the observed changes in the absorptive behavior.

Comparing the DRS spectra of calcium-based materials with the barium-based ones, CaT showed a wider starting band gap (3,4 eV) than $BaTiO_3$ (3,0 eV), as elsewhere reported[38]. However, the narrowing ability after doping between the two materials was comparable.

The doping effect on the two perovskites was different. In fact, C and CN doping influenced $BaTiO_3$ greater than $CaTiO_3$. This was probably related to the lower amounts of carbon and nitrogen in CNBaT (0,06% nitrogen and 1,42% carbon) than CNCaT (0,07% nitrogen and 2,70% carbon). In CNCaT, a high amount of carbon was detected that could increase the adsorption, but it promoted also the recombination[30].

FT-IR spectroscopy was applied to determine the functional groups on perovskites surface.

The results relative to barium-based perovskites are reported in Figure 48.

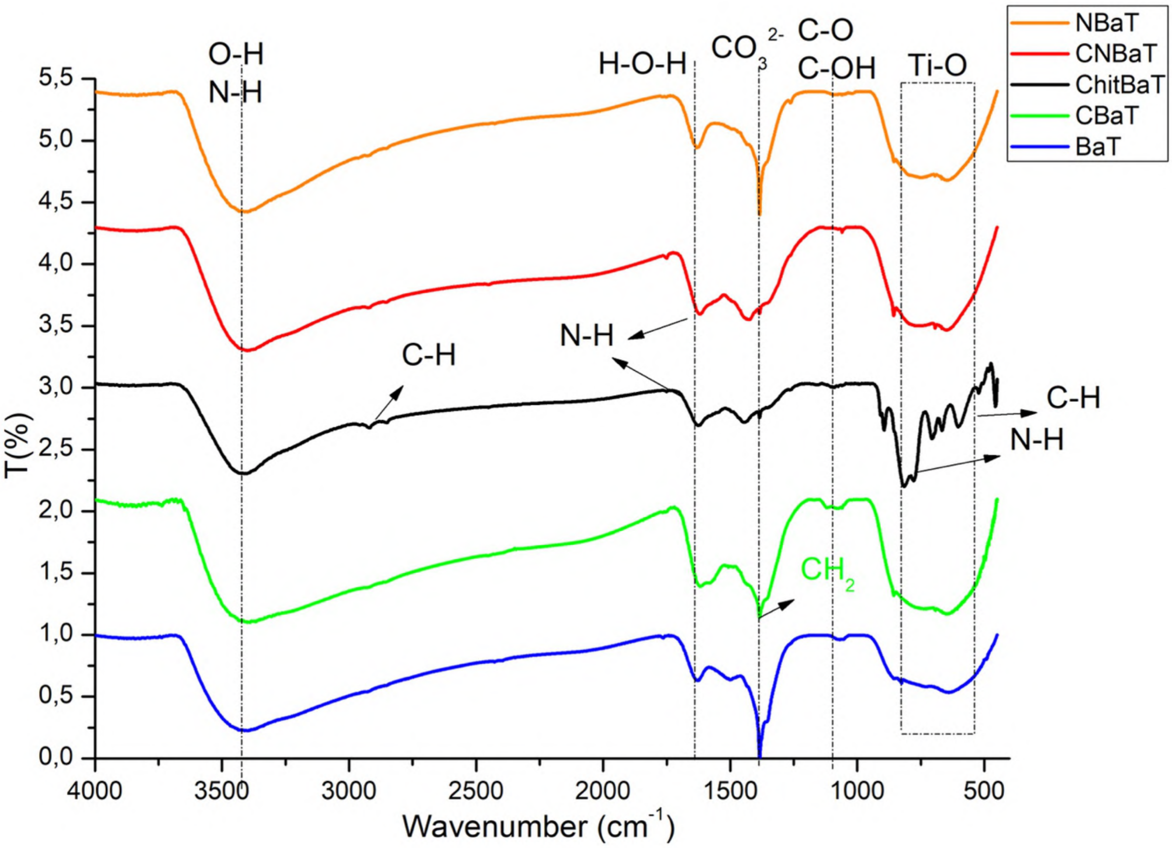

Figure 48: *IR spectra of Ba-based perovskites: BaT (blue), CBaT (green), NBaT (orange), CNBaT (red), ChitBat (black).*

As expected, the infrared profiles of these perovskites were similar with several signals in common, except for some peaks which can be reconducted to doping with heteroatoms. At first, NBaT and BaT profiles were comparable, supporting the previous characterizations which reported the non-doping of NBaT. For all samples, a band between 3500-3400 cm^{-1} was observed relative to the stretching mode of O-H groups. In the same wavenumbers' interval, bands due to N-H stretching of amine groups of CN, and chitosan in doped $BaTiO_3$ were detected[77]. The band at 1630 cm^{-1} was attributed to the H-O-H bending, which derived from the physical adsorption of water on the perovskite surface[61]. At the same wavenumber, for CN and chitosan $BaTiO_3$, there was N-H bending belonging to the amine groups[77]. The adsorption band at 1450 cm^{-1} is characteristic of carbonate groups on the perovskite surface, that could be correlated to the XRD analysis (Figure 19); whereas in CBaT this band could be also attributed to C-H bending due to the insertion of glucose in the perovskite lattice or to the superficial carbon deposition[60]. The band at 1090 cm^{-1} is indicative of -C-O and C-OH stretching of doped carbon in the perovskites structure or of alcohol groups present in the materials surface[78],[79]. For chitosan this stretching was characteristic for its polysaccharidic structure[80]. The formation of barium titanate network was seen from the band between 800 and 400 cm^{-1} which represents Ti-O stretching[81]. The introduction of chitosan in $BaTiO_3$ structure was also supported by the peaks at 727-627 cm^{-1}relative to N-H and C-O wagging of amino-groups, and N-C-N bending, which was overlapped with Ti-O[82]. Also C-H rocking at 600 cm^{-1} and C-H stretching at 2913 cm^{-1} determined the presence of chitosan[80]. The IR spectrum of chitosan was different from the other doped samples and its jagged morphology was possibly due to a superficial deposition of the material without entering the perovskite structure, as supported by the SEM analysis in Figure 21 i, l.

IR spectra of calcium-based perovskites are reported in Figure 49.

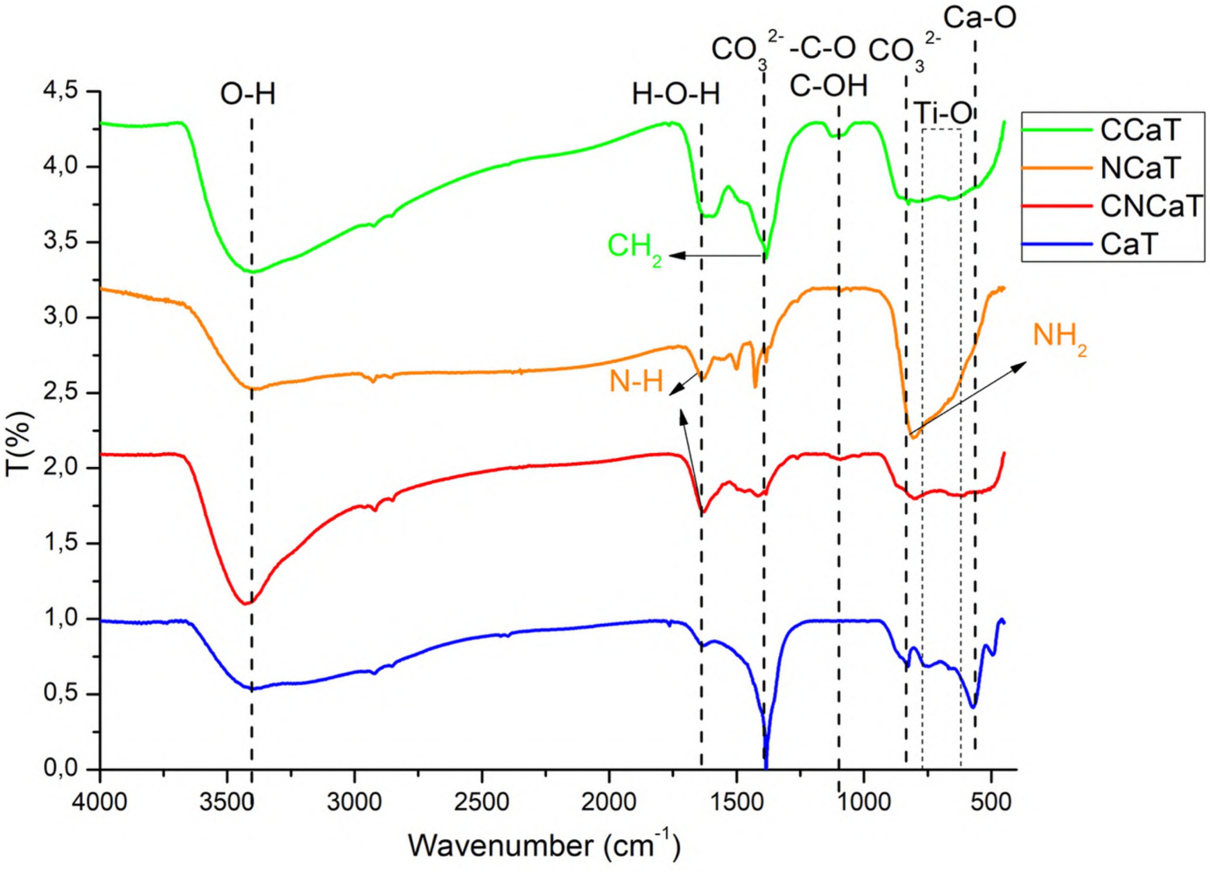

Figure 49: *IR spectra of Ca-based perovskites: CaT (blue), CCaT (green), NCaT (orange), CNCaT (red).*

As for $BaTiO_3$, $CaTiO_3$ IR spectra presented similar profiles to the other doped perovskites. Between 3400 and 3500 cm^{-1}, there was a band relative to the stretching mode of O-H groups that could derive from physically adsorbed water on the material surface. This was supported also by the peak at 1630 cm^{-1} related to H-O-H bending[78]. At 1450 cm^{-1} and 865 cm^{-1} there were bands corresponding to the asymmetric stretching of CO_3^{2-}groups. These carbonate groups could be generated by the adsorption of carbon dioxide from the atmosphere on the perovskites surface[67]. $CaTiO_3$ perovskites also showed a band at 1090 cm^{-1} characteristics of -C-O and C-OH stretching[78],[79]. The formation of calcium titanate structure was given by the band between 800 and 400 cm^{-1} related to Ti-O stretching mode and, for untreated $CaTiO_3$, the stretching vibration of Ca-O was reported at 550 cm^{-1} [67]. Nitrogen doping was confirmed by the peak at 1400 cm^{-1} related to N-H bending of amino groups at 1630 cm^{-1} and by the wide band between 800 and 500 cm^{-1}. In addition, in CCaT at 1450 cm^{-1} there was a band that could be attributed to C-H bending due to the insertion of glucose in the lattice or to surface deposited carbon, as suggested by EDX (Figures 35, 36) and by the jagged morphology observed in Figure 32 c[60].

4.1.3 PHOTOCATALYTIC TESTS

4.1.3.1 GAS-PHASE PHOTOREDUCTION TESTS.

CO_2 photoreduction was performed in a gas phase batch reactor with CO_2/H_2O molar ratio of 13,3. The experimental conditions are reported in Table 8.

Table 8: *Experimental conditions of CO_2 photoreduction*

PARAMETERS	UV LIGHT	SOLAR LIGHT
CO_2/H_2O	13,3	13,3
Temperature (°C)	60	60
Pressure (atm)	1	1
Time (hours)	6	6
Irradiance (W/m^2)	40	1000
Catalyst mass (mg)	10	10

The gas-chromatograph was calibrated for methane and hydrogen as products.

The hypothesized mechanism of the gas phase reaction consists of a fast deoxygenation of CO_2 that leads, in this case, to methane generation as the favored product, which involves the formation of carbon radicals as given below[83] (Figure 50).

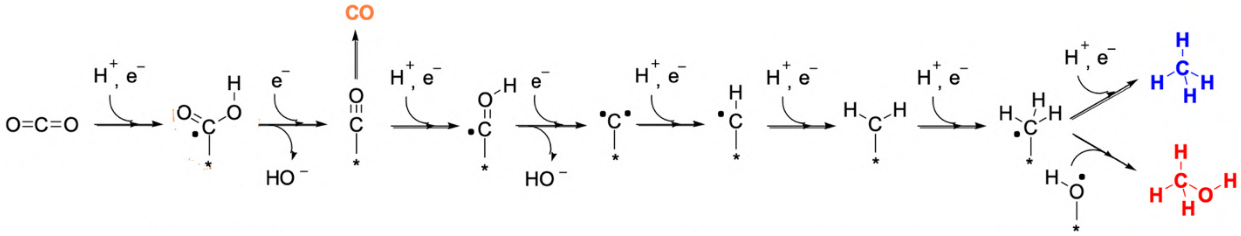

Figure 50: *CO_2 deoxygenation mechanism.*

Hydrogen production is led back to water splitting reaction from vapor water [84].

The results of photocatalytic tests for barium-based perovskites under both UV and solar light are reported in Figure 51, while all TON are reported in Table 9.

Table 9: *Methane and hydrogen TON for all Ba-based samples.*

Sample	TON CH_4 UV ($\mu mol/g_{cat}$)	TON CH_4 solar ($\mu mol/g_{cat}$)	TON H_2 UV ($\mu mol/g_{cat}$)	TON H_2 solar ($\mu mol/g_{cat}$)
BaT	2,0	0,0	7,1	0,0
CBaT	2,3	1,1	1,6	2,7
NBaT	2,1	0,0	0,0	0,0
CNBaT	1,0	1,0	0,0	4,8
ChitBaT	1,8	1,0	1,2	0,0
P25	5,8	0,0	6,4	0,0

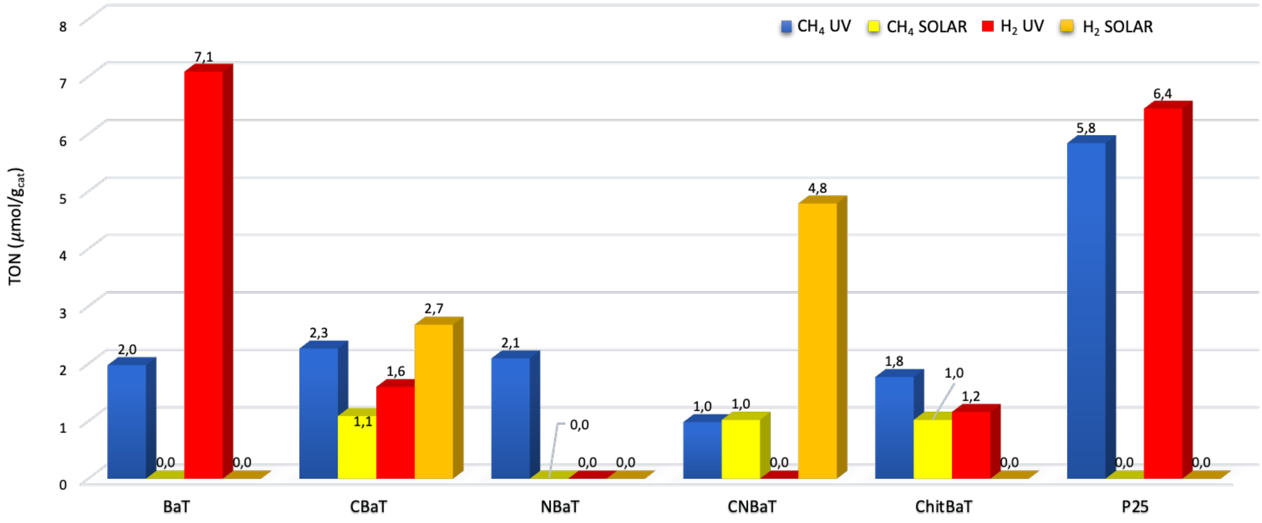

Figure 51: *CH_4 production under both UV (blue) and solar light (yellow) and H_2 production under both UV (red) and solar light (orange).*

All the materials were found to be active for CO_2 photoreduction under UV light leading to a similar CH_4 production around to 2 μmol/g$_{cat}$, whereas P25 showed methane production of about 5,8 μmol/g$_{cat}$. As reported in Figure 51*,* H_2 production decreased in the doped samples if compared to bare $BaTiO_3$ and P25, supporting a higher selectivity towards C-based products. Moreover, except for NBaT, the doped perovskites were all able to produce methane under solar light irradiation, compared to P25 and bare $BaTiO_3$, although only CBaT and CNBaT were able to produce H_2.

As expected, BaT activity under solar light was hampered due to its band gap of 3 eV[85], whereas doping the perovskite with carbon, specifically in the case of CBaT, allowed an improvement in the photo reactivity. In general, the introduction of heteroatoms in the material structure for CNBaT, ChitBaT and CBaT enabled a decrease in the energy difference between valence and conduction bands, likely related to the generation of intra-gap energy layers, and which was observed to improve the activity under solar light, in accordance with DRS analysis (Figure 44). However, NBaT did not show activity if irradiated by solar light, but under UV radiation its TON relative to CH_4 production was about 2,1 μmol/g$_{cat}$. Also, in this case the similar behavior of NBaT to BaT was supported by the fact that nitrogen was not doped in barium titanate (as reported in paragraph 3.1.2). However, compared to NBaT, BaT produced H_2. This was probably due to the particles average dimensions, which were bigger in NBaT than BaT, and which affected the selectivity or the kinetics of the reaction. From the photocatalytic tests and from DRS analysis, CBaT was the best catalyst under both UV and solar light irradiating conditions. This activity was probably related to the higher surface area of CBaT (196 m^2/g) compared to the other catalysts, which provided a better absorbance of the reactant molecules on the perovskite surface. In addition, the intra-gap energy layers formation was supported by Tauc plot in Figure 45, in which the band gap value was equal to 2,3 eV. These intra-gap states likely reduced the recombination events and improved the photocatalytic activity of CBaT[86].

The TON obtained from the photocatalytic tests of calcium-based perovskites under both UV and solar light are reported respectively in Figure 52 and are summarized in Table 10.

Table 10: *Methane and hydrogen TON for all Ca-based samples.*

Sample	**TON CH_4 UV (μmol/g_{cat})**	**TON CH_4 solar (μmol/g_{cat})**	**TON H_2 UV (μmol/g_{cat})**	**TON H_2 solar (μmol/g_{cat})**
CaT	1,0	0,0	0,0	0,0
CCaT	1,8	0,8	17,3	2,2
NCaT	1,6	1,8	0,0	2,8
CNCaT	0,9	0,5	7,5	0,0
P25	5,8	0,0	6,4	0,0

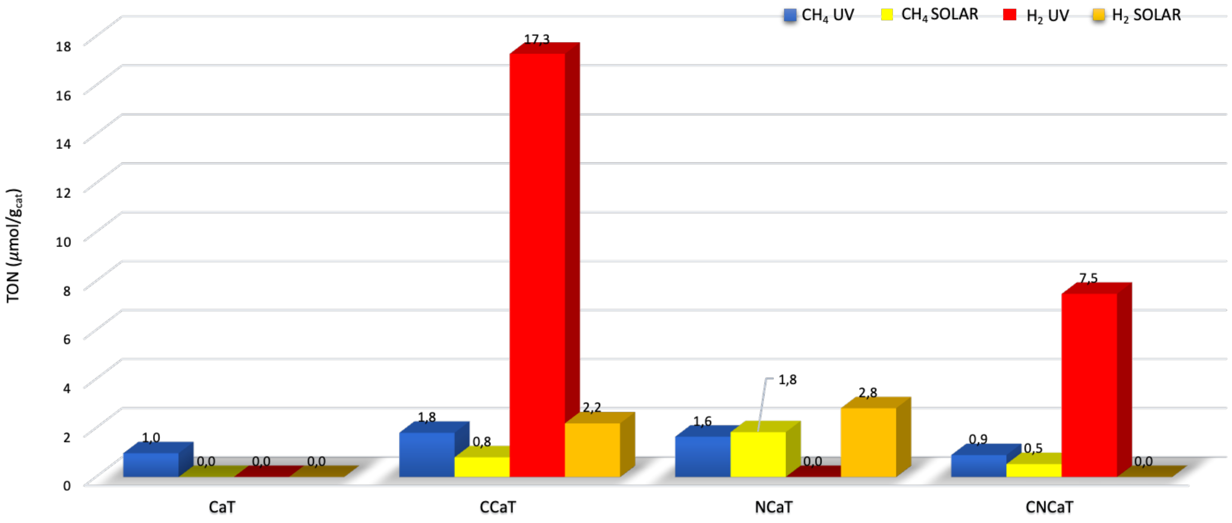

Figure 52: *CH_4 production under both UV (blue) and solar light (yellow) and H_2 production under both UV (red) and solar light (orange).*

All calcium-based perovskites exhibited activity under UV light. The CH_4 productivity of Ca-based perovskites went from 0,9 for CNCaT to 1,8 μmol/g_{cat} for CCaT, although P25 showed the highest methane production. H_2 was generated by CCaT and CNCaT, which recorded a production of 17,3 μmol/g_{cat} and 7,5 μmol/g_{cat} respectively, both being higher than that of P25 (6,4 μmol/g_{cat}). Under simulated solar irradiation, hydrogen was produced only by CCaT and NCaT.

Except for $CaTiO_3$, each perovskite was active under both UV and solar light. NCaT sample showed the best photocatalytic activity with a methane production equal to 1,83 μmol/g_{cat} upon visible light conditions. This activity was strongly supported by the absorption ability of the sample in the visible region, as reported by DRS spectra (Figure 47). Furthermore, the increased methane production was possibly attributed to a better interaction of N superficial functional groups – such as amino groups, as supported by FT-IR spectra - with CO_2 during the reaction. In fact, nitrogen have basic and electron-donating properties which can bind to the electrophilic carbon in CO_2. Moreover, the electrophilic carbon atoms in the amino groups can re-bind to the nucleophilic oxygen atoms of CO_2[87]. The increased affinity towards methane due to the presence of nitrogen function has already been reported[45]. CNCaT sample was less active under both solar and UV light, likely related to a non-synergistic effect between carbon and nitrogen dopants in calcium titanate.

Under UV light, the best activity amongst the Ca-based samples was attributed to CCaT, which also produced H_2.

Therefore, the experimental data supported that the addition of carbon and nitrogen into the perovskite structure was able to improve the photoactivity under both UV and solar light, compared to the untreated samples.

A comparison between Ca-based and Ba-based perovskites for methane production under both UV and solar light is reported in Figure 53 and in Table 11.

Table 11: *Relative amounts* of *methane and hydrogen produced under both UV and solar light.*

Sample	CH_4 UV (%)	H_2 UV (%)	CH_4 solar (%)	H_2 solar (%)
CaT	100	0	0	0
CCaT	9	91	27	73
NCaT	100	0	39	61

CNCaT	11	89	100	0
P25	48	52	0	0
BaT	22	78	0	0
CBaT	59	41	29	71
NBaT	100	0	0	0
CNBaT	100	0	17	83
ChitBaT	60	40	100	0

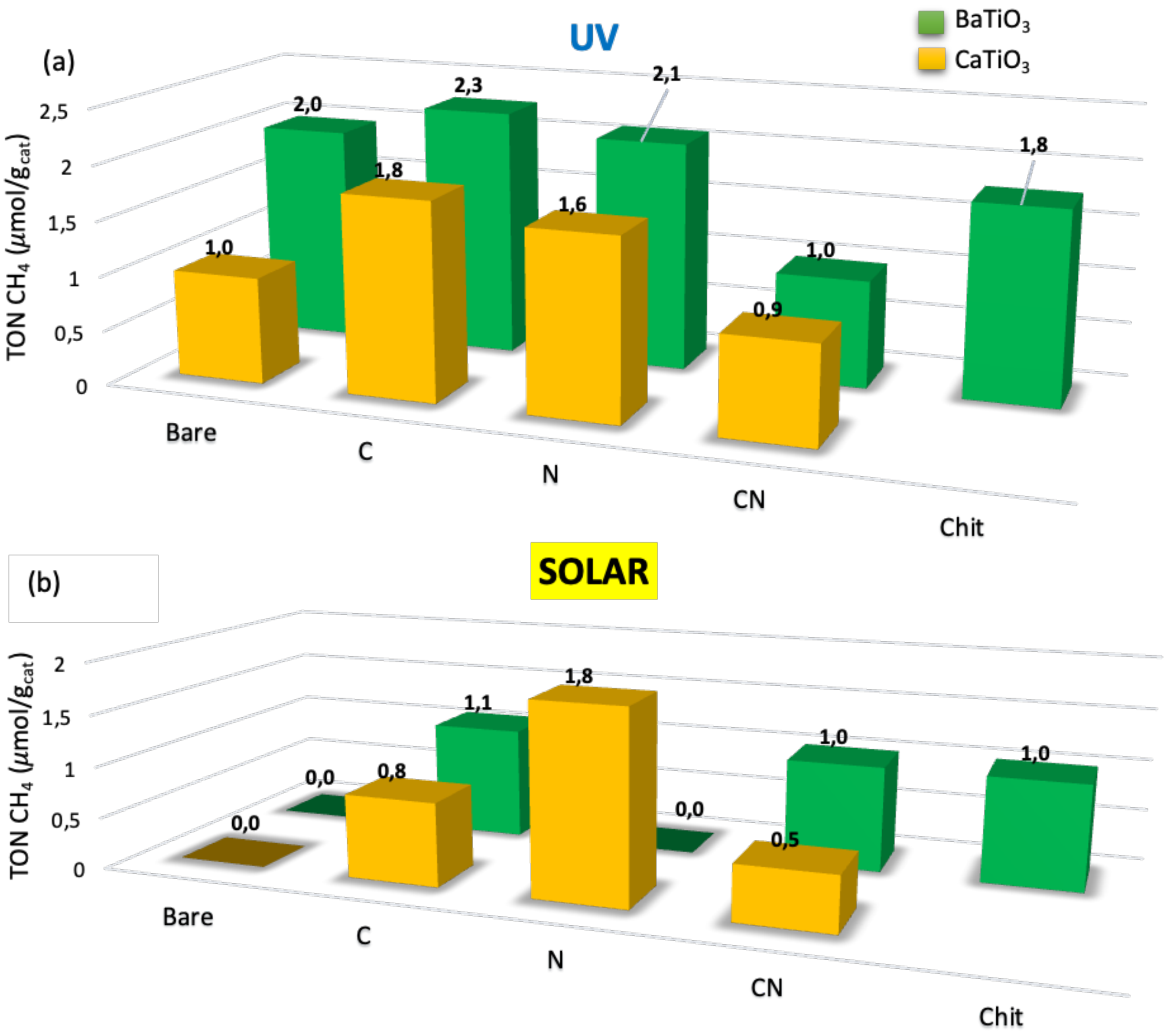

Figure 53: *Comparison between Ca and Ba-based perovskites for CH_4 production under both (a) UV and (b) solar light.*

As reported in Table 11, CCaT under solar light improved the selectivity to methane production (from 9 to 27%) but reduced the selectivity to hydrogen (from 91 to 73%). The presence of carbon particles on the perovskite surface could interact with the reagents during the reaction leading to higher selectivity to CH_4. To support this, thanks to CCaT surface area (313 m^2/g) and small particles dimensions, obtained by physisorption measurement and TEM analysis, compared to the other materials, it could absorb greater amounts of carbon dioxide.

On the other side, NCaT showed a selectivity decrement toward methane and increment toward hydrogen when irradiated by solar light. The elemental analysis of this sample showed the presence of nitrogen, even if in little amounts (0,05%). For this reason, probably the dopant was not present in the required amount to narrow the band gap and improve the methane production.

CNCaT presented an improvement in the solar activity towards the production of methane (from 11 to 100%). Therefore, under visible light the synergistic effect of the two dopants led to higher selectivity to the desired product.

In Table 11, it was also reported that CBaT had a similar behavior to NCaT, because it showed a decrement to methane selectivity (from 59 to 29%) and increment to hydrogen production (from 41 to 71%). The elemental and FT-IR analysis reported the presence of carbon in the perovskite and the XRD pattern showed an amorphous system due to the carbon introduction. DRS spectrum confirmed its activity in the visible region. In addition, CBaT presented the higher surface area among the Ba-perovskites. This improved the interaction with the reagents and therefore the photoactivity. Probably the decrement in methane selectivity was related to inert carbon deposition on its surface, as confirmed by SEM analysis. Also, CNBaT had similar selectivity values.

ChitBaT presented an improvement in methane selectivity (from 60 to 100%) under solar light. The previous characterizations confirmed chitosan presence in the perovskite structure and the activity of ChitBaT in the visible region.

On the other hand, NBaT was not active under solar light, and it had similar trend to bare BaT. The previous characterizations demonstrated that $BaTiO_3$ was not doped by nitrogen, otherwise it probably was decomposed during the hydrothermal synthesis. Also in literature it was reported that the synthetic method could affect the insertion of nitrogen in the lattice[30]. For future research, it will be necessary to improve the synthetic approach in order to maintain nitrogen in the proper amount into the perovskite structure. In addition, it is important to underline that the operating conditions (reaction time and pH) for the synthesis of bare BaT and NBat were different, and this explained their different particle sizes respectively 20 and 22 nm and surface area values respectively 181 and

145 m^2/g. This was possibly correlated to the different production of H_2. Overall, under UV light C-doped perovskites were more performant than the other bare and doped ones. This was due to their higher surface areas which permitted a greater interaction with CO_2. The surface area and porosity of the catalysts played a fundamental role in the photocatalytic reaction because they enabled a better interaction with the reactants involved, being adsorbed efficiently on the surface. This led to a major transfer of charge on the material surface. Between the two C-doped materials, CBaT was the most performant (2,3 $\mu mol/g_{cat}$). This sample was characterized by higher pore volumes of 0,34 cm^3/g, which could be fundamental for the interaction with the reagents.

Under solar irradiation NCaT exhibited the best activity in methane production (1,8 $\mu mol/g_{cat}$). Nitrogen could act as additional adsorption site for carbon dioxide, improving the photocatalytic activity.

CBaT was the most active among Ba-perovskites in the same conditions with methane production of 1,1 $\mu mol/g_{cat}$.

In general, under both UV and solar light the doped perovskites reached higher TON values than the bare ones. These were not active if irradiated by solar simulator.

Overall, except CNBaT and CNCaT and NBaT, the doped samples presented higher activity compared to the bare ones. Co-doping effect was not comparable with single doping one, although it enabled the activity in the visible region.

4.1.3.2 LIQUID-PHASE PHOTOREDUCTION TESTS.

CO_2 photoreduction in liquid phase was performed in a pressurized batch reactor at the University of Milan, in the group of Professor Ilenia Rossetti. The tests were conducted with a UV mercury lamp and at alkaline pH. The experimental conditions are reported in Table 12.

Table 12: *Experimental conditions of CO_2 photoreduction in liquid phase.*

PARAMETERS	VALUES
Temperature (°C)	80
Pressure (atm)	18
Time (hours)	6

Irradiance (W/m^2)	120
Catalyst concentration (g/L)	0,03
Hole scavenger concentration (g/L)	1,6
pH	14

In liquid phase, a wide variety of reagents such as gases, liquids and solids can be used. In addition, the properties of the solution such as the dielectric constant and viscosity can be varied depending on the desired result. However, compared to the gas phase, the radiation penetrates less though the liquid medium and there is a limited mass transfer due to the low diffusivity of the reaction medium. High pressure and alkaline environment were applied to improve CO_2 solubility in water, while sodium sulfite (Na_2SO_3) was added to the reaction mixture as hole-scavenger. The latter is a non-harmful compound, which can be oxidized into sulfate by photogenerated holes. A drawback of working at pH=14 is the formation of carbonate ions (CO_3^- or HCO_3^-) which are more difficult to be reduced than CO_2[59]. In liquid phase, methanol, formic acid, and formaldehyde could be detected. They derive from the fast hydrogenation of carbon dioxide reported in Equation 8. However, in these conditions, methanol formation is hindered because i) the high amount of hydroxide ions lead to the formation of HCO_3^- species and therefore to the generation of formic acid, and ii) methanol is usually obtained upon HCOOH and HCHO reduction[88] (Equation 8). In this reaction, H_2 generation can be also derived from the accumulation of organic compounds[84].

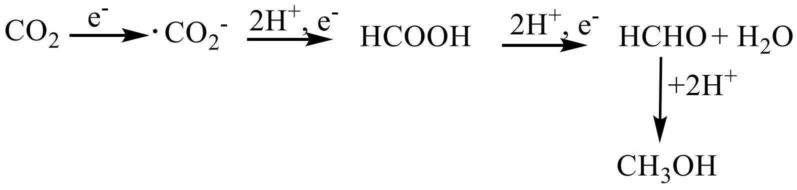

$$CO_2 \xrightarrow{e^-} \cdot CO_2^- \xrightarrow{2H^+,\, e^-} HCOOH \xrightarrow{2H^+,\, e^-} HCHO + H_2O \xrightarrow{+2H^+} CH_3OH$$

Equation 8

In the tests performed, only formic acid was detected. Figure 54 reports the results of CO_2 photoreduction tests in liquid phase for barium-based perovskites. Table 13 shows the reactivity increment of doped catalysts compared to $BaTiO_3$, used as benchmark.

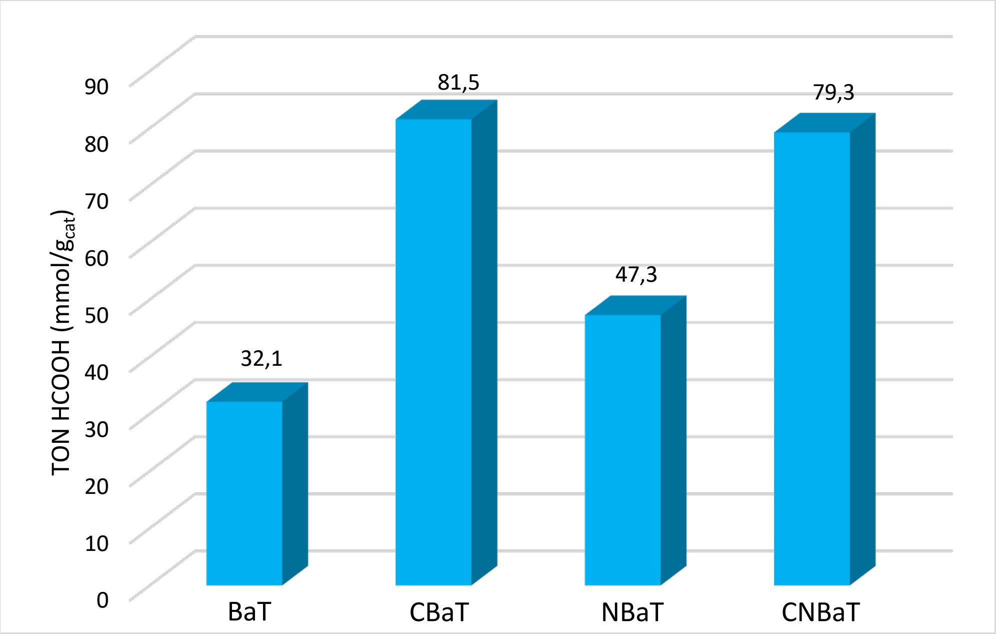

Figure 54: *HCOOH production in liquid phase under UV light.*

Table 13*: Reactivity increment of doped catalysts from the reference.*

Catalyst	***Reactivity increment ratio from the reference ($BaTiO_3$)***
BaT	-
CBaT	*2,5*
NBaT	*1,5*
CNBaT	*2,5*

The activity of bare $BaTiO_3$ was found to be lower than the doped samples, but higher than the co-doped one. In fact, CBaT resulted in a formic acid production of 81,5 mmol/g$_{cat}$, supporting the promising photocatalytic behavior previously recorded in the gas phase tests. In general, doping with individual elements – either C or N – resulted in an overall positive effect on the photo-activity, both in liquid and gas phase. CBaT, NBaT and CNBaT doped materials presented respectively 2,5, 1,5 and 2,5 of reactivity increment than the benchmark BaT.

In Figure 55, the results of photocatalytic tests for calcium-based perovskites are reported. Table 14 reports the reactivity increment of doped catalysts compared to $CaTiO_3$, used as benchmark for Ca-based samples.

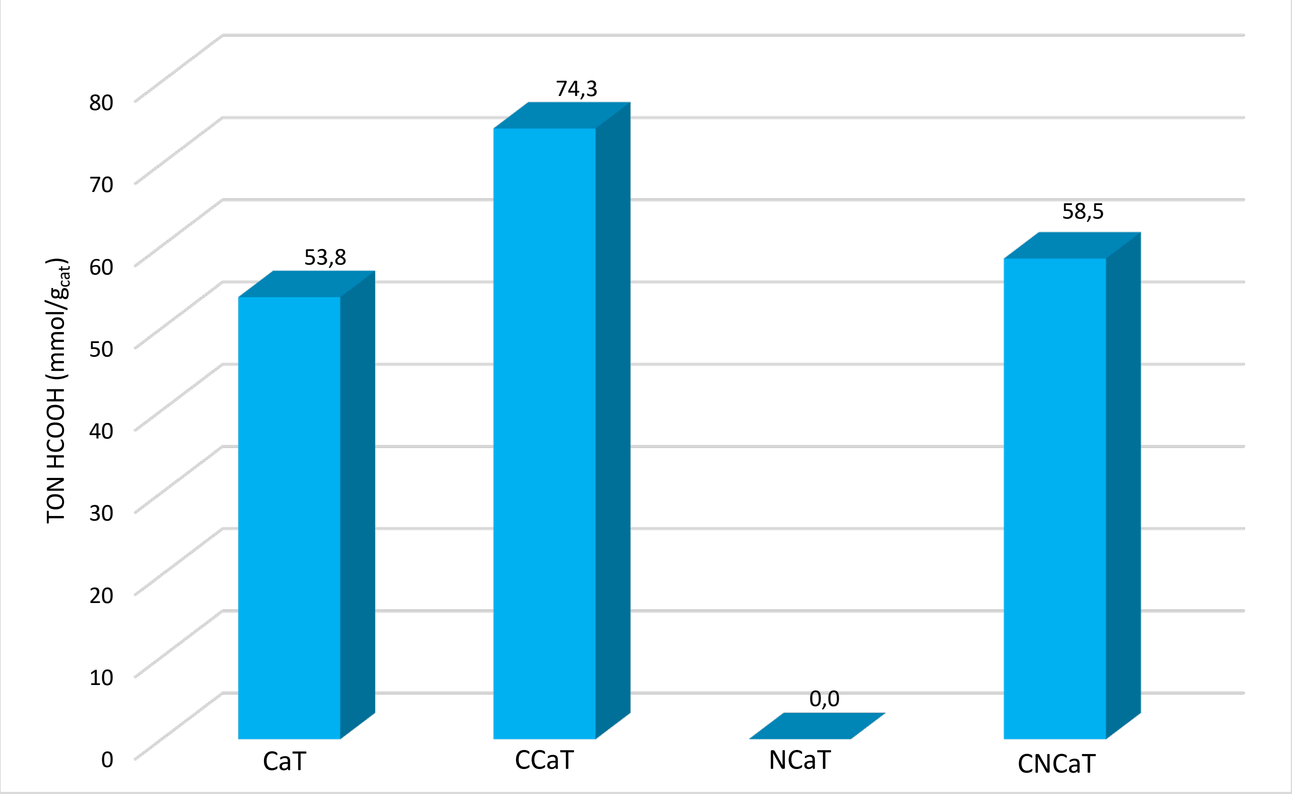

Figure 55: *HCOOH production in liquid phase under UV light.*

Table 14*: Reactivity increment of doped catalysts from the reference.*

Catalyst	***Reactivity increment ratio from the reference ($CaTiO_3$)***
CaT	-
CCaT	*1,4*
NCaT	*0,0*
CNCaT	*1,1*

The TON of bare $CaTiO_3$ was higher than that of $BaTiO_3$, whereas the doped and co-doped catalysts presented higher values. CCaT amongst calcium-based perovskites showed the best photoactivity in liquid phase with a TON equal to 74,3 mmol/g$_{cat}$. In addition, it presented an increment of 1,4 in the reactivity, compared to $CaTiO_3$. This result is in accordance with the tests performed in gas phase, where carbon doped $CaTiO_3$ reached higher values than the other doped $CaTiO_3$-based samples under UV light.

Conversely, CNCaT showed a higher reactivity with respect of $CaTiO_3$, recording a TON of 58,5 mmol/g_{cat} and a reactivity increment of 1,1. However, NCaT did not show any activity.

Overall, CBaT achieved the best photocatalytic activity in CO_2 reduction in liquid phase, under UV light irradiation. These results related well with the ones obtained in gas phase test, in which CBaT was the most active perovskite under UV light. In addition, it was observed that the activity trend of doped materials in liquid phase was different from the same materials used in gas phase. In fact, both Ba-based and Ca-based materials doped with both carbon and nitrogen where more active if compared to the results obtained in the other phase. Probably the increase solubility of CO_2 in basic conditions permitted a better interaction with CN catalysts. Furthermore, Ba-based catalysts presented higher activity in liquid phase than Ca-based ones, in accordance with the results obtained in gas phase.

4.2 CARBON DOTS-BASED CATALYSTS

4.2.1 STRUCTURAL AND MORPHOLOGICAL CHARACTERIZATIONS

CD_s samples synthetized from o-phenylenediamine via microwave-assisted method were characterized with UV-Vis spectroscopy and methylene blue photodegradation and then tested in CO_2 photoreduction.

XRD was performed to characterize the crystal structure of carbon dots.

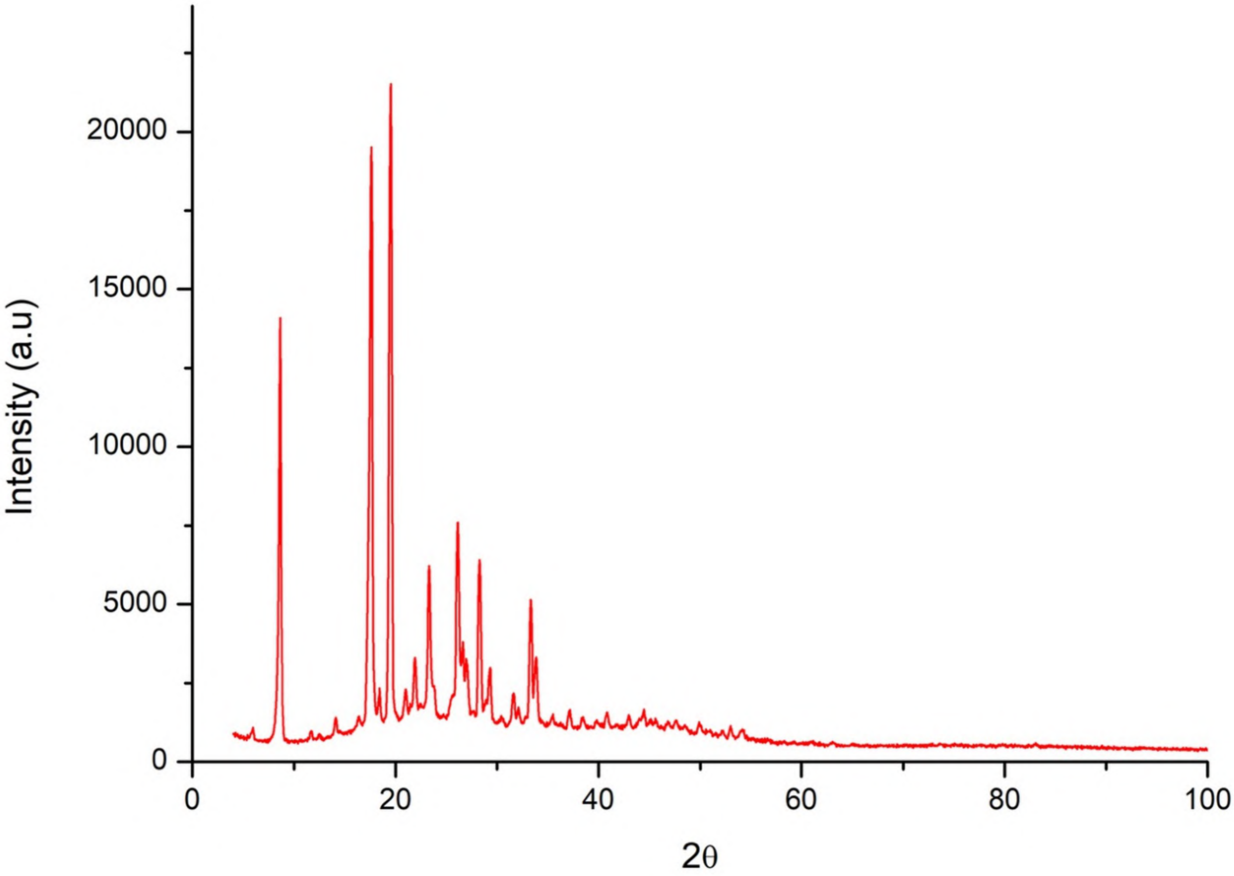

Figure 56: *XRD spectra of CDs.*

XRD spectrum suggested the presence of both crystalline and amorphous phases, with typical signals attributed to carbon dots. The crystalline phase denoted larger structures, whereas the amorphous was attributed to smaller carbon particles. From Sherrer's law, the crystallites dimensions were determined and ranged from 45 to 50 nm.

TEM analysis was performed, and results are shown in Figure 57.

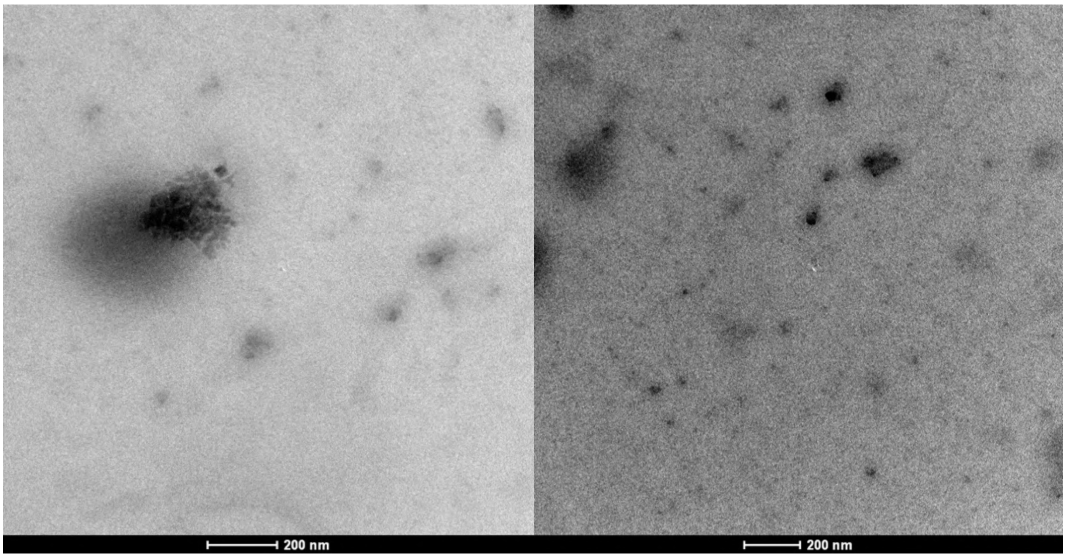

Figure 57: *TEM images of carbon dots.*

The synthesized carbon dots were detected both as single nano-spheres with <10 nm size, and as aggregated structures of about 200 nm.

4.2.2 OPTICAL AND SPECTROSCOPIC CHARACTERIZATIONS.

UV-vis spectroscopy was applied in order to analyze the absorption range of synthetized carbon dots. The results are reported in Figure 58.

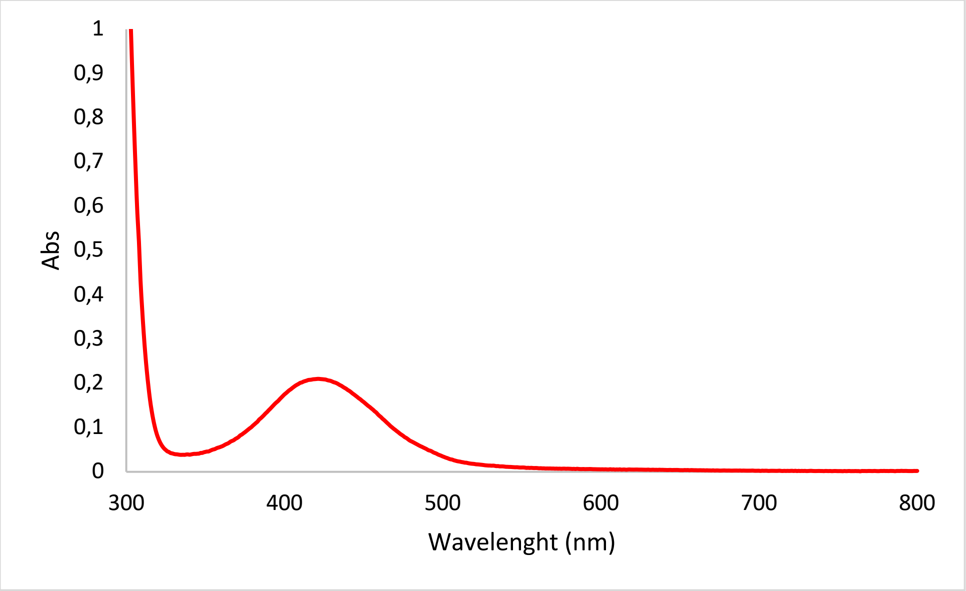

Figure 58: *UV-Vis absorption spectra of CD$_s$ carbon dots.*

As reported in the graph, CD_s carbon dots absorbed in the range between 330 and 500 nm so in the visible region. These absorption peaks can be ascribed either to the n-π* transition of C-O and C=O bonds, or to the functional groups on their surface[53]. In addition, CD_s were found to be able to absorb in the UV region of the spectrum.

The photoluminescence of the material was measured to determine the emission ability of the sample upon light excitation. Figure 59 reports the PL and PLE spectra of carbon dots.

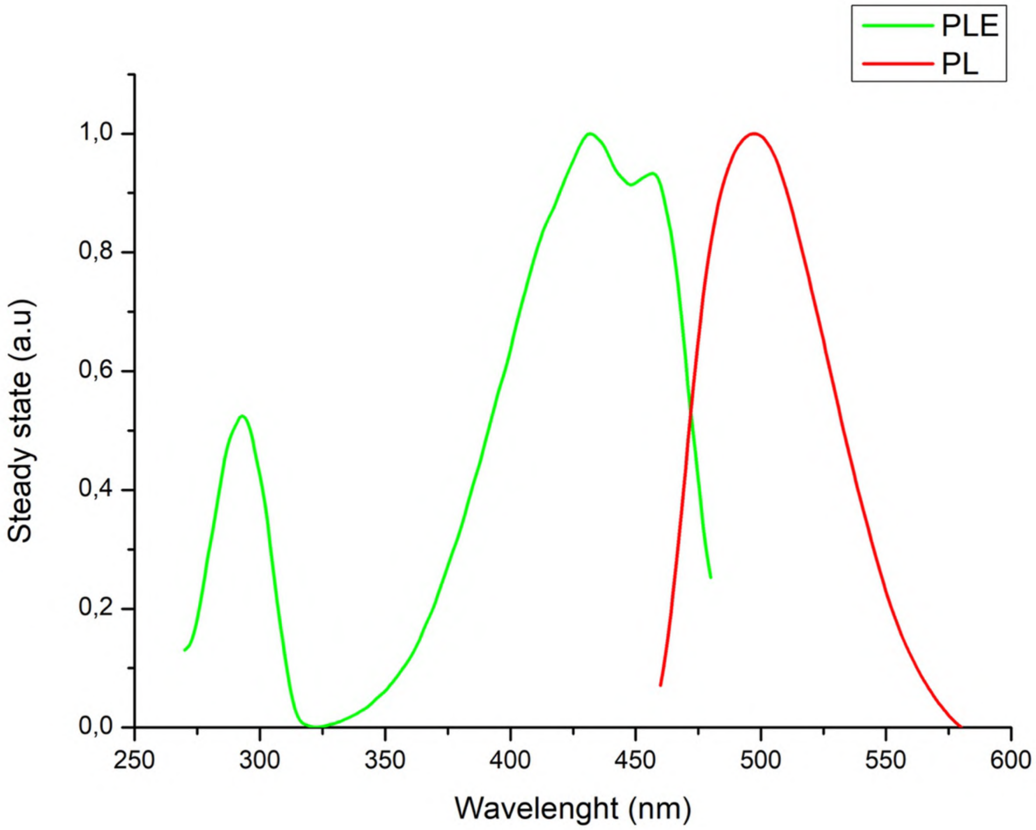

Figure 59: *PL and PLE spectra of CD_s.*

Excitation PLE spectrum showed a band in the UV region, centered at 280 nm and a band centered at 400 nm related to green color (Figure 60 a).

The emission spectrum (PL) showed a visible light emission centered at 500 nm (yellow). This was also supported by the yellow color of CDs-containing solution, as reported in Figure 60 b.

4.2.3 PHOTOCATALYTIC TESTS

4.2.3.1 METHYLENE BLUE PHOTODEGRADATION

Carbon dots were tested for the water depuration ability, by measuring the methylene blue photodegradation activity under both UV and solar light irradiation (Table 15). CDs were supported on P25 and $BaTiO_3$ either with wet impregnation or in situ during the synthesis, to explore their role as co-catalysts. Figure 60 (a) showed the color change of solutions obtained at regular intervals up to 120 minutes during the photocatalytic reaction. The colors shift was proportional to photodegradation efficiency.

However, a brownish color was observed after 90 minutes exposure to UV. This effect was attributed either to the UV-mediated degradation of the carbon dots, or to their instability in aqueous media[89]. As it is reported in Figure 60 (b), the decreasing of the photoluminescence of the solutions supported the instability of carbon dots in water under a prolongated exposure to UV light.

Table 15: *Experimental conditions for methylene blue photodegradation under UV and solar light.*

PARAMETERS	VALUES
Temperature (°C)	25
Time (hours)	2
Irradiance UV (W/m^2)	40
Irradiance Solar (W/m^2)	1000
Catalyst concentration (g/L)	0,16
pH	6

Figure 60: *Methylene blue photodegraded solutions (a) taken at different time during the photocatalytic reaction, (b) irradiated by UV light.*

Figure 61 reports the absorbance of methylene blue under UV irradiation as a function of time. The curves were extrapolated by taking the methylene blue maximum absorption wavelength (λ_{max}) that is equal to 665 nm. It was then determined how the C/C_0 ratio varied over time to λ_{max}, where C represents the concentration measured at different times, and C_0 is the concentration at t=0.

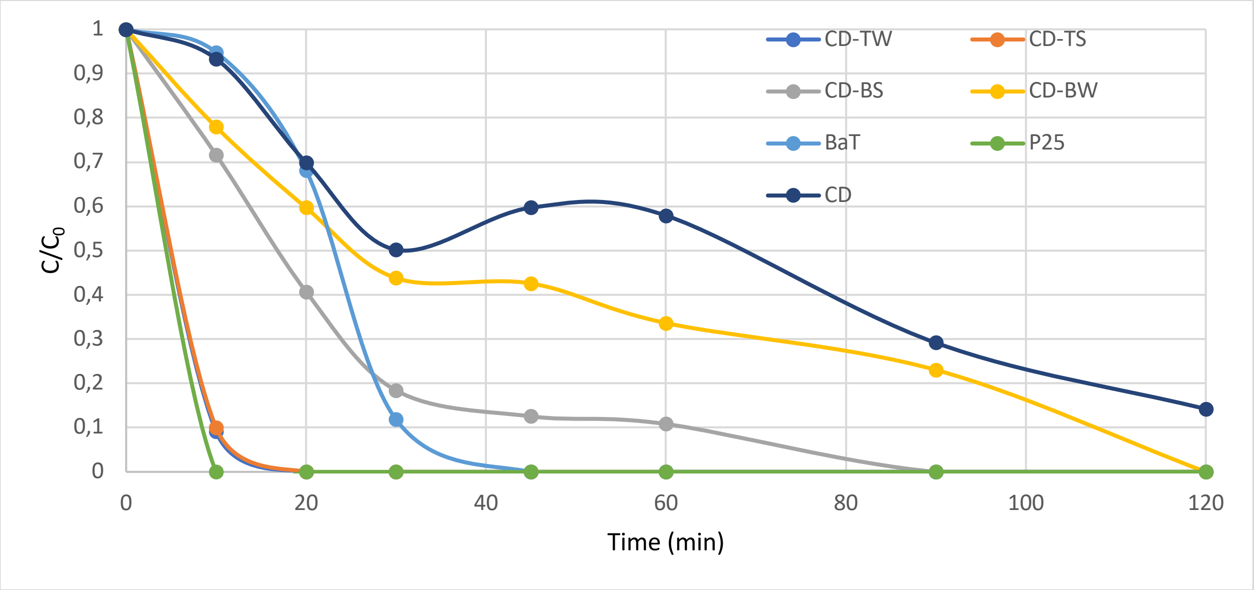

Figure 61: *Photodegradation curve of methylene blue under UV light catalyzed by CDs.*

When the catalyst was added to the methylene blue solution, the dye molecules adsorbed on the catalyst's surface[90].

It could be observed that after 10 minutes P25 was able to totally degrade methylene blue. A similar profile was obtained by CD-TW and CD-TS. However, bare CDs presented a lower activity in the methylene blue degradation, suggesting their role as co-catalysts rather than as catalysts themselves. While $BaTiO_3$ showed the complete photodegradation of the dye after 45 minutes from the start of the reaction, only CD-BS seemed to have a similar trend, while the wet impregnated sample (CD-BW) was found to be less active and to require up to 120 minutes for the complete degradation. In any case, supported CDs led to higher photodegradation efficiency than bare CDs. However, the synthetic method for titania-based CDs did not affect the photodegradation ability, but in barium titanate-based CDs the microwave assisted-method had influenced positively the results than the ones prepared by wet impregnation.

Figure 62 reports the degradation curves of methylene blue under solar light irradiation as a function of time.

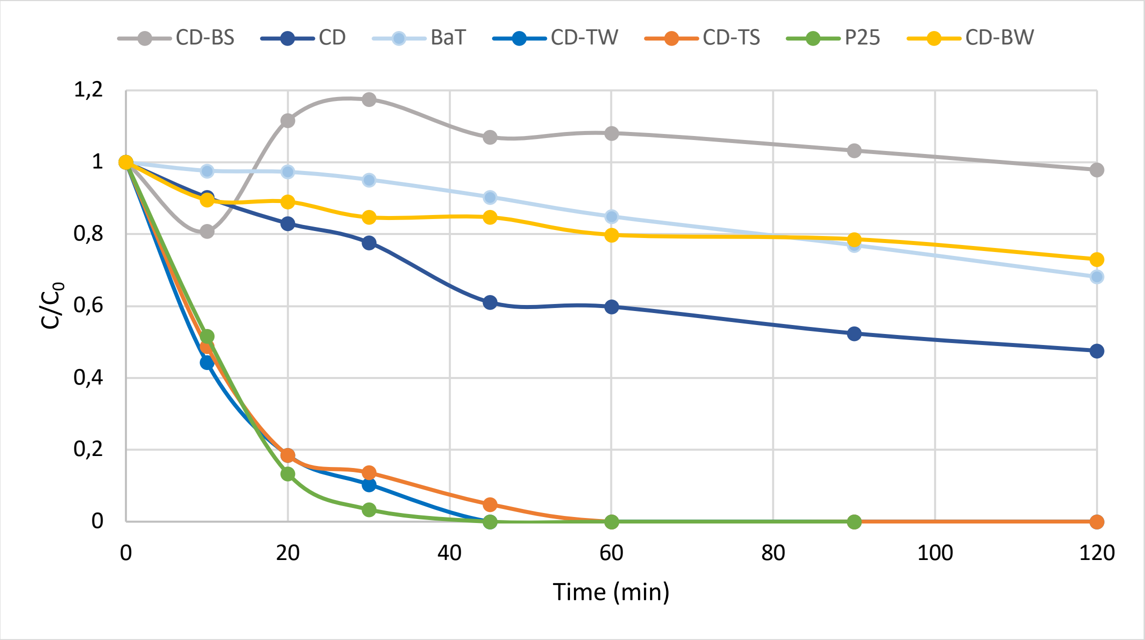

Figure 62: *Photodegradation curve of methylene blue under solar light catalyzed by CDs.*

As reported in Figure 62, titania-based catalysts (P25, CD-TW, CD-TS) were the most active under solar light at 1000 W/m^2 of irradiance. In fact, after 40 and 60 minutes these catalysts were able to totally degrade methylene blue. On the contrary, barium titanate-based carbon dots (BaT and CD-BW) were less active, and they degraded only about 30% of methylene blue. In addition, CD-BS synthetized in situ via microwave-assisted method did not present activity under solar light in aqueous solution. This was related to the solvent used for their preparation meaning ethanol which probably did not work in water. In general, the solvent influenced CDs activity and affected their interactions, resulting in different optical properties[89].

Bare CDs were able to degrade 50% of the colorant after 120 minutes and they seemed to have a better ability in photodegradation than when supported on BaT. However, supporting CDs on P25 via in situ or wet impregnation led to higher photodegradation efficiency than the bare ones.

Comparing the obtained results to Figure 61 where the same samples were exposed under UV light, it was seen that P25, CD-TW and CD-TS had a similar trend in both conditions, but they were more active under UV irradiation, in which after 10 and 20 minutes they totally degraded methylene blue. CD-BS and CD-BW degraded greatest amount of the colorant under UV light, in particular CD-BS, that after 90 minutes led to complete degradation, whereas under solar light it did not work.

Also, BaT was more active under UV light than solar one. This was in accordance with the results obtained for BaT in the photocatalytic gas phase tests reported in the previous section.

CDs were active under both conditions, but they degraded almost 85% of methylene blue under UV light compared to 50% under solar light.

4.2.3.2 GAS-PHASE PHOTOREDUCTION TESTS

All samples were tested in CO_2 photoreduction. The experimental conditions are reported in Table 16.

Table 16: *Experimental conditions for CO_2 photoreduction under both UV and solar light.*

PARAMETERS	UV LIGHT	SOLAR LIGHT
CO_2/H_2O	13,3	13,3
Temperature (°C)	60	60

Pressure (atm)	1	1
Time (hours)	6	6
Irradiance (W/m^2)	40	1000
Catalyst mass (mg)	10	10

The results of the photocatalytic test are reported in Figure 63.

Bare CDs did not work in gas phase under both UV and solar light but when supporting them on BaT or P25, CDs activity increased. In particular, the best TON were obtained for CD-TS and CD-BS catalysts, prepared in situ by microwave-assisted method using ethanol as the solvent. CD-TS reached a TON equal to 1,5 $\mu mol/g_{cat}$ under solar light, but bare P25 and CDs did not work under the same conditions.

In fact, as reported in the work of *Mkhari et al.* CDs strong fluorescent emissions could be reduced or quenched when CDs were transferred from a solvent to the solid phase because of their agglomeration. So to overcome these drawbacks, CDs could be placed on a support[91]. Therefore, associating carbon dots with a support enabled to stabilize them and to improve their photocatalytic efficiency.

In addition, as seen in the optical and spectroscopical characterizations, carbon dots were active in the visible region of the spectrum. Also, CD-BS showed the ability for methane production with a TON of 0,7 $\mu mol/g_{cat}$ under solar light, whereas bare BaT was not active under the same conditions. It was also noted that wet impregnated titania or barium titanate with CDs were not active under solar light. This was probably due to a non-homogeneous dispersion of the nanoparticles on the support matrix that could be confirmed in future by SEM and TEM characterizations of the supported catalysts. Furthermore, carbon dots deposition in situ probably favored carbon dots interaction with the support.

On the other side, under UV light, except for CD and CD-BW, all the materials produced methane, in particular CD-TW that reached TON of 2,6 $\mu mol/g_{cat}$. The activity of this sample under UV conditions was probably attributed to the presence of P25 as support, which showed the best photocatalytic efficiency under these conditions (5,8 $\mu mol/g_{cat}$).

CD-TS and CD-BS presented activity also under UV light. In particular, methane selectivity was implemented for CD-BS passing from solar to UV conditions, and the same decreased for CD-TS passing from solar to UV.

Overall, it was confirmed that supporting carbon dots on a solid matrix could improve the photoactivity in gas phase under both UV and solar light. In particular, CD-TS and CD-BS prepared and supported in situ led to the best photocatalytic activity in gas phase.

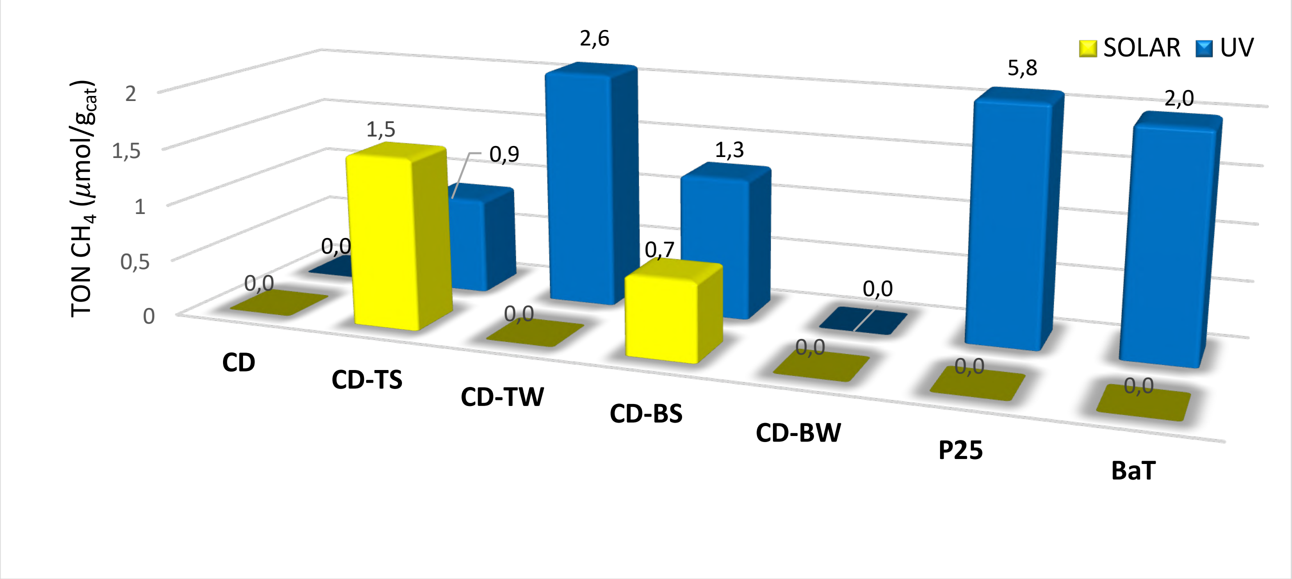

Figure 63: *CH_4 production under both UV and solar light.*

Hence, the prepared carbon dots showed activity both in gas and liquid phase and under both UV and solar light. Specifically, CD-TS and CD-BS showed their activity in methylene blue photodegradation under UV light. Whereas CD-BS did not degrade the colorant under solar light, even if it was active in gas phase under the same irradiation. This was related to water used as solvent in methylene blue solution, in which probably CD-BS were not stable.

CD-TW totally degraded methylene blue after 20 minutes under UV light and after 40 minutes under solar light. On the contrary in gas phase, they worked only under UV irradiation.

CD-BW were active under both conditions in methylene blue photodegradation, whereas they did not work in gas phase. This was probably related to the wet impregnation method which did not lead to a homogeneous dispersion of CDs on BaT. This will be confirmed through some characterizations in future.

Thus, CD-TS prepared in situ with microwave-assisted method showed the best photocatalytic activity in CO_2 photoreduction under solar light.

Overall supporting carbon dots on a solid matrix permitted to improve the photocatalytic efficiency under both UV and solar light in both methylene blue photodegradation and CO_2 photoreduction.

5. CONCLUSIONS

Carbon dioxide conversion into high value-added products is a strategy aiming at reducing its concentration in the atmosphere. Photocatalysis is still drawing attention in virtu of the possibility to use of direct solar energy - without any additional energy input - to make the reaction to take place.

In this thesis work, the use of perovskites such as $BaTiO_3$ and $CaTiO_3$ as new photocatalytic materials for CO_2 photoreduction under solar light was investigated. The two strategies used to enhance the photoactivity were doping and associating carbon dots as co-catalysts.

Doping the materials with heteroatoms affected the morphology and crystalline structure of the starting perovskites. C and CN-doping of both materials resulted in crystal structures modifications, promoting the generation of amorphous phases, which resulted in increased surface areas, but also in a reduced band gap, implementing the absorption of radiation in the visible region. However, the use of chitosan as both carbon and nitrogen source changed $BaTiO_3$ morphology, although the crystal structure was preserved. In addition, doping the material with nitrogen encountered technical difficulties that will be improved and overcome in the future, changing the synthesis conditions.

The two types of perovskites had similar morphological and crystal structures properties and presented analogous activity trend. However, Ba-Based materials showed higher activities in CO_2 photoreduction. Among Ba-perovskites, in virtue of the high surface area and pores volume, and to the narrow band gap, the employment of C-$BaTiO_3$ as photocatalyst led to the best performance under solar light, both in gas and liquid phases. For Ca-based perovskites, under solar irradiation the best performance was obtained by N-$CaTiO_3$, confirming the positive interaction of the dopant with carbon dioxide and likely due to its ability improve the adsorption of light in the visible region.

The employment of carbon dots as co-catalysts for $BaTiO_3$ and P25 in methylene blue photodegradation led to good results for CD-TW and CD-TS, which were the most active under solar light. Conversely, supporting carbon dots on titania and barium titanate in situ (CD-TS and CD-BS) led to the best results if irradiated by solar light. Therefore, the synthetic method affected the CO_2 photoreduction efficiency.

Hence, from these experimental data it was proved that doping the perovskites led to a more pronounced effect in improving CO_2 photoreduction toward methane under solar light, compared to using carbon dots as co-catalysts, whose use for now remains a challenge.

6. BIBLIOGRAPHY

(1) Al-Ghussain, L. Global Warming: Review on Driving Forces and Mitigation. *Environ. Prog. Sustain. Energy* **2019**, *38* (1), 13–21. https://doi.org/10.1002/ep.13041.

(2) *Global Warming Effects*. Environment. https://www.nationalgeographic.com/environment/article/global-warming-effects (accessed 2023-07-01).

(3) *Climate Change: Global Temperature | NOAA Climate.gov*. http://www.climate.gov/news-features/understanding-climate/climate-change-global-temperature (accessed 2023-07-01).

(4) Kweku, D.; Bismark, O.; Maxwell, A.; Desmond, K.; Danso, K.; Oti-Mensah, E.; Quachie, A.; Adormaa, B. Greenhouse Effect: Greenhouse Gases and Their Impact on Global Warming. *J. Sci. Res. Rep.* **2018**, *17* (6), 1–9. https://doi.org/10.9734/JSRR/2017/39630.

(5) Gong, Y.; Peng, Y.; Wang, S.; Wang, S. Production of N_2O in Two Biologic Nitrogen Removal Processes: A Comparison between Conventional and Short-Cut Nitrogen Removal Processes. *Front. Environ. Sci. Eng.* **2014**, *8* (4), 589–597. https://doi.org/10.1007/s11783-013-0571-7.

(6) Buis, A. *Steamy Relationships: How Atmospheric Water Vapor Amplifies Earth's Greenhouse Effect*. Climate Change: Vital Signs of the Planet. https://climate.nasa.gov/explore/ask-nasa-climate/3143/steamy-relationships-how-atmospheric-water-vapor-amplifies-earths-greenhouse-effect/ (accessed 2023-07-02).

(7) Guo, L.; Yang, Y.; Fraser, P. J.; Velders, G. J. M.; Liu, Z.; Cui, D.; Quan, J.; Cai, Z.; Yao, B.; Hu, J.; Fang, X. Projected Increases in Emissions of High Global Warming Potential Fluorinated Gases in China. *Commun. Earth Environ.* **2023**, *4* (1), 1–9. https://doi.org/10.1038/s43247-023-00859-6.

(8) Castro, P. J.; Aráujo, J. M. M.; Martinho, G.; Pereiro, A. B. Waste Management Strategies to Mitigate the Effects of Fluorinated Greenhouse Gases on Climate Change. *Appl. Sci.* **2021**, *11* (10), 4367. https://doi.org/10.3390/app11104367.

(9) US EPA, O. *Overview of Greenhouse Gases*. https://www.epa.gov/ghgemissions/overview-greenhouse-gases (accessed 2023-07-02).

(10) Leggett, J.A. The United Nations Framework Convention on Climate Change, the Kyoto Protocol, and the Paris Agreement: A Summary. **2020**.

(11) *Conferenza delle Nazioni Unite sui cambiamenti climatici (COP 27), vertice sull'attuazione per*

il clima, Sharm el-Sheikh, Egitto, 7 e 8 novembre 2022. https://www.consilium.europa.eu/it/meetings/international-summit/2022/11/07-08/ (accessed 2023-07-02).

(12) Hertwich, E. G.; Ali, S.; Ciacci, L.; Fishman, T.; Heeren, N.; Masanet, E.; Asghari, F. N.; Olivetti, E.; Pauliuk, S.; Tu, Q.; Wolfram, P. Material Efficiency Strategies to Reducing Greenhouse Gas Emissions Associated with Buildings, Vehicles, and Electronics—a Review. *Environ. Res. Lett.* **2019**, *14* (4), 043004. https://doi.org/10.1088/1748-9326/ab0fe3.

(13) Ritchie, H.; Roser, M.; Rosado, P. CO_2 and Greenhouse Gas Emissions. *Our World Data* **2020**.

(14) IPCC_AR6_SYR_LongerReport.Pdf. https://www.ipcc.ch/report/ar6/syr/downloads/report/IPCC_AR6_SYR_LongerReport.pdf (accessed 2023-07-05).

(15) Gür, T. M. Carbon Dioxide Emissions, Capture, Storage and Utilization: Review of Materials, Processes and Technologies. *Prog. Energy Combust. Sci.* **2022**, *89*, 100965. https://doi.org/10.1016/j.pecs.2021.100965.

(16) Tinker, P. B.; Ingram, J. S. I.; Struwe, S. Effects of Slash-and-Burn Agriculture and Deforestation on Climate Change. *Agric. Ecosyst. Environ.* **1996**, *58* (1), 13–22. https://doi.org/10.1016/0167-8809(95)00651-6.

(17) Huang, C.-H.; Tan, C.-S. A Review: CO_2 Utilization. *Aerosol Air Qual. Res.* **2014**, *14* (2), 480–499. https://doi.org/10.4209/aaqr.2013.10.0326.

(18) Bui, M.; Adjiman, C. S.; Bardow, A.; Anthony, E. J.; Boston, A.; Brown, S.; Fennell, P. S.; Fuss, S.; Galindo, A.; Hackett, L. A.; Hallett, J. P.; Herzog, H. J.; Jackson, G.; Kemper, J.; Krevor, S.; Maitland, G. C.; Matuszewski, M.; Metcalfe, I. S.; Petit, C.; Puxty, G.; Reimer, J.; Reiner, D. M.; Rubin, E. S.; Scott, S. A.; Shah, N.; Smit, B.; Trusler, J. P. M.; Webley, P.; Wilcox, J.; Mac Dowell, N. Carbon Capture and Storage (CCS): The Way Forward. *Energy Environ. Sci.* **2018**, *11* (5), 1062–1176. https://doi.org/10.1039/C7EE02342A.

(19) *IEA – International Energy Agency*. IEA. https://www.iea.org/data-and-statistics (accessed 2023-07-10).

(20) Dey, S.; Dhal, G. C.; Mohan, D.; Prasad, R. Application of Hopcalite Catalyst for Controlling Carbon Monoxide Emission at Cold-Start Emission Conditions. *J. Traffic Transp. Eng. Engl. Ed.* **2019**, *6* (5), 419–440. https://doi.org/10.1016/j.jtte.2019.06.002.

(21) Chen, X.; Liu, Y.; Wu, J. Sustainable Production of Formic Acid from Biomass and Carbon Dioxide. *Mol. Catal.* **2020**, *483*, 110716. https://doi.org/10.1016/j.mcat.2019.110716.

(22) Sun, L.; Wang, Y.; Guan, N.; Li, L. Methane Activation and Utilization: Current Status and Future Challenges. *Energy Technol.* **2020**, *8* (8), 1900826. https://doi.org/10.1002/ente.201900826.

(23) Zhang, X.; Zhang, G.; Song, C.; Guo, X. Catalytic Conversion of Carbon Dioxide to Methanol: Current Status and Future Perspective. *Front. Energy Res.* **2021**, *8*, 621119. https://doi.org/10.3389/fenrg.2020.621119.

(24) Alvarado, M. The Changing Face of the Global Methanol Industry. **2016**. https://www.methanol.org/wp-content/uploads/2016/07/IHS-ChemicalBulletin-Issue3-Alvarado-Jun16.pdf.

(25) Nguyen, T. P.; Nguyen, D. L. T.; Nguyen, V.-H.; Le, T.-H.; Vo, D.-V. N.; Trinh, Q. T.; Bae, S.-R.; Chae, S. Y.; Kim, S. Y.; Le, Q. V. Recent Advances in TiO_2-Based Photocatalysts for Reduction of CO_2 to Fuels. *Nanomaterials* **2020**, *10* (2), 337. https://doi.org/10.3390/nano10020337.

(26) Ma, J.; Sun, N.; Zhang, X.; Zhao, N.; Xiao, F.; Wei, W.; Sun, Y. A Short Review of Catalysis for CO_2 Conversion. *Catal. Today* **2009**, *148* (3–4), 221–231. https://doi.org/10.1016/j.cattod.2009.08.015.

(27) Habisreutinger, S. N.; Schmidt-Mende, L.; Stolarczyk, J. K. Photocatalytic Reduction of CO_2 on TiO_2 and Other Semiconductors. *Angew. Chem. Int. Ed.* **2013**, *52* (29), 7372–7408. https://doi.org/10.1002/anie.201207199.

(28) Arora, I.; Chawla, H.; Chandra, A.; Sagadevan, S.; Garg, S. Advances in the Strategies for Enhancing the Photocatalytic Activity of TiO_2: Conversion from UV-Light Active to Visible-Light Active Photocatalyst. *Inorg. Chem. Commun.* **2022**, *143*, 109700. https://doi.org/10.1016/j.inoche.2022.109700.

(29) Wu, H.; Li, X.; Tung, C.; Wu, L. Semiconductor Quantum Dots: An Emerging Candidate for CO_2 Photoreduction. *Adv. Mater.* **2019**, *31* (36), 1900709. https://doi.org/10.1002/adma.201900709.

(30) Trevisan, V.; Olivo, A.; Pinna, F.; Signoretto, M.; Vindigni, F.; Cerrato, G.; Bianchi, C. L. C-N/TiO_2 Photocatalysts: Effect of Co-Doping on the Catalytic Performance under Visible Light. *Appl. Catal. B Environ.* **2014**, *160–161*, 152–160. https://doi.org/10.1016/j.apcatb.2014.05.015.

(31) Weng, B.; Qi, M.-Y.; Han, C.; Tang, Z.-R.; Xu, Y.-J. Photocorrosion Inhibition of Semiconductor-Based Photocatalysts: Basic Principle, Current Development, and Future Perspective. *ACS Catal.* **2019**, *9* (5), 4642–4687. https://doi.org/10.1021/acscatal.9b00313.

(32) Som, I.; Roy, M. Recent Development on Titania-Based Nanomaterial for Photocatalytic CO_2 Reduction: A Review. *J. Alloys Compd.* **2022**, *918*, 165533. https://doi.org/10.1016/j.jallcom.2022.165533.

(33) Mgolombane, M.; Majodina, S.; Bankole, O. M.; Ferg, E. E.; Ogunlaja, A. S. Influence of Surface Modification of Zinc Oxide–Based Nanomaterials on the Photocatalytic Reduction of Carbon Dioxide. *Mater. Today Chem.* **2021**, *20*, 100446. https://doi.org/10.1016/j.mtchem.2021.100446.

(34) Shen, H.; Peppel, T.; Strunk, J.; Sun, Z. Photocatalytic Reduction of CO_2 by Metal-Free-Based Materials: Recent Advances and Future Perspective. *Sol. RRL* **2020**, *4* (8), 1900546. https://doi.org/10.1002/solr.201900546.

(35) Le, Q. V.; Nguyen, V.-H.; Nguyen, T. D.; Sharma, A.; Rahman, G.; Nguyen, D. L. T. Light-Driven Reduction of Carbon Dioxide: Altering the Reaction Pathways and Designing Photocatalysts toward Value-Added and Renewable Fuels. *Chem. Eng. Sci.* **2021**, *237*, 116547. https://doi.org/10.1016/j.ces.2021.116547.

(36) Variar, A. G.; M.S., R.; Ail, V. U.; S., S. P.; K., S.; Tahir, M. Influence of Various Operational Parameters in Enhancing Photocatalytic Reduction Efficiency of Carbon Dioxide in a Photoreactor: A Review. *J. Ind. Eng. Chem.* **2021**, *99*, 19–47. https://doi.org/10.1016/j.jiec.2021.04.017.

(37) Sasirekha, N.; Basha, S.; Shanthi, K. Photocatalytic Performance of Ru Doped Anatase Mounted on Silica for Reduction of Carbon Dioxide. *Appl. Catal. B Environ.* **2006**, *62* (1–2), 169–180. https://doi.org/10.1016/j.apcatb.2005.07.009.

(38) Mai, H.; Chen, D.; Tachibana, Y.; Suzuki, H.; Abe, R.; Caruso, R. A. Developing Sustainable, High-Performance Perovskites in Photocatalysis: Design Strategies and Applications. *Chem. Soc. Rev.* **2021**, *50* (24), 13692–13729. https://doi.org/10.1039/D1CS00684C.

(39) Kanhere, P.; Chen, Z. A Review on Visible Light Active Perovskite-Based Photocatalysts. *Molecules* **2014**, *19* (12), 19995–20022. https://doi.org/10.3390/molecules191219995.

(40) Kwak, B. S.; Kang, M. Evaluation of Photoreduction Performance of CO_2 to CH_4 with H_2O Over Alkaline-Earth-Metal-Based Peroskite Nanoparticles. *J. Nanosci. Nanotechnol.* **2017**, *17* (10), 7351–7357. https://doi.org/10.1166/jnn.2017.14794.

(41) Panthi, G.; Park, M. Approaches for Enhancing the Photocatalytic Activities of Barium Titanate: A Review. *J. Energy Chem.* **2022**, *73*, 160–188. https://doi.org/10.1016/j.jechem.2022.06.023.

(42) Passi, M.; Pal, B. A Review on CaTiO3 Photocatalyst: Activity Enhancement Methods and Photocatalytic Applications. *Powder Technol.* **2021**, *388*, 274–304. https://doi.org/10.1016/j.powtec.2021.04.056.

(43) Kumari, V.; Mittal, A.; Jindal, J.; Yadav, S.; Kumar, N. S-, N- and C-Doped ZnO as Semiconductor Photocatalysts: A Review. *Front. Mater. Sci.* **2019**, *13* (1), 1–22. https://doi.org/10.1007/s11706-019-0453-4.

(44) Humayun, M.; Qu, Y.; Raziq, F.; Yan, R.; Li, Z.; Zhang, X.; Jing, L. Exceptional Visible-Light Activities of TiO $_2$ -Coupled N-Doped Porous Perovskite LaFeO $_3$ for 2,4-Dichlorophenol Decomposition and CO_2 Conversion. *Environ. Sci. Technol.* **2016**, *50* (24), 13600–13610. https://doi.org/10.1021/acs.est.6b04958.

(45) Domingo-Tafalla, B.; Martínez-Ferrero, E.; Franco, F.; Palomares-Gil, E. Applications of Carbon Dots for the Photocatalytic and Electrocatalytic Reduction of CO_2. *Molecules* **2022**, *27* (3), 1081. https://doi.org/10.3390/molecules27031081.

(46) Habisreutinger, S. N.; Schmidt-Mende, L.; Stolarczyk, J. K. Photocatalytic Reduction of CO_2 on TiO_2 and Other Semiconductors. *Angew. Chem. Int. Ed.* **2013**, *52* (29), 7372–7408. https://doi.org/10.1002/anie.201207199.

(47) Kulandaivalu, T.; Abdul Rashid, S.; Sabli, N.; Tan, T. L. Visible Light Assisted Photocatalytic Reduction of CO_2 to Ethane Using CQDs/Cu_2O Nanocomposite Photocatalyst. *Diam. Relat. Mater.* **2019**, *91*, 64–73. https://doi.org/10.1016/j.diamond.2018.11.002.

(48) Saini, D.; Garg, A. K.; Dalal, C.; Anand, S. R.; Sonkar, S. K.; Sonker, A. K.; Westman, G. Visible-Light-Promoted Photocatalytic Applications of Carbon Dots: A Review. *ACS Appl. Nano Mater.* **2022**, *5* (3), 3087–3109. https://doi.org/10.1021/acsanm.1c04142.

(49) Zhang, J.; Xu, J.; Tao, F. Interface Modification of TiO_2 Nanotubes by Biomass-Derived Carbon Quantum Dots for Enhanced Photocatalytic Reduction of CO_2. *ACS Appl. Energy Mater.* **2021**, *4* (11), 13120–13131. https://doi.org/10.1021/acsaem.1c02760.

(50) Dang, Y.; Li, B.; Feng, X.; Jia, J.; Li, K.; Zhang, Y. Preparation of Iron-Doped Carbon Dots and Their Application in Photocatalytic Reduction of Carbon Dioxide. *ChemPhotoChem* **2023**, *7* (2). https://doi.org/10.1002/cptc.202200156.

(51) Ong, W.-J.; Tan, L.-L.; Chai, S.-P.; Yong, S.-T. Graphene Oxide as a Structure-Directing Agent for the Two-Dimensional Interface Engineering of Sandwich-like Graphene–g-C_3N_4 Hybrid Nanostructures with Enhanced Visible-Light Photoreduction of CO_2 to Methane. *Chem. Commun.* **2015**, *51* (5), 858–861. https://doi.org/10.1039/C4CC08996K.

(52) Farhadian, N.; Akbarzadeh, R.; Pirsaheb, M.; Jen, T.-C.; Fakhri, Y.; Asadi, A. Chitosan Modified N, S-Doped TiO_2 and N, S-Doped ZnO for Visible Light Photocatalytic Degradation of Tetracycline. *Int. J. Biol. Macromol.* **2019**, *132*, 360–373. https://doi.org/10.1016/j.ijbiomac.2019.03.217.

(53) Kang, C.; Huang, Y.; Yang, H.; Yan, X. F.; Chen, Z. P. A Review of Carbon Dots Produced from Biomass Wastes. *Nanomaterials* **2020**, *10* (11), 2316. https://doi.org/10.3390/nano10112316.

(54) Peter Atkins; Julio de Paula. *Chimica Fisica*, Quinta.; Zanichelli, **2012**.

(55) *International Union of Pure and Applied Chemistry*. https://iupac.org/ (accessed 2023-09-06).

(56) Rds_par2015-057.Pdf. https://www.enea.it/it/Ricerca_sviluppo/documenti/ricerca-di-sistema-elettrico/adp-mise-enea-2015-2017/processi-e-macchinari-industriali/rds_par2015-057.pdf (accessed 2023-08-06).

(57) F. James Holler; Stanley R. Crouch. *Fondamenti Di Chimica Analitica*, Terza.; EdiSES, **2015**.

(58) Murzin, A. O.; Samsonova, A. Yu.; Stoumpos, C. C.; Selivanov, N. I.; Emeline, A. V.; Kapitonov, Y. V. Diffuse Reflectance Spectroscopy with Dilution: A Powerful Method for Halide Perovskites Study. *Molecules* **2023**, *28* (1), 350. https://doi.org/10.3390/molecules28010350.

(59) Galli, F.; Compagnoni, M.; Vitali, D.; Pirola, C.; Bianchi, C. L.; Villa, A.; Prati, L.; Rossetti, I. CO_2 Photoreduction at High Pressure to Both Gas and Liquid Products over Titanium Dioxide. *Appl. Catal. B Environ.* **2017**, *200*, 386–391. https://doi.org/10.1016/j.apcatb.2016.07.038.

(60) Utara, S.; Hunpratub, S. Ultrasonic Assisted Synthesis of $BaTiO_3$ Nanoparticles at 25°C and Atmospheric Pressure. *Ultrason. Sonochem.* **2018**, *41*, 441–448. https://doi.org/10.1016/j.ultsonch.2017.10.008.

(61) Phan, T. T. M.; Chu, N. C.; Luu, V. B.; Nguyen Xuan, H.; Pham, D. T.; Martin, I.; Carrière, P. Enhancement of Polarization Property of Silane-Modified $BaTiO_3$ Nanoparticles and Its Effect in Increasing Dielectric Property of Epoxy/$BaTiO_3$ Nanocomposites. *J. Sci. Adv. Mater. Devices* **2016**, *1* (1), 90–97. https://doi.org/10.1016/j.jsamd.2016.04.005.

(62) Mora-Hernandez, J. M.; Huerta-Flores, A. M.; Torres-Martínez, L. M. Photoelectrocatalytic Characterization of Carbon-Doped NaTaO3 Applied in the Photoreduction of CO_2 towards the Formaldehyde Production. *J. CO_2 Util.* **2018**, *27*, 179–187. https://doi.org/10.1016/j.jcou.2018.07.014.

(63) Yuan, J.; Chen, M.; Shi, J.; Shangguan, W. Preparations and Photocatalytic Hydrogen Evolution of N-Doped TiO_2 from Urea and Titanium Tetrachloride. *Int. J. Hydrog. Energy* **2006**, *31* (10), 1326–1331. https://doi.org/10.1016/j.ijhydene.2005.11.016.

(64) Alammar, T.; Hamm, I.; Wark, M.; Mudring, A.-V. Low-Temperature Route to Metal Titanate Perovskite Nanoparticles for Photocatalytic Applications. *Appl. Catal. B Environ.* **2015**, *178*, 20–28. https://doi.org/10.1016/j.apcatb.2014.11.010.

(65) Lee, W. W.; Chung, W.-H.; Huang, W.-S.; Lin, W.-C.; Lin, W.-Y.; Jiang, Y.-R.; Chen, C.-C. Photocatalytic Activity and Mechanism of Nano-Cubic Barium Titanate Prepared by a Hydrothermal Method. *J. Taiwan Inst. Chem. Eng.* **2013**, *44* (4), 660–669. https://doi.org/10.1016/j.jtice.2013.01.005.

(66) Lu, S.; Zhu, K.; Guo, H.; Wang, H.; Zhang, N.; Alsaedi, A.; Hayat, T.; Li, Y.; Sun, Y. The Influence of Humic Acid on U(VI) Sequestration by Calcium Titanate. *Chem. Eng. J.* **2019**, *368*, 598–605. https://doi.org/10.1016/j.cej.2019.02.210.

(67) Yahya, N. Y.; Ngadi, N.; Jusoh, M.; Halim, N. A. A. Characterization and Parametric Study of Mesoporous Calcium Titanate Catalyst for Transesterification of Waste Cooking Oil into Biodiesel. *Energy Convers. Manag.* **2016**, *129*, 275–283. https://doi.org/10.1016/j.enconman.2016.10.037.

(68) Yang, W.; Tan, G.; Huang, J.; Ren, H.; Xia, A.; Zhao, C. Enhanced Magnetic Property and Photocatalytic Activity of UV-Light Responsive N-Doped $Fe_2O_3/FeVO_4$ Heterojunction. *Ceram. Int.* **2015**, *41* (1), 1495–1503. https://doi.org/10.1016/j.ceramint.2014.09.084.

(69) Li, X.; Zhuang, Z.; Li, W.; Pan, H. Photocatalytic Reduction of CO_2 over Noble Metal-Loaded and Nitrogen-Doped Mesoporous TiO_2. *Appl. Catal. Gen.* **2012**, *429–430*, 31–38. https://doi.org/10.1016/j.apcata.2012.04.001.

(70) Selvaraj, M.; Venkatesan, R.; Mayandi, J.; Venkatachalapathy, V. Influence of Tin (IV) Doping on Structural and Optical Properties of Rhombohedral Barium Titanate ($BaTiO_3$). *Mater. Today Proc.* **2021**, *35*, 13–16. https://doi.org/10.1016/j.matpr.2019.05.302.

(71) Zhang, J.; Xia, A.; Chen, H.; Nizami, A.-S.; Huang, Y.; Zhu, X.; Zhu, X.; Liao, Q. Biobased Carbon Dots Production via Hydrothermal Conversion of Microalgae Chlorella Pyrenoidosa. *Sci. Total Environ.* **2022**, *839*, 156144. https://doi.org/10.1016/j.scitotenv.2022.156144.

(72) Jelovica Badovinac, I.; Peter, R.; Omerzu, A.; Salamon, K.; Šarić, I.; Samaržija, A.; Perčić, M.; Kavre Piltaver, I.; Ambrožić, G.; Petravić, M. Grain Size Effect on Photocatalytic Activity of TiO_2 Thin Films Grown by Atomic Layer Deposition. *Thin Solid Films* **2020**, *709*, 138215.

https://doi.org/10.1016/j.tsf.2020.138215.

(73) Polidoro, D.; Perosa, A.; Rodríguez-Castellón, E.; Canton, P.; Castoldi, L.; Rodríguez-Padrón, D.; Selva, M. Metal-Free *N* -Doped Carbons for Solvent-Less CO_2 Fixation Reactions: A Shrimp Shell Valorization Opportunity. *ACS Sustain. Chem. Eng.* **2022**, *10* (41), 13835–13848. https://doi.org/10.1021/acssuschemeng.2c04443.

(74) Dolat, D.; Quici, N.; Kusiak-Nejman, E.; Morawski, A. W.; Li Puma, G. One-Step, Hydrothermal Synthesis of Nitrogen, Carbon Co-Doped Titanium Dioxide (N,C TiO_2) Photocatalysts. Effect of Alcohol Degree and Chain Length as Carbon Dopant Precursors on Photocatalytic Activity and Catalyst Deactivation. *Appl. Catal. B Environ.* **2012**, *115–116*, 81–89. https://doi.org/10.1016/j.apcatb.2011.12.007.

(75) Kudo, A.; Omori, K.; Kato, H. A Novel Aqueous Process for Preparation of Crystal Form-Controlled and Highly Crystalline $BiVO_4$ Powder from Layered Vanadates at Room Temperature and Its Photocatalytic and Photophysical Properties. *J. Am. Chem. Soc.* **1999**, *121* (49), 11459–11467. https://doi.org/10.1021/ja992541y.

(76) Teng, Z.; Jiang, J.; Chen, G.; Ma, C.; Zhang, F. The Electronic Structures and Optical Properties of B, C or N Doped $BaTiO_3$. *AIP Adv.* **2018**, *8* (9), 095216. https://doi.org/10.1063/1.5047094.

(77) Ibrahim, A. G.; Fouda, A.; Elgammal, W. E.; Eid, A. M.; Elsenety, M. M.; Mohamed, A. E.; Hassan, S. M. New Thiadiazole Modified Chitosan Derivative to Control the Growth of Human Pathogenic Microbes and Cancer Cell Lines. *Sci. Rep.* **2022**, *12* (1), 21423. https://doi.org/10.1038/s41598-022-25772-4.

(78) Yan, Y.; Yang, H.; Yi, Z.; Li, R.; Wang, X. Enhanced Photocatalytic Performance and Mechanism of Au@CaTiO3 Composites with Au Nanoparticles Assembled on CaTiO3 Nanocuboids. *Micromachines* **2019**, *10* (4), 254. https://doi.org/10.3390/mi10040254.

(79) Kędzierska-Matysek, M.; Matwijczuk, A.; Florek, M.; Barłowska, J.; Wolanciuk, A.; Matwijczuk, A.; Chruściel, E.; Walkowiak, R.; Karcz, D.; Gładyszewska, B. Application of FTIR Spectroscopy for Analysis of the Quality of Honey. *BIO Web Conf.* **2018**, *10*, 02008. https://doi.org/10.1051/bioconf/20181002008.

(80) Drabczyk, A.; Kudłacik-Kramarczyk, S.; Głąb, M.; Kędzierska, M.; Jaromin, A.; Mierzwiński, D.; Tyliszczak, B. Physicochemical Investigations of Chitosan-Based Hydrogels Containing Aloe Vera Designed for Biomedical Use. *Materials* **2020**, *13* (14), 3073. https://doi.org/10.3390/ma13143073.

(81) Kavitha, K.; Sutha, S.; Prabhu, M.; Rajendran, V.; Jayakumar, T. In Situ Synthesized Novel

Biocompatible Titania–Chitosan Nanocomposites with High Surface Area and Antibacterial Activity. *Carbohydr. Polym.* **2013**, *93* (2), 731–739. https://doi.org/10.1016/j.carbpol.2012.12.031.

(82) Hamza, M. F.; Wei, Y.; Althumayri, K.; Fouda, A.; Hamad, N. A. Synthesis and Characterization of Functionalized Chitosan Nanoparticles with Pyrimidine Derivative for Enhancing Ion Sorption and Application for Removal of Contaminants. *Materials* **2022**, *15* (13), 4676. https://doi.org/10.3390/ma15134676.

(83) Liu, L.; Li, Y. Understanding the Reaction Mechanism of Photocatalytic Reduction of CO_2 with H_2O on TiO_2-Based Photocatalysts: A Review. *Aerosol Air Qual. Res.* **2014**, *14* (2), 453–469. https://doi.org/10.4209/aaqr.2013.06.0186.

(84) Olivo, A.; Ghedini, E.; Signoretto, M.; Compagnoni, M.; Rossetti, I. Liquid vs. Gas Phase CO_2 Photoreduction Process: Which Is the Effect of the Reaction Medium? *Energies* **2017**, *10* (9), 1394. https://doi.org/10.3390/en10091394.

(85) Bantawal, H.; Krishna Bhat, D. Hierarchical Porous $BaTiO_3$ Nano-Hexagons as A Visible Light Photocatalyst. *Int. J. Eng. Technol.* **2018**, *7* (4.5), 105. https://doi.org/10.14419/ijet.v7i4.5.20022.

(86) Zhang, S.; Song, L. Preparation of Visible-Light-Active Carbon and Nitrogen Codoped Titanium Dioxide Photocatalysts with the Assistance of Aniline. *Catal. Commun.* **2009**, *10* (13), 1725–1729. https://doi.org/10.1016/j.catcom.2009.05.017.

(87) Walczak, R.; Savateev, A.; Heske, J.; Tarakina, N. V.; Sahoo, S.; Epping, J. D.; Kühne, T. D.; Kurpil, B.; Antonietti, M.; Oschatz, M. Controlling the Strength of Interaction between Carbon Dioxide and Nitrogen-Rich Carbon Materials by Molecular Design. *Sustain. Energy Fuels* **2019**, *3* (10), 2819–2827. https://doi.org/10.1039/C9SE00486F.

(88) Zhang, Q.; Lin, C.-F.; Jing, Y. H.; Chang, C.-T. Photocatalytic Reduction of Carbon Dioxide to Methanol and Formic Acid by Graphene-TiO_2. *J. Air Waste Manag. Assoc.* **2014**, *64* (5), 578–585. https://doi.org/10.1080/10962247.2013.875958.

(89) Ai, L.; Yang, Y.; Wang, B.; Chang, J.; Tang, Z.; Yang, B.; Lu, S. Insights into Photoluminescence Mechanisms of Carbon Dots: Advances and Perspectives. *Sci. Bull.* **2021**, *66* (8), 839–856. https://doi.org/10.1016/j.scib.2020.12.015.

(90) Xu, C.; Rangaiah, G. P.; Zhao, X. S. Photocatalytic Degradation of Methylene Blue by Titanium Dioxide: Experimental and Modeling Study. *Ind. Eng. Chem. Res.* **2014**, *53* (38), 14641–14649. https://doi.org/10.1021/ie502367x.

(91) Mkhari, O.; Ntuli, T. D.; Coville, N. J.; Nxumalo, E. N.; Maubane-Nkadimeng, M. S. Supported Carbon-Dots: A Review. *J. Lumin.* **2023**, *255*, 119552. https://doi.org/10.1016/j.jlumin.2022.119552.